Wind Tunnel Study of Preview H_2 and H_∞ Control for Gust Load Alleviation of Flexible Aircraft

Kuang-Ying Ting

A thesis
submitted in partial fulfillment of the
requirements for the degree of

Master of Science in Aeronautics and Astronautics

University of Washington

2021

Reading Committee:

Mehran Mesbahi, Chair

Eli Linve, Chair

Program Authorized to Offer Degree:
William E. Boeing Department of Aeronautics and Astronautics

University of Washington

Abstract

Wind Tunnel Study of Preview H_2 and H_∞ Control for Gust Load Alleviation of Flexible Aircraft

Kuang-Ying Ting

Co-Chairs of the Supervisory Committee:
Professor Mehran Mesbahi

Professor Eli Linve
William E. Boeing Department of Aeronautics and Astronautics

This paper describes simulation and wind tunnel test results of preview gust load alleviation (GLA) controllers based on H_2 and H_∞ approaches. Aeroservoelastic model and gust generation system capabilities at the University of Washington's 3ft by 3ft low-speed wind tunnel allow low-cost testing and, hence, the completion of multiple GLA wind tunnel tests effectively and practically. The test article used for the work reported here is a flexible half wing-body-tail model with active control surfaces, including two ailerons and an elevator. The work reported here demonstrates the feasibility of preview-information-based-control, allowing the control system to respond to advance warning about incoming gusts that would be, in-flight, provided by light detection and ranging (LIDAR) devices. In the wind tunnel, such advance warning is provided by measurements of the motion of gust generation vanes that send gusts into the test section. Discrete output feedback is augmented with various preview lengths of information. The experimental results show that gust load is reduced, compared to feedback only, as a function of preview length and is halved with enough long enough preview information compared to open-loop control or closed-loop control without preview. Test results presented here validate simulation results and add insight.

TABLE OF CONTENTS

LIST OF FIGURES

LIST OF TABLES

ACKNOWLEDGMENTS

I would like to first thank my advisors Professor Mehran Mesbahi and Professor Eli Livne. Thank you Mehran for the guidance you've given me and patience you've shown towards me over the span of my master study. Thank you Eli for the guidance and for the enthusiasm that you've given me for the topics I now study. I also owe thanks to all the members of the RAIN Lab who have assisted me over the years.

I would also like to thank Larry Cheng, George Huang and Mengyuan Wang for their feedback. Many thanks to John Berg, Bijan Barzgaran, Jake Quenzer from the University of Washington's aeroservoelasticity research group and Alison Zongolowicz, Kimber Hinson, Kioumars Najmabadi, Brian Rupnik, Gregory Clark, Alexander Ho, and Prachya Panyakeow from the Boeing for supporting GLA research at the University of Washington and many insightful discussions and suggestions.

Chapter 1
INTRODUCTION

The research collaboration is interested in high-performance fly-by-wire flight control technology, including gust load alleviation (GLA) and maneuver load alleviation (MLA). The flight control law for aircraft longitudinal and lateral dynamics involves designing, optimizing, and implementing control laws and analysis. The work reported here focuses on the preview-information-based GLA system design and implementation. This chapter starts with the motivation, then introduces the prior works the research group has done, and finally presents the problem formulation and contribution.

1.1 Motivation

The pursuit of methods and means for reducing gust response and gust loads in flight dates back to the early days of aviation, before WWII, with more and more activity including flight tests [5], in the late 1940s and 1950s. Developments in control theory and hardware led to many studies of active GLA, with the concept as well as many control law types demonstrated in flight in the 1960s, [6–9], already in a field that has remained active until today [10, 11]. Numerous theoretical studies of GLA techniques have been published. Many wind tunnel tests have been completed and reported. GLA technology has become an important part of the development of Multidisciplinary Design Optimization (MDO) of flight vehicles, where the flight vehicle optimization process seeks to find the optimal structural, aerodynamic, and control design, subject, among many other families of constraints, to constraints on the dynamic loads and ride comfort of crew and passengers due to atmospheric gusts [12].

Naturally, GLA technology has followed the development of control technology over the

years, beginning with classical single-input single-output (SISO) control laws, then proceeding to multi-input multi-output (MIMO) designs via Linear Quadratic Regulatr (LQR) and Linear Quadratic Gaussian (LQG) control laws [13]. Various forms of robust control approaches have been tested. GLA systems can be found now on almost every advanced actively-controlled flight vehicle.

Among the many modern control law alternatives that have been studies over the years in GLA applications, the H_2 and H_∞ [14] controllers are still of major interest because of their central place in modern control theory. More recently, Model Predictive Control [15, 16] was evaluated. Relatively recent GLA control law synthesis and wind tunnel tests, using a large wind tunnel model and alternative control laws in an international collaboration, is presented in [17].

From the early years of GLA work it, was intuitively clear, in concept, that the capability of an active control system to reduce the response to sudden gusts significantly is limited if the system begins to respond to the gust only once the airplane is hit by it. If information about incoming sudden gusts could just be known at an acceptable level of certainty ahead of time, the thinking has been, the potential suppression of the response could be, maybe, much improved. This triggered the examination of technologies that would provide early detection of incoming gusts in flight. LIDAR sensors measure the distance by using the reflection of an emitting laser. This technology has terrestrial, airborne, and mobile applications for 2-D and 3-D scanning and representation. In particular, turbulence gust ahead of the airplane can be measured by the LIDAR, as described in [18–20]. This makes it possible for an aircraft with onboard LIDAR sensors to preview the gust disturbance ahead of encounter. The preview GLA formulation, simulation [15, 21–26], wind tunnel experiments [2, 3, 27], and flight test [28, 29] have all been explored. Table 1.1 summarizes prior GLA works with corresponding control laws and test methods. The need for experimental validation and experience building with preview H_∞ controllers is evident.

With all advances made to date in computational modeling and simulation of aeroelastic and aeroservoelastic systems, the uncertainty of such systems can still be considerable, mak-

ing experimental studies of GLA extremely valuable. Flight tests of new GLA technologies are costly for full-scale aircraft. Flight tests with small Unmanned Aerial Vehicle (UAV) are more affordable but are challenged by scaling the hardware and operation. In both cases the environments and parameters may not be well controllable, and the desired gusts are not repeatable for GLA systems tests. Wind tunnel experiments, however, provide controlled and repeatable environments for testing [30–32] and they are cost-effective compared to flight tests. Miniature control systems hardware developments of recent years make the development of low-cost aeroelastic wind tunnel testing capabilities and rapid aeroservoelastic practical.

The University of Washington's William E. Boeing Department of Aeronautics and Astronautics has two low-speed wind tunnels: a modern 3ft by 3ft low-speed wind tunnel and a 12ft by 8ft commercial low-speed wind tunnel (the Kirsten Wind Tunnel). Active flexible models for GLA tests were developed for both systems, In this work, we focus on the 3ft by 3ft wind tunnel, for which a vane-driven gust generation system and a wing/fuselage/tail aeroservoelastic wind tunnel model were developed. The systems [4] and early control law synthesis, implantation, and test results are presented in [2, 3]. The present paper aims at building experience and adding insight regarding the synthesis and test performance of H_2 and H_∞ controllers, including the effects of gust preview information. This also includes the evaluation of analysis and test correlation.

Table 1.1: Some preview gust load alleviation works using MPC, H_∞, and H_2 controllers

	Simulation	Wind Tunnel Test	Flight Test
Feedforward	Fezans and Joos [21]		Rabadan et al. [28]
Model Predictive Control	Giesseler et al. [15]	Barzgaran et al. [2, 3]	
H_2	Hamada [22]	Hamada et al. [27]	Hamada [29]
H_∞	Khalil and Fezans [23–25] Takase et al. [26]		

1.2 Prior Work

The prior works have been done by previous graduate students, Jake Quenzer and Alison Zongolowicz, and graduate students, Bijan Barzgaran and Kimber Alison. The initial development in [1] is a Nastran model that resembles commercial aircraft for aero-structural aircraft flight control investigation. The mathematical work of generic wide body aircraft model led to interests in experimental validation and development of the aeroservoelastic wind tunnel model [4], the testbed built in 3ft by 3ft wind tunnel for studying the control laws. Lastly, [2, 3] presents the wind tunnel test results of GLA with MPC method.

1.2.1 The Generic Wide Body Aircraft Model

The aero-structural aircraft model is developed for studying the modern flight control of large commercial aircraft. The generic wide body (GWB) model, as shown in Figure 1.1, supports the study of flight control systems on airframes with both rigid body flight-dynamic mode and structural vibration mode. The GWB is a full-vehicle aero-structural model defined via NASTRAN modeling elements and is comparable in size, shape, and structure to Airbus A350-1000 and Boeing 777-300ER. The model used only information from the public domain.

1.2.2 Model for Aeroelastic Response to Gust Excitation

The model for aeroelastic response to gust excitation (MARGE) is the wind tunnel testbed built over the spring and early summer of 2018 to demonstrate and compare active control laws of a flexible aircraft to gust excitation. The testbed has a modular design allowing modification for desired structure dynamics and control surfaces. The nominal configuration is a half-span aircraft model with three control surfaces of two ailerons on the outer shells and elevator, as shown in Figure 1.2. The MARGE has one rigid body mode and two structural modes, but the second structural mode is out of the actuator bandwidth. The wind tunnel testing verified the dynamic characteristic and validated the model for GLA control law research. A detailed description of the testbed is given in Chapter 3.

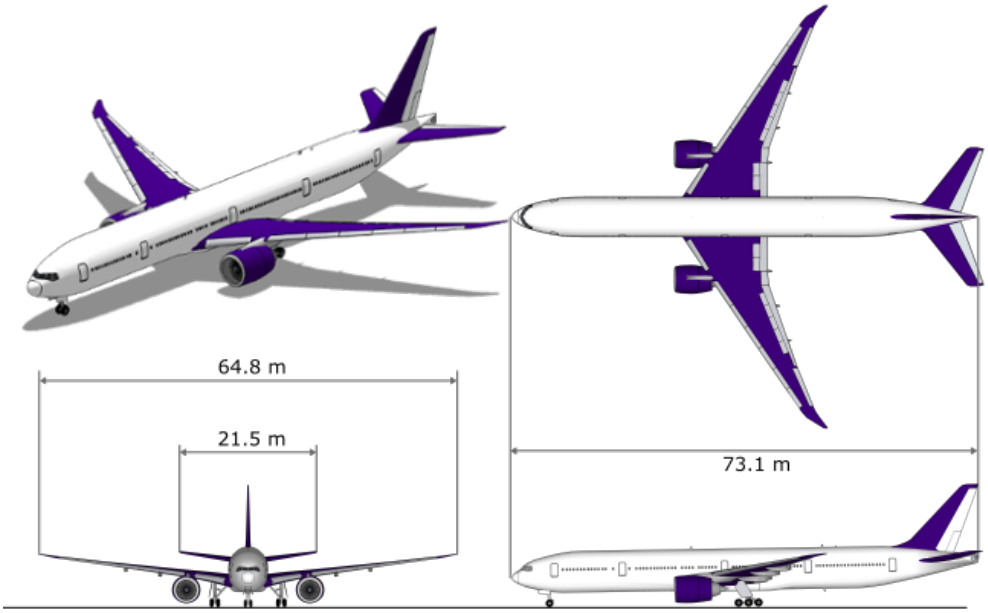

Figure 1.1: The generic wide body aircraft model dimension [1]

1.2.3 Low-Cost Wind Tunnel Studies of Gust Alleviation Control Techniques

The work is followed by the development of MARGE, which is capable of wind tunnel testing for gust load alleviation research. The testbed includes two systems: the flexible half-span wind tunnel model and gust generation system (GGS). This article further detailed the GGS and presented the initial results of GLA with the MPC approach. Figure 1.3 shows the time history of the closed-loop system response.

Figure 1.2: The aeroservoelastic model in the wind tunnel [2]

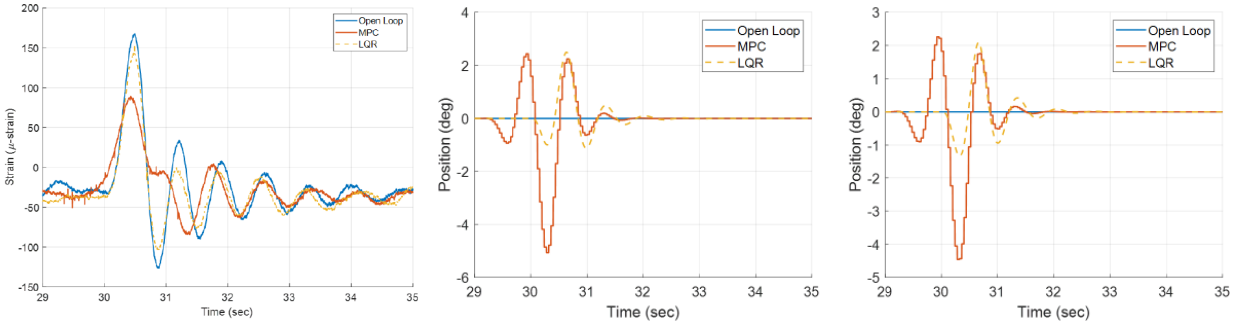

(a) Wing-root strain

(b) Outboard (left) and inboard (right) ailerons

Figure 1.3: Time history of MPC closed-loop response with a $1 - \cos$ gust disturbance [2]

1.2.4 Real-Time Model Predictive Control for Gust Load Alleviation on an Aeroelastic Wind Tunnel Test Article

The paper details the design and implementation of real-time MPC for GLA on MARGE. The MPC architecture has full control of two ailerons to achieve wing-root load reduction. The article presented both constrained and unconstrained MPC results with an additional study on the parameterization of prediction window lengths and prediction horizons. The test results are summarized in Figure 1.4.

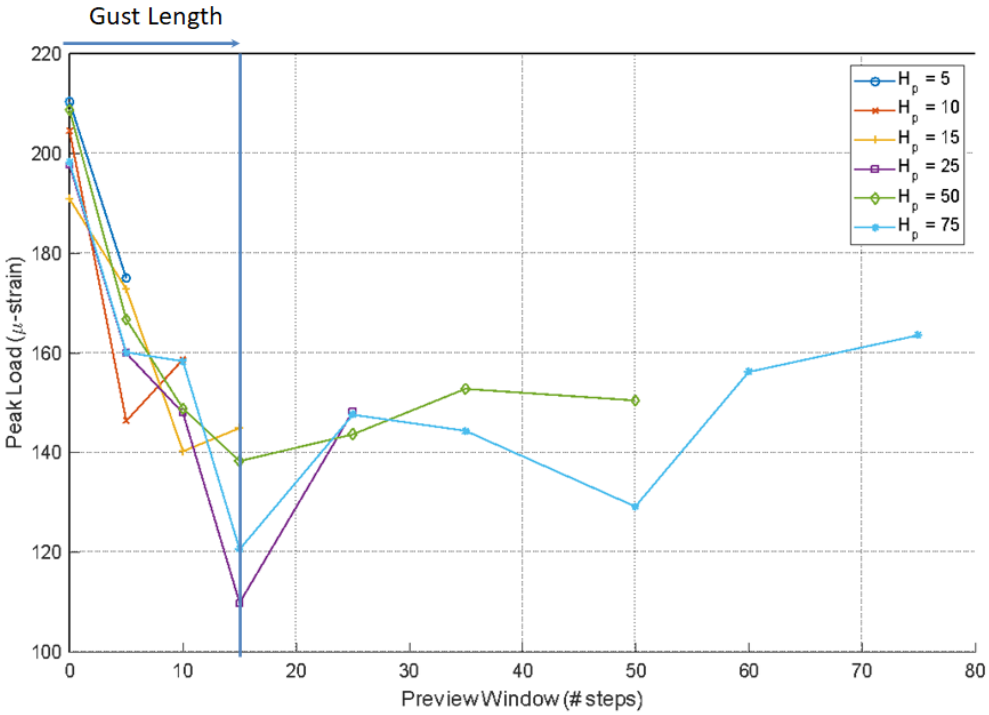

Figure 1.4: Summary of control performance in load alleviation for prediction of horizon, given in the legend, and preview window variation, on the x-axis [3]

1.3 Problem Formulation

The H_∞ control technique accounts worst-case scenario and suppresses peak gain. The GLA is a disturbance rejection problem that is nature to be formulated in the H_∞ control framework suppressing peak response against exogenous inputs. Feedforward and preview controls are not a new topic in theory and application [33]; however, the development of Doppler LIDAR enabling gust and disturbance detection ahead of encounter renews the interests in GLA with preview-information-based-control. In SciTech 2019, [23] proposed the discrete-time preview H_∞ output feedback control formulation by enhancing the robust control performance using preview information. The proposed method claimed the reduced the gust load surpass the feedback-only control and is proportional to the given preview information. The interests in the application include implementation of the controller, gust load reduction, and benefits of the controllers comparing to the existing methods.

1.4 Contribution

This thesis demonstrates the feasibility of preview information benefiting the controller performance. The present control laws of H_2 and H_∞ incorporate finite preview information to reduce the H_2 and H_∞ norm of the closed-loop transfer function and minimize the wing-root strain. The finite preview information is modeled as discrete dynamic systems and augmented in the plant such that the preview problem could be solved as the standard form of the H_2 and H_∞ optimal control problem. Both H_2 and H_∞ controller norms and maximum wing-root strain reduce with respect to the given preview lengths. This work adds insights to experimental wind tunnel results of both preview H_2 and H_∞ control and verifies the simulation works. Furthermore, detailed discussion on the systematic controller synthesis and H_2 and H control interpretation are provided.

1.5 Thesis Organization

In Chapter 2, background and preliminary mathematical knowledge are introduced, including optimal control theory in LQR, estimation theory in Kalman Filter, and Robust Control of $\mathcal{H}_\infty$. In Chapter 3, the experimental apparatus and setup are specified. In Chapter 4, a systematic approach of controller design is detailed, and preview augmentation is formulated. In Chapter 5 the simulation and experimental results are presented, and a discussion is given in Chapter 6. Finally, Chapter 7 contains concluding remarks and future works encouraged by this effort.

Chapter 2
BACKGROUND AND MATHEMATICAL PRELIMINARIES

This chapter introduces some terminology and conceptual material of optimal control theory, estimation theory, and robust control theory.

2.1 Optimal Control

Optimal control theory is formulated as mathematical optimization computing control input for dynamical systems achieving optimized objective function. A control problem includes a cost function that is a function of state and control variables to achieve an optimized and desired trajectory. A general cost function is

$$J(x,u) = l(k,x_k) + \sum_{\tau=0}^{N-1} \mathcal{L}(k,x_\tau,u_\tau) \tag{2.1}$$

The desired trajectory and the optimized control are determined based on the cost function where Nonlinear Programming (NLP) is studied. Given Equation 2.1, the cost of each time step could be determined given states and inputs; however, the optimal trajectory and control inputs need to be solved through a multi-stage optimization problem using Bellmans' Principle of Optimally, which considers as the Optimal Control Problem (OCP). A general nonlinear optimal control problem is

$$\begin{aligned} &\min_u J(x,u) \\ \text{s.t} \quad &x_{k+1} = f(k,x_k,u_k) \end{aligned} \tag{2.2}$$

The general nonlinear OCP minimizes the cost function, shown in Equation 2.1, of the sum of all running costs from the initial condition to the final condition subject to a nonlinear dynamic system. Bellmans' Principle reduces OCP to a sequence of NLP such that the

optimal cost at each step time could be calculated.

$$J_k^*(x_k) = \min_{u_k \in \mathcal{R}^m} \{L(k, x_k, u_k) + J_{k+1}^*(x_{k+1})\} \tag{2.3}$$

The LQR is a special case of the general nonlinear OCP. The LQR minimizes a quadratic cost function subject to a linear dynamic system. The cost function is generalized from Equation 2.1 to

$$J(x, u) = \frac{1}{2} x_N^\intercal Q x_N + \frac{1}{2} \sum_{\tau=0}^{N-1} (x_\tau^\intercal Q x_\tau + u_\tau^\intercal R u_\tau) \tag{2.4}$$

The LQR optimal control problem is derived from Equation 2.2 to

$$\begin{aligned} &\min_u J(x, u) \\ &\text{s.t} \quad x_{k+1} = Ax_k + Bu_k \end{aligned} \tag{2.5}$$

As the result of solving OCP, the optimal cost and control input could be solved recursively backward in time. The sequential NLP could be further reduced to the Riccati differential equation. The solution of Discrete Algebraic Riccati Equation (DARE) is

$$P_k = (A_k - B_k K_k)^\intercal P_{k+1} (A_k - B_k K_k) + K_k^\intercal R_k K_k + Q_k \tag{2.6}$$

The computed optimal gain is

$$K_k = (B_k^\top P_{k+1} B_k + R_k)^{-1} B_k^\intercal P_{k+1} A_k \tag{2.7}$$

where the optimal state-feedback control input is

$$u_k^* = -K_k x_k \tag{2.8}$$

and optimal cost at each time step becomes

$$J_k^* = \frac{1}{2} x_k^\intercal P_k x_k \tag{2.9}$$

2.2 Estimation Theory

Estimation theory estimates the parameters using the observed measurements. The parameters represent physical system variables affecting the distribution of observed measurements, and the estimator approximates the unknown parameters based on measured data. The general estimation theory involves a probabilistic assumption that the measurement data is random with a probabilistic distribution. This section briefly introduces the Kalman Filter, integrated into the real-time Simulink environment, used for state estimation in the experiment. The detailed mathematics and derivations are in Chapter 8 of [34].

Kalman filter is a branch of estimation theory known as Linear Quadratic Estimation (LQE) because of minimizing mean squared error (MSE), quadratic cost, between the measurements and estimates subjecting to a linear dynamic system. It is a dual problem of LQR. The minimization problem is formulated as

$$\begin{aligned} &\min \frac{1}{2}(y - C\hat{x})^\intercal R^{-1}(y - C\hat{x}) \\ \text{s.t} \quad &x_{k+1} = Ax_k + Bu_k + w_k, \quad w_k \sim N(0, Q) \\ &y_k = Cx_k + v_k, \quad v_k \sim N(0, R) \end{aligned} \tag{2.10}$$

The Kalman filter estimates states through joint probability distribution at each time step using measurements with noise and inaccuracies. The algorithm is a two-step process. In the prediction step, the Kalman filter predicts the current states with previous states estimate $\hat{x}_{k-1}^+$ and predicts the error covariance P_k^- is with previous error covariance P_{k-1}^+ and measurement noise covariance.

$$\hat{x}_k^- = A\hat{x}_{k-1}^+ + Bu_{k-1} \tag{2.11}$$

$$P_k^- = AP_{k-1}^+A^T + BQB^T \tag{2.12}$$

The Kalman gain is derived through an optimal probabilistic method which is the minimum variance approach.

$$K_k = P_k^- C^T \left(CP_k^- C^T + R\right)^{-1} \tag{2.13}$$

Kalman filter updates the estimation with Kalman gain multiplying the difference between measurements and estimated observations in the update step. The error covariances are updated respectively.

$$\hat{x}_k^+ = \hat{x}_k^- + K_k \left(y_k - C\hat{x}_k^- \right) \tag{2.14}$$

$$P_k^+ = \left(I - K_k C \right) P_k^- \tag{2.15}$$

Once the states are estimated, the subsequent measurements are fed into the filter, and the Kalman filter repeats the steps above with prediction of priori states and covariance and correction of posteriori states and covariances. As a result, the Kalman filter's predictor-corrector form is recursive and can be implemented in real-time, using only the present input measurements and the last time step states and covariances without any past information.

2.3 Robust Control

Robust control generally refers to control methods that ensure robust stability and performance. In this article, the robust control refers to the H_∞ optimization, which is with bounded uncertainty and disturbance and embedded with margins in phase and gain to quantify the robustness of the closed-loop system. The theory of robust control started in the late 1970s and early 1980 to overcome lack of robustness in LQG design [35], which is combined LQR and LQE. A brief history of robust control is given by Safonov in [36] and the H_∞ terminology is first introduced by Zames in [37]. The symbol H stands for *Hardy Space*. The H_2 and H_∞ control problem shares a similar framework and solution such that they are discussed together. The details of controller synthesis are discussed in [38–40] and Chapter 9 of [41], and are not presented here.

2.3.1 H_2 and H_∞ norm

Assuming continuous linear time-invariant (LTI) system as below

$$\begin{aligned} \dot{x}(t) &= Ax(t) + Bu(t) \\ y(t) &= Cx(t) + Du(t) \end{aligned} \tag{2.16}$$

where the transfer matrix in terms of state-space data is denoted

$$G(s) = \left[\begin{array}{c|c} A & B \\ \hline C & D \end{array}\right] := C(SI - A)^{-1}B + D. \tag{2.17}$$

The transfer matrix in Equation 2.17 can be further partitioned in the form of

$$G(s) = \left[\begin{array}{c|cc} A & B_1 & B_2 \\ \hline C_1 & D_{11} & D_{12} \\ C_2 & D_{21} & D_{22} \end{array}\right] \tag{2.18}$$

and the state-space representation is

$$\begin{aligned} \dot{x}(t) &= Ax(t) + B_1 d(t) + B_2 u(t) \\ z(t) &= C_1 x(t) + D_{11} d(t) + D_{12} u(t) \\ y(t) &= C_2 x(t) + D_{21} d(t) + D_{22} u(t) \end{aligned} \tag{2.19}$$

where $x(t) \in \mathbb{R}^n$, $d(t) \in \mathbb{R}^l$, and $u(t) \in \mathbb{R}^m$ are the state vector, exogenous/disturbance input vector, and the control input vector. The $z(t) \in \mathbb{R}^p$ and $y(t) \in \mathbb{R}^q$ denote the regulated outputs and observed outputs, respectively. The regulated outputs are not necessarily fed back to the closed-loop system, but the observed outputs are used for feedback control.

The most commonly used performance measures are the norms, $||\cdot||$, with the 2-norm and the ∞-norm shown below.

$$\left\|G(s)\right\|_2 \triangleq \left(\tfrac{1}{2\pi}\int_{-\infty}^{\infty}\left|G(j\omega)\right|^2 d\omega\right)^{1/2} \tag{2.20}$$

$$\left\|G(s)\right\|_\infty \triangleq \sup_\omega \sigma_{\max}\left|G(j\omega)\right| \tag{2.21}$$

where ω is the frequency.

The H_∞ norm of a stable scalar transfer function $G(s)$ is the peak value, and the H_∞ norm of a stable transfer matrix $G(s)$ is the largest singular value of $G(j\omega)$ as a function of frequency. The H_∞ is the set of stable and proper transfer functions with bounded ∞-norm. Similarly, the H_2 is the set of stable and strictly proper transfer functions with bounded 2-norm.

H_2 norm

The H_2 norm in Equation 2.20 could be reformulated using the Frobenius norm as

$$\left\|G(s)\right\|_2 \triangleq \left(\frac{1}{2\pi}\int_{-\infty}^{\infty} \mathrm{tr}\left(G(j\omega)^H G(j\omega)\right) d\omega\right)^{1/2} \tag{2.22}$$

where G must be strictly proper to avoid infinite H_2 norm. Furthermore, by Parseval's Theorem, Equation 2.22 is equal to the H_2 norm of the impulse response

$$\left\|G(s)\right\|_2 = \left\|g(t)\right\|_2 \triangleq \left(\int_0^{\infty} \mathrm{tr}\left(g(\tau)^H g(\tau)\right) d\tau\right)^{1/2} \tag{2.23}$$

As a result, the deterministic performance interpretation of the H_2 norm is derived as below.

$$\left\|G(s)\right\|_2 = \max_{w(t)=\text{unit impulse}} \left\|z(t)\right\|_2 \tag{2.24}$$

H_∞ norm

The H_∞ norm in Equation 2.21 is the peak magnitude of the transfer function. The H_∞ norm is the upper bound of the closed-loop transfer function by proper normalization and weight, and could be used as a performance specification in terms of weighted sensitivity, mixed sensitivity, etc. Moreover, the H_∞ norm has several time-domain performance interpretations. First, it is the worst-case steady-state gain for sinusoidal inputs at any frequency. Second, the H_∞ norm is equal to the induced 2-norm in the time domain as

$$\left\|G(s)\right\|_\infty = \sup_{d(t)\neq 0} \frac{\left\|z(t)\right\|_2}{\left\|d(t)\right\|_2} = \sup_{||d(t)||_2=1} \left\|z(t)\right\|_2 \tag{2.25}$$

Equation 2.25 suggest the maximum gain results from the worst input signal $d(t)$ of a sinusoidal with frequency ω^* aligning the direction of $\bar{\sigma}(G(j\omega^*))$. Lastly, the H_∞ norm is equal to the induced power norm and has an interpretation of an induced norm in terms of expected values of stochastic signals.

The difference of the H_2 and H_∞ norm could be seen in Equations 2.21 and 2.26 in term of singular values.

$$\left\|G(s)\right\|_2 = \left(\frac{1}{2\pi}\int_{-\infty}^{\infty} \sum_i \sigma_i^2(G(j\omega)) d\omega\right)^{1/2} \tag{2.26}$$

Minimizing the H_∞ norm is minimizing the largest singular value at the worst direction and the worst frequency while minimizing the H_2 norm is minimizing the sum of the square of all the singular values over all frequencies. In the time-domain interpretations, minimizing H_∞ norm alleviates the worst response of the system and minimizing H_2 norm reduces the overall energy of the system.

Moreover, the H_∞ satisfies the multiplicative property, which given any $A(s)$ and $B(s)$ that

$$\left\| A(s)B(s) \right\|_\infty \leq \left\| A(s) \right\|_\infty \cdot \left\| B(s) \right\|_\infty \tag{2.27}$$

This property allows the H_∞ norm to satisfy the Small Gain Theorem. First, assume stable loop transfer function, $L(s)$, and the spectral radius, $\rho(L(j\omega))$, is defined as the maximum eigenvalue magnitude at each frequency.

$$\rho(L(j\omega)) \triangleq \sup_i |\lambda_i(L(j\omega))| \tag{2.28}$$

Theorem 1 (Spectral radius stability condition) *Consider a system with a stable loop transfer function $L(s)$. Then the closed-loop system is stable if*

$$\rho(L(j\omega)) < 1 \qquad \forall\omega \tag{2.29}$$

Theorem 1 claims that if the system gain is less than 1 in all directions, all eigenvalues, and for all frequencies, then all signals attenuation will die out, and the system is stable. For any matrix norm that

$$\rho(A) \leq \left\| A \right\| \tag{2.30}$$

suggests the eigenvalue of the matrix is measured only in a certain direction and must be less than a matrix norm which allows any direction and yields maximum gain. By combining Equations 2.29 and 2.30 leads to the small gain theorem.

Theorem 2 (Small Gain Theorem) *Consider a system with a stable loop transfer function $L(s)$. Then the closed-loop system is stable if*

$$\left\| L(s) \right\| < 1 \qquad \forall \omega \tag{2.31}$$

where $||L(s)||$ denotes any matrix norm satisfying $||AB|| \leq ||A|| \cdot ||B||$

Although both Theorems 1 and 2 are conservative and excluded phase information, they guarantee the closed-loop system's stability condition. Therefore, if the induced norm such as ∞-norm of the stable closed-loop system is less than 1, then the signal in closed-loop will be attenuated and die out. On the other hand, even though H_2 has numerous good mathematical and numerical proprieties, the H_2 is not an induced norm and does not satisfy the multiplicative property. This guarantees no stability on the cascaded interconnections of the system.

2.3.2 H_2 and H_∞ control problem

The H_2 and H_∞ norm are introduced in the previous section, Section 2.3.1. The control problem of H_2 and H_∞ is minimizing the overall energy and the largest response of the system, respectively. The general control configuration of the H_2 and H_∞ are often illustrated as in Figure 2.1, where the closed-loop system is the linear fractional transformation of the plant, G, and controller, K. The system in Figure 2.1 is described by

$$\begin{bmatrix} z \\ y \end{bmatrix} = G(s) \begin{bmatrix} d \\ u \end{bmatrix} = \begin{bmatrix} G_{11}(s) & G_{12}(s) \\ G_{21}(s) & G_{22}(s) \end{bmatrix} \begin{bmatrix} d \\ u \end{bmatrix} \tag{2.32}$$

$$u = K(s)y \tag{2.33}$$

with transfer matrix representation in Equation 2.18 and state-space representation in Equation 2.19. The closed-loop transfer function from the exogenous signals, d, to regulated outputs, z, is given by the linear fractional transformation

$$z = F_l(G, K)d \tag{2.34}$$

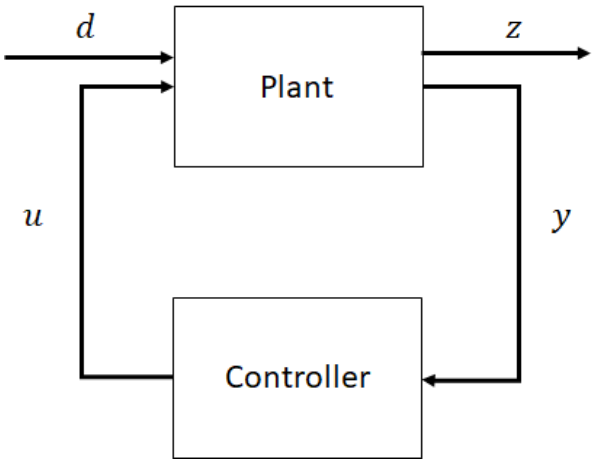

Figure 2.1: General Control Configuration

where $F_l(G, K)$ is often denoted as T_{zw} and used interchangeably in this article as

$$F_l(G, K) = P_{11} + P_{12}K(I - P_{22}K)^{-1}P_{21} \tag{2.35}$$

H_2 and H_∞ control minimize the H_2 and H_∞ norms of $F_l(P, K)$ respectively.

There are different approaches to solve the H_∞ control problem [38–40]. The most used approaches for H_2 and H_∞ control problems are based on the state-space solution in [38]. Doyle et al. solved two Riccati equations, also known as Riccati (RIC) method, for the H_2 and H_∞ problem with the demonsion of controller as the plant state-order. A controller exists if and only if the unique stabilizing solutions to two algebraic Riccati equations (AREs) are positive definite and the spectral radius of their product is less than γ^2, where γ is the controller performance value and $|G|_\infty < \gamma$. Gahinet and Apkarian solved the H_∞ problem with Linear Matrix Inequality (LMI) approach [39], specifically using three Riccati inequalities. The solvability conditions are the Riccati inequalities instead of indefinite Riccati equations and the three LMI could be solved by convex optimization. The *hinfsyn* function in MATLAB Robust Toolbox [42] can use either RIC or LMI method and yield controller order as plant order. Lastly, Apkarian and Noll developed nonsmooth optimization techniques, other than the LMI or RIC, to solve the H_∞ synthesis problem with additional structural

constraints. The additional structural constraints such as static, fixed-order, fixed-structure, decentralized control, design of PID controller, and simultaneous design and stabilization make the H_∞ synthesis problem nonconvex. The method solves quadratic programming for descent direction and generates steps through line search. The nonsmooth H_∞ synthesis is the *hinstruct* function in MATLAB Robust Toolbox [42]. The work in the paper used RIC method for full-order and nonsmooth method for fixed-order controller synthesis. The assumptions on the generalized plant for each method are in Table 2.1.

Table 2.1: Assumption on the generalized plant

Method	RIC	LMI and Nonsmooth
G(s)	$\left[\begin{array}{c\|cc} A & B_1 & B_2 \\ \hline C_1 & 0 & D_{12} \\ C_2 & D_{21} & 0 \end{array}\right]$	$\left[\begin{array}{c\|cc} A & B_1 & B_2 \\ \hline C_1 & D_{11} & D_{12} \\ C_2 & D_{21} & 0 \end{array}\right]$
Assumptions	1. (A, B_1) is stabilizable and (C_1, A) is detectable. 2. (A, B_2) is stabilizable and (C_2, A) is detectable. 3. $D_{12}^\intercal \begin{bmatrix} C_1 & D_{12} \end{bmatrix} = \begin{bmatrix} 0 & I \end{bmatrix}$. 4. $\begin{bmatrix} B_1 \\ D_{21} \end{bmatrix} D_{21}^\intercal = \begin{bmatrix} 0 \\ I \end{bmatrix}$.	1.(A, B_1) is stabilizable and (C_1, A) is detectable. 2.$D_{22} = 0$
Controller order	Full (as state order)	LMI: Full (as state order) Nonsmooth: Full (as state order) or reduced (specified)

The assumptions for the RIC method are more restricted than the other two. Assumptions 1 and 2 are required for the existence of stabilizing controller K and simplify the assumption of internal stability, which is equivalent to input-output stability. These assumptions ensure the optimal controller does not yield any pole-zero cancellation on the imaginary axis resulting in closed-loop instability. Assumptions 3 and 4 suggest orthogonality and assume no correlation as $D_{12}^\intercal C_1 = 0$ and $B_1 D_{21}^\intercal = 0$. The implicit assumptions of $D_{11} = 0$ and $D_{22} = 0$ are required for H_2 to be the set of strictly proper stable transfer function but not for H_∞. $D_{11} = 0$ and $D_{22} = 0$ are assumed for simplification of calculation for H_∞.

2.3.3 H_2 Optimization: Linear Quadratic Gaussian

The system is assumed to be a continuous LTI system which is defined as

$$\dot{x}(t) = Ax(t) + E\mu(t) + B_2u(t) \tag{2.36}$$

$$y(t) = C_2x + F\nu(t) + D_{22}u(t) \tag{2.37}$$

where μ is exogenous or disturbance input vector, and ν is exogenous or observation noise output vector.

The LQG controller and observer are in the form below

$$\dot{\hat{x}}(t) = A\hat{x}(t) + B\hat{u}(t) + L(y(t) - \hat{y}(t)) \tag{2.38}$$

$$\hat{y}(t) = C\hat{x}(t) + Du(t) \tag{2.39}$$

where $\hat{u} = -K\hat{x}$. K is the controller gain of LQR, and L is the observer gain of LQE. In LQG, K is chosen to minimize

$$\int_0^\infty x(t)^\intercal Qx(t) + u(t)^\intercal Ru(t)\ dt \tag{2.40}$$

where $Q \geq 0$ and $R > 0$; similarly, L is chosen to minimize

$$E\{\int_0^\infty \mu(t)^\intercal E^\intercal E\mu(t) + \nu(t)^\intercal F^\intercal F\nu(t)\ dt\} \tag{2.41}$$

where $F^\intercal F > 0$. By relating the regulated output in the H_2 problem with the LQR cost function, it becomes

$$||z(t)||_2^2 = \int_0^\infty x(t)^\intercal Qx(t) + u(t)^\intercal Ru(t)dt \tag{2.42}$$

The regulated outputs and the exogenous inputs are

$$z(t) = \begin{bmatrix} Q^{\frac{1}{2}}x(t) \\ R^{\frac{1}{2}}u(t) \end{bmatrix}, \qquad w(t) = \begin{bmatrix} \mu(t) \\ \nu(t) \end{bmatrix} \tag{2.43}$$

The system is reformulated as following equations

$$\dot{x}(t) = Ax(t) + \begin{bmatrix} B_1 & B_2 \end{bmatrix} \begin{bmatrix} w(t) \\ u(t) \end{bmatrix} \tag{2.44}$$

$$\begin{bmatrix} z(t) \\ y(t) \end{bmatrix} = \begin{bmatrix} C_1 \\ C_2 \end{bmatrix} x(t) + \begin{bmatrix} D_{11} & D_{12} \\ D_{21} & D_{22} \end{bmatrix} \begin{bmatrix} w(t) \\ u(t) \end{bmatrix} \tag{2.45}$$

This led to the following transfer matrix realization for system

$$G(s) = \left[\begin{array}{c|cc} A & \begin{bmatrix} E & 0 \end{bmatrix} & B_2 \\ \hline \begin{bmatrix} Q^{\frac{1}{2}} \\ 0 \end{bmatrix} & D_{11} & \begin{bmatrix} 0 \\ R^{\frac{1}{2}} \end{bmatrix} \\ C_2 & \begin{bmatrix} 0 & F \end{bmatrix} & D_{22} \end{array}\right] \tag{2.46}$$

which satisfies all general assumptions of solving AREs as shown in Table 2.1.

1. $(Q^{\frac{1}{2}}, A)$ is detectable and (A, B_1) is stabilizable.

2. (C_2, A) is detectable and (A, B_2) is stabilizable.

3. $D_{12}^{\intercal} \begin{bmatrix} C_1 & D_{12} \end{bmatrix} = \begin{bmatrix} 0 & R \end{bmatrix}$.

4. $\begin{bmatrix} B_1 \\ D_{21} \end{bmatrix} D_{21}^{\intercal} = \begin{bmatrix} 0 \\ F^{\intercal} F \end{bmatrix}$.

Lastly, if $D_{11} = D_{22} = 0$, then LQG cost depends on state and control input individually (No N term).

2.4 Chapter Summary

This chapter gives background and mathematical preliminaries on optimal control theory in LQR, optimal estimation theory in LQE, and robust control on H_∞ optimization. The LQR method is one of the first method used in aeroservoeslastic wind tunnel control and is also used to verify the H_2 control implementation as shown in Section 2.3.3. The LQE,

Kalman filter, is used for states estimations of the wing bending mode for full-state feedback. The next chapter, Chapter 3, details the setup and integration of hardware and software for real-time GLA.

Chapter 3
EXPERIMENTAL SETUP

This chapter introduces the testbed and test-article for experimental setup and then the software environment, architecture, and hardware in the loop. The development of aeroservoelastic wind tunnel model for studying GLA control laws in the 3ft by 3ft low-speed wind tunnel is detailed in [2–4].

3.1 3ft by 3ft Low-Speed Wind Tunnel

The historic wind tunnel is funded by William E. Boeing for training engineers and testing airplanes in the late 1910s and is donated to the University of Washington to develop an aeronautics curriculum. The modern 3ft by 3ft Low-Speed Wind Tunnel is housed in the historic 1917 Boeing's original wind tunnel building. The 3ft by 3ft low-speed wind tunnel has a 9-to-1 contraction ratio, 3ft by 3ft by 8ft test section, and a wind speed capability of 34-135 mph. The electric fan has a constant rotation speed, and the variable pitch allows control of the desired wind speed. Is is an open circuit tunenl. Figure 3.1 shows the wind tunnel and its part schematically.

3.2 Gust Generation System

The GGS is installed at the extension section between the contraction section and test section, as shown in Figure 3.1. This extension/transition section between the inlet contraction and the test sections was designed for quick installation and removal of the gust system. There are two NACA0012-airfoil movable gust vanes with of 10-inch chord length each. They are installed vertically and spaced evenly 7 inches from the centerline to avoid their wakes hitting the model. The vanes are designed to be very stiff and have minimal distortion under

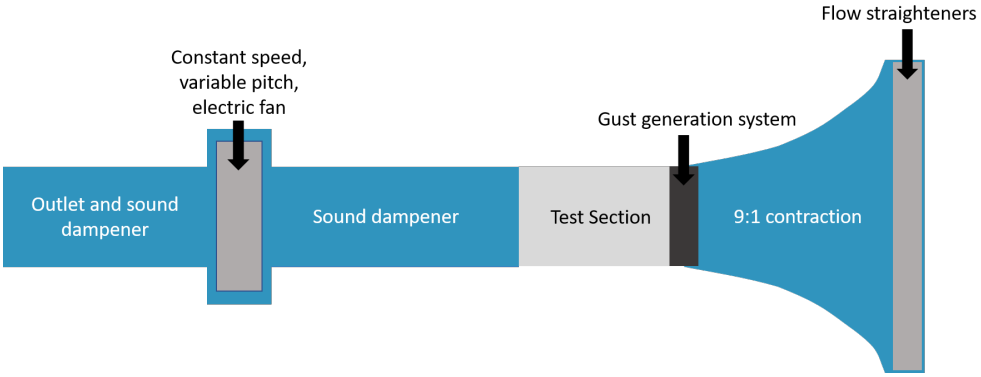

Figure 3.1: Parts, shown schematically, of the University of Washington's 3ft by 3ft low-speed wind tunnel [4]

load during operation for uniform gust field generation in the test section. The natural frequencies of the vanes, above 20 Hz, are much higher than the frequencies of interest of the aeroservoelastic models tested.

The gust profile shape and duration are specified and commanded manually through HTTP-protocol via the local network. A command signal drives an external motor to rotate the gust vanes in a way that would generate the desired gust waveform. A laser vibrometer is placed outside of the tunnel, pointing at a gust vane's trailing edge to measure its time dependent displacement, to then be translated into direct measurement of the rotational motion of the gust vanes. Figure 3.2 shows the gust vanes system schematically. The gust vanes are driven by the electric motor to move together.

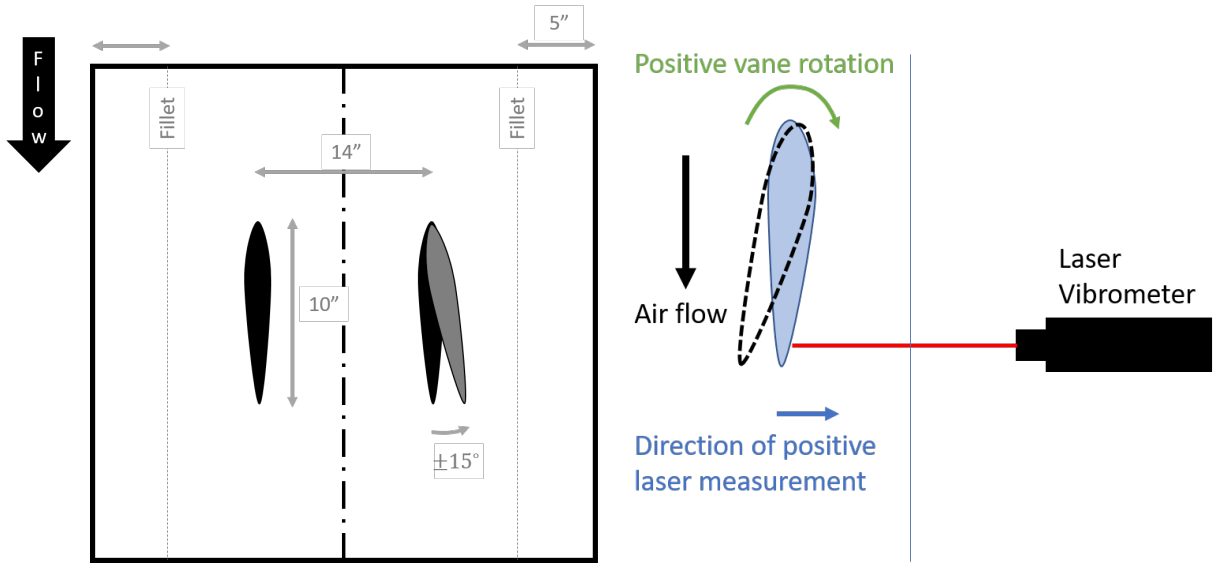

(a) Schematic Gust Vane Configuration (b) Vane-laser Measurement Configuration

Figure 3.2: Gust generation system and sensor [2]

3.3 The Aeroservoelastic Wind Tunnel Model

The MARGE, [4], was designed subject to the wind tunnel's physical constraints to capture the aeroelastic coupling of rigid-body and elastic motions of typical wing / fuselage/ tail configurations. It is a half-span wing-body-tail model mounted to the wind tunnel ceiling with the wingtip pointed down. The MARGE is made of three beams corresponding to the wing, fuselage, and tail. Both the wing and tail are covered by NACA-0012 airfoil aerodynamic shells that were 3D printed to create lifting surfaces, following the common way in which subsonic aeroelastic wind tunnel models are built. The wing is composed of a beam, five aerodynamic shells, and soft foam between shells spanwise to minimize aerodynamic leaks while preventing the shells from affecting the stiffness of the structure. The tail is made of a beam and one shell. Figure 3.3 shows the structural, aerodynamic, and systems components of the MARGE. The tip shaped mass at the wing tip can be sized

and placed to shape low-frequency modes of motion and natural frequencies. The rigid body rotation axis is at the quarter chord of the wing, allowing MARGE to pitch freely. Figure 3.4 illustrate the model mounted in the wind tunnel.

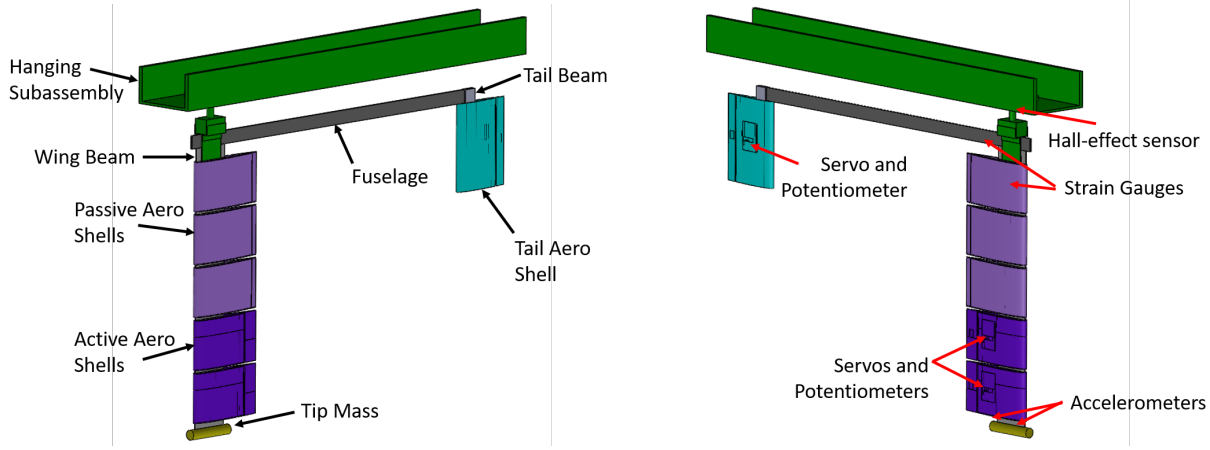

(a) Primary components (b) Sensing and actuation components

Figure 3.3: Model of aeroeslatic response to gust excitation [4]

MARGE is designed for rapid configuration changes at low-cost. The aerodynamic shells on the wing are interchangeable and could be active or passive depends on desired test configuration. That is, each aerodynamic strip along the span of the wing may or may not contain an actuator and a control surface (up to five control surfaces or no control surfaces). The tip mass can be increased or decreased, shaped to be longer or shorter from different materials, and placed forward or afterward along the wingtip chord. All beam parts (wing, fuselage, tail) can be replaced for different stiffness characteristics. The detailed structural information is provided in Table 3.1.

For the studies reported in this paper, MARGE has two wing control surfaces on the two outer shells and a single full-span elevator surface. Each control surface is driven by an MKS HV6130 servo motor mounted inside the shell. Seven on-board sensors are shown in Figure 3.3b. The rigid body pitch angle is measured by a non-contact Hall-effect sensor.

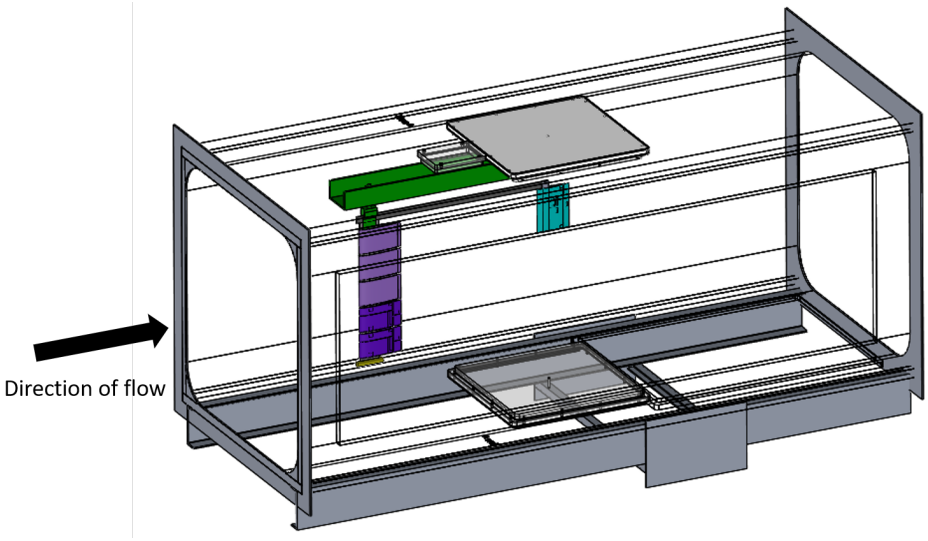

Figure 3.4: Test article, MARGE, mounted in the wind tunnel test section [4]

Table 3.1: Overview of structure components [2]

Components	Materials
Wing Beam	Aluminum 6061-T6
Tip Cylinder	Brass
Aero-Shell	Polyactic Acid (PLA)
Fuselage Beam	Low Carbon Steel
Tail Beam	Aluminum 6061-T6

(a) Materials

Components	Weight (lb)
Wing Beam	0.367
Tip Cylinder	0.276
Active Aero-Shell	0.209
Passive Aero-Shell	0.132
Fuselage Beam	0.986
Tail Beam	0.146

(b) Masses

Two accelerometers at the wing tip measure bending and torsional motions. The wing-root bending strain is measured by the strain gauge. Rotary potentiometers are installed on each control surface measuring the actual motions of the control surfaces.

3.4 Analytical/ Numerical Modelling

Commonly used techniques for generating state space models of aeroservoelastic systems are used in this work in general [43–46]. In the work presented here a LTI state-space model is determined first based on quasi-steady aerodynamic analysis of a NASTRAN finite element model of MARGE, as shown in [1]. The LTI state-space model is shown in conventional form in Equation

$$\dot{x} = Ax(t) + Bu(t) \tag{3.1}$$

where $x \in \mathbb{R}^n$ is the time-dependent state vector and $u \in \mathbb{R}^m$ is the time-dependent control vector.

The matrices of A and B are state and control matrices. The states include contributions from the angle of attack, pitch rate, and the first two second-order structural modes.

Generalized modal displacements are used to approximate the motions of the elastic structure in the reduced order basis shown below.

$$q \approx \Phi\eta \tag{3.2}$$

Φ is normal modes matrix and η is the vector of generalized modal coordinates. The system matrix partitioned as

$$A = \begin{bmatrix} A_r & A_{re} \\ A_{er} & A_e \end{bmatrix} \tag{3.3}$$

where the matrix $A_r \in \mathbb{R}^{2\times2}$ contains the linearized rigid-body dynamics and aerodynamic coefficients, the matrix $A_e \in \mathbb{R}^{4\times4}$ models the elastic linearized structural dynamics, and $A_{re} \in \mathbb{R}^{2\times4}$ and the $A_{er} \in \mathbb{R}^{4\times2}$ model coupled dynamics between linearized rigid-body and elastic dynamics, structural and aerodynamic. A detailed description of the mathematical model, with states, inputs, and outputs, and the system matrices, is given in the Appendix.

3.5 Adjusted Dynamics

The adjusted dynamics are recorded here as an LTI state-space representation where the state vector is $x \in \mathbb{R}^6$ and its elements are defined as

$$x^\intercal = \begin{bmatrix} \alpha & q & \eta_1 & \dot{\eta}_1 & \eta_2 & \dot{\eta}_2 \end{bmatrix}, \tag{3.4}$$

where α and q have units of rad and rad/s, respectively. The two modal coordinates (η_1, η_2) and their time derivatives are unitless. Any current controllers use a reduced state-space model for control design. The input vector is $u \in \mathbb{R}^4$ with elements defined as

$$u^\intercal = \begin{bmatrix} \delta_e & \delta_{OB} & \delta_{IB} & \delta_{gust} \end{bmatrix}. \tag{3.5}$$

The input matrix has been scaled such that these angular displacements (elevator displacement, outboard aileron displacement, inboard aileron displacement, and gust vane displacement, respectively) are defined in units of degrees. The observation vector is $y \in \mathbb{R}^4$ with elements of

$$y^\intercal = \begin{bmatrix} \mu\epsilon_{WR} & \theta & a_{fore} & a_{aft} \end{bmatrix}, \tag{3.6}$$

where the first output is micro-strain measured at the wing root, the second output is the pitch angle measured in degrees, and the final two outputs are accelerations measured in gees at the forward and after corners of the wingtip. The adjusted dynamics have the form of

$$\begin{aligned} \dot{x}(t) &= Ax(t) + Bu(t) \\ y(t) &= Cx(t) \end{aligned} \tag{3.7}$$

where the system matrices have the following values:

3.5.1 2018 Model

$$
A = \begin{bmatrix}
-3.588 & 2.545 & -0.00472 & 0 & -0.06629 & 0 \\
-11.71 & 0.6877 & -0.03113 & 0 & -0.2492 & 0 \\
0.04404 & 0.2006 & 0 & 1.0 & 0 & 0 \\
51.34 & 0.1776 & -83.6 & -2.377 & 1.127 & 0 \\
5.104 & 0.2788 & 0 & 0 & 0 & 1.0 \\
84.29 & 0.4278 & -0.0182 & 0 & -4363.0 & -17.18
\end{bmatrix},
$$

$$
B = \begin{bmatrix}
-0.0007152 & -2.913\,10^{-5} & 2.826\,10^{-5} & 0.0002368 \\
0.01403 & 0.0008593 & 0.0009988 & -0.0005096 \\
0.09562 & 0.02433 & 0.01614 & 0.05095 \\
-1.597 & -0.2965 & -0.2936 & -1.846 \\
0.00273 & 0.0002442 & 0.000198 & 0.0001023 \\
-0.08805 & -0.01127 & -0.00978 & -0.02487
\end{bmatrix}, \tag{3.8}
$$

$$
C = \begin{bmatrix}
-0.2852 & 0.2289 & -1804.0 & 0.001234 & -1.618\,10^{6} & 1.116 \\
382.7 & -17.28 & -4.59 & 0.06836 & -1976.0 & -2.069 \\
194.9 & 25.37 & 1.57 & 0.139 & -4334.0 & 9.407 \\
170.1 & 28.86 & 1.688 & 0.1316 & -4095.0 & 9.683
\end{bmatrix}.
$$

3.5.2 2019 Model

The input matrix is scaled that all the angular displacements are defined in units of *rad*. The μ-strain is updated to strain, and the pitch angle and angle of attack are also updated to the unit of *rad*. The observation vector is re-ordered as below.

$$
y^{\intercal} = \begin{bmatrix} a_{fore} & a_{aft} & \epsilon_{WR} & \theta \end{bmatrix}, \tag{3.9}
$$

$$
A = \begin{bmatrix}
-6.801 & 0.5644 & -0.00472 & 0 & -0.06629 & 0 \\
-96.15 & 4.024 & -0.03113 & 0 & -0.2492 & 0 \\
0 & 0 & 0 & 1 & 0 & 0 \\
-34.8 & 14.73 & -83.6 & -2.377 & 1.127 & 0 \\
0 & 0 & 0 & 0 & 0 & 1 \\
261.2 & -21.37 & -0.0182 & 0 & -4363 & -17.18
\end{bmatrix},
$$

$$
B = \begin{bmatrix}
0.5575 & 0.02004 & 0.03483 & 0.01355 \\
1.401 & 0.05154 & 0.07457 & 0.7849 \\
0.0003849 & 1.901e-05 & 1.816e-05 & -3.269 \\
-84.42 & -13.87 & -14.27 & -54.65 \\
3.511e-06 & 2.436e-08 & -1.757e-08 & 0.006003 \\
-2.636 & 0.1082 & -0.06945 & 1.889
\end{bmatrix},
\tag{3.10}
$$

$$
C = \begin{bmatrix}
-327 & 23.71 & 2.412 & -0.02055 & 5446 & 148.2 \\
-336.4 & 25.63 & 2.498 & -0.04154 & 5758 & 137.8 \\
-0.09509 & 0.009932 & -0.00169 & 0.0001562 & 1.497 & 0.07061 \\
3.613 & 0.09258 & 0.08484 & -0.009969 & -31.72 & -5.371
\end{bmatrix}.
$$

3.6 Hardware and Software Integration

There are two dedicated computers, one for the wind tunnel data acquisition (DAQ) and control and GGS command, and one for Simulink Desktop Real-Time Application and MARGE DAQ, used for the test setup. Simulink is used for both simulations and experiments. The Simulink Desktop Real-Time Application collects sensor measurements and sends actuation commands to MARGE in the wind tunnel. The dedicated desktop PC runs the real-time desktop environments and stores collected test data through a National Instrument (NI) BNC 2110 DAQ and circuit board for input and output (I/O) signals. The DAQ board processes eight channels, including seven on-board sensors and laser vibrometer with analog

filters. The measured signals are filtered and then could be further estimated by a Kalman filter. The flow chart of the closed-loop control process is shown in Figure 3.5.

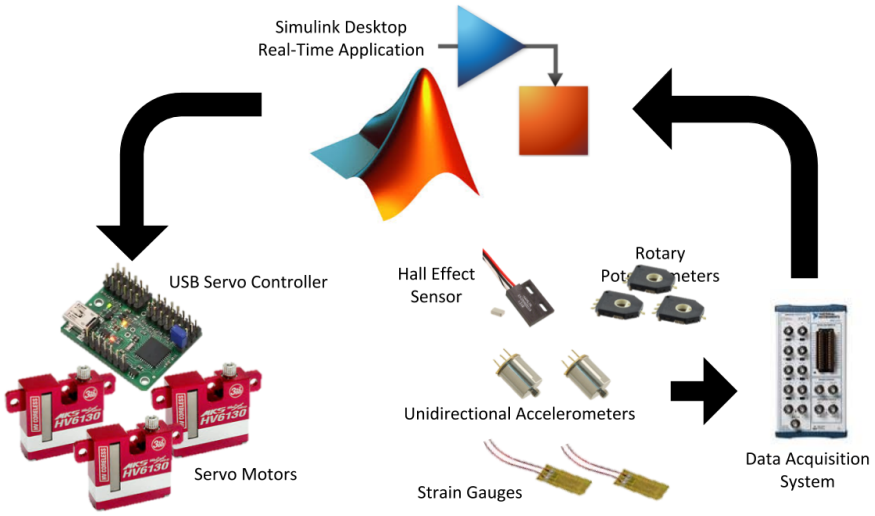

Figure 3.5: Signal flow in servo command and measurement loop [2]

3.7 Closed-loop Setup

Two general block diagrams for control loop setup are given in Figure 3.6.

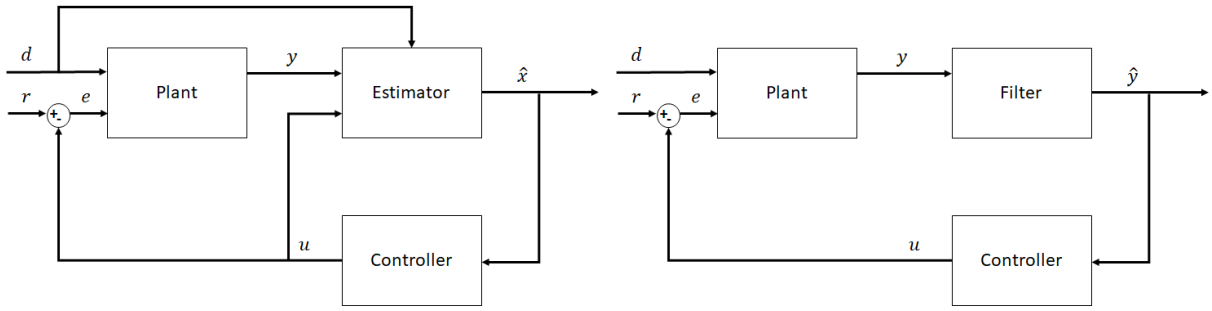

(a) State feedback (b) Output feedback

Figure 3.6: Block diagram of closed-loop feedback setup

For state feedback, a Kalman filter is used for state estimation. The filter takes observed outputs and control inputs, and return estimated states for state-feedback control. During experiments, a linear Kalman filter with covariances identified from prior steady output measurements was used. The linear Kalman filter is introduced in Section 2.2 and referenced in [34]. For output feedback, the output filters are used to roll off high-frequency contents. Band-pass filter are used for accelerometers eliminating low-frequency drift. Detailed filter information are given in Section 5.1.

The block diagrams given in Figure 3.6 are also the representation of the control loop implementation in Simulink. The plant is modelled as a LTI system described in Section 3.5. The state-feedback control use estimated states by the Kalman filter and output-feedback control uses filtered outputs. The selected signals are fed in the control block where an active controller is selected from a variety of control methods. The control inputs and the disturbance inputs from each respective blocks are then fed back to the plant. For feedback setup, Figure 3.6 illustrates both state and output feedback where no preview gust signals are given to controller nor estimator. Figure 3.7 shows the preview setup that the defined finite preview information are sent to estimator in state feedback and to controller for both preview configurations.

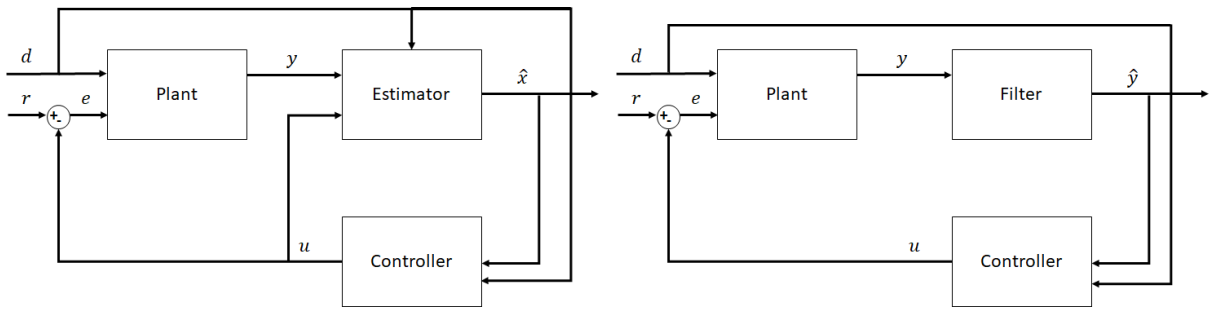

(a) State feedback (b) Output feedback

Figure 3.7: Block diagram of closed-loop preview setup

3.8 Chapter Summary

This chapter details the experimental setup on the aeroservoelastic model, wind tunnel, and the GGS. Furthermore, the analytical and numerical modelling of the MARGE model is given and incorporated in the Simulink environment for real-time control implementation. Block diagrams of both feedback and preview control are presented in Section 3.7. Chapter 4 extends the feedback control of H_2 and H_∞ method presented in Section 2.3 accounting the preview information in a systematic approach for real-time preview control.

Chapter 4

CONTROLLER DESIGN AND SYNTHESIS

This chapter presents a systematic approach for formulation of preview H_2 and H_∞ controller. The approach includes the normalization of the dynamical system, construction of the generalized plant, weighting selection, preview augmentation, and finally rescaling of the normalized system. The normalization is critical for model analysis and controller design because of the physical and allowed magnitude. The process of constructing the generalized plant and weight selection is usually done in a single step. This chapter separates the process detailing each step: construction of the generalized plant specifies regulated channels and formulates the control problem, and weight selection penalizes the regulated channels to achieve desired performance. The weight selection is also coupled with preview augmentation for achieving desired preview performance. The discrete preview augmentation formulates the preview problem to be solved in standard H_2 and H_∞ feedback control synthesis as described in Section 2.3. Lastly, once the controller is synthesized, the controller requires rescaling before implementation on the original system. The details are discussed in [23–25, 41].

4.1 Normalization

The importance of normalization is in the practical application of model analysis and controller design. The control problem has required performance and limitation. The normalization process constraints the allowed magnitude in both input and output signals. It gives signals physical representation and allows input and output signals to be on the same scaling. Thus, later in the weight selection process, the closed-loop magnitudes have physical meanings.

Assume the system has the form as in Equation 2.17 with additional disturbance transfer function shown as following

$$\hat{y} = \hat{G}\hat{u} + \hat{G}_d\hat{d} \tag{4.1}$$

where the hat (ˆ) represents unscaled variables. The block diagram of such system is illustrated in Figure 4.1.

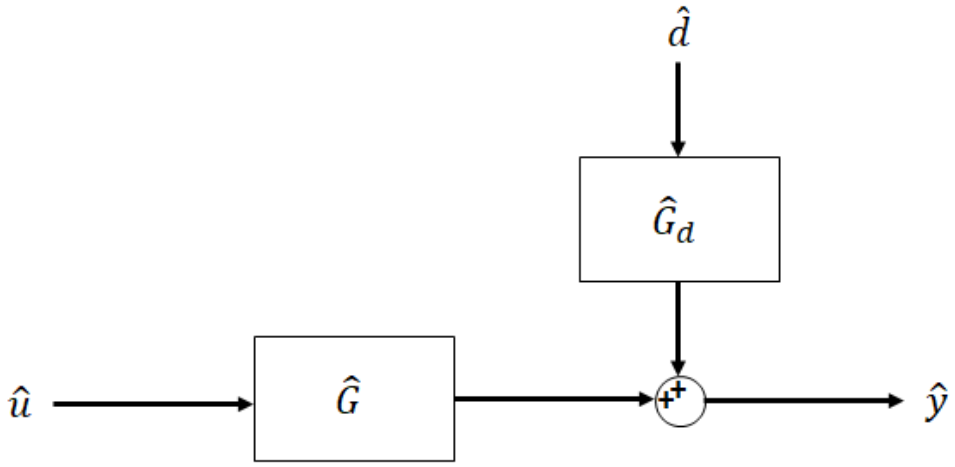

Figure 4.1: Block diagram of unscaled system

The approach in scaling is to normalize the variables to less than one in magnitude, < 0 dB, by dividing each variable by their maximum expected or allowed values. For the disturbance and control input, the scaled variables are are as below

$$d = \hat{d}/\hat{d}_{\max}, \qquad u = \hat{u}/\hat{u}_{\max} \tag{4.2}$$

where $\hat{d}_{\max}$ and $\hat{u}_{\max}$ are the largest expected change in disturbance and the largest allowed input change, respectively. The output variable is divided by its corresponding maximum value.

$$y = \hat{y}/\hat{y}_{\max} \tag{4.3}$$

To generalize scaling, the scaling factors are defined as

$$D_d = \hat{d}_{\max}, \qquad D_u = \hat{u}_{\max}, \qquad D_y = \hat{y}_{\max} \tag{4.4}$$

For MIMO systems, each variable has a different maximum value such that D_d, D_u, and D_y become diagonal scaling matrices. The normalization process ensures that all outputs are equally weighted in magnitudes. By combing Equations 4.2 and 4.4, it becomes

$$d = D_d^{-1}\hat{d}, \qquad u = D_u^{-1}\hat{u}, \qquad y = D_y^{-1}\hat{u} \tag{4.5}$$

By substituting Equation 4.5 in 4.1, the transfer function is

$$D_y y = \hat{G} D_u u + \hat{G}_d D_d d \tag{4.6}$$

where the block diagram in Figure 4.1 becomes as shown in Figure 4.2.

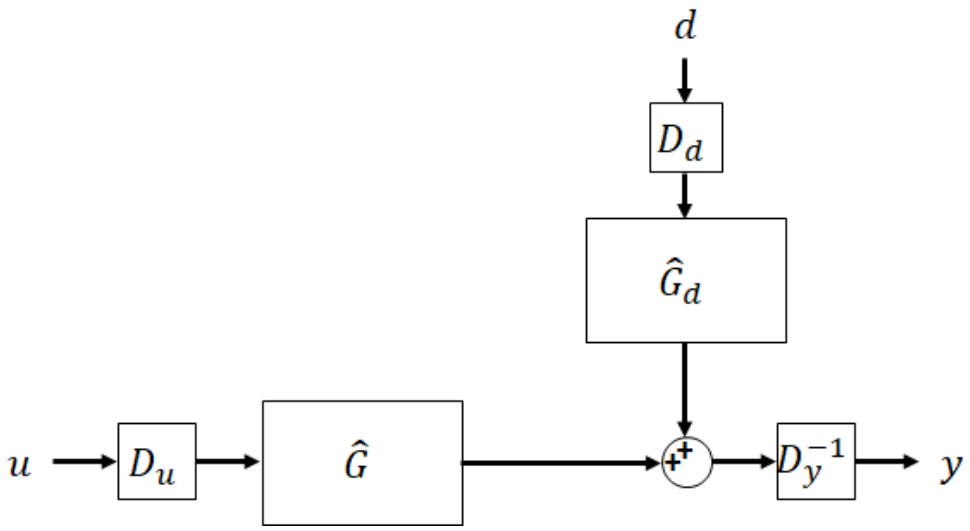

Figure 4.2: Block diagram of normalized signals

By multiplying the inverse of D_y on both side, the normalized signals are

$$y = D_y^{-1}\hat{G} D_u u + D_y^{-1}\hat{G}_d D_d d \tag{4.7}$$

where the normalized transfer functions are

$$G = D_y^{-1}\hat{G}D_u, \qquad G_d = D_y^{-1}\hat{G}_d D_d \tag{4.8}$$

The block diagram of the normalized signals and transfer functions are shown in Figure 4.3.

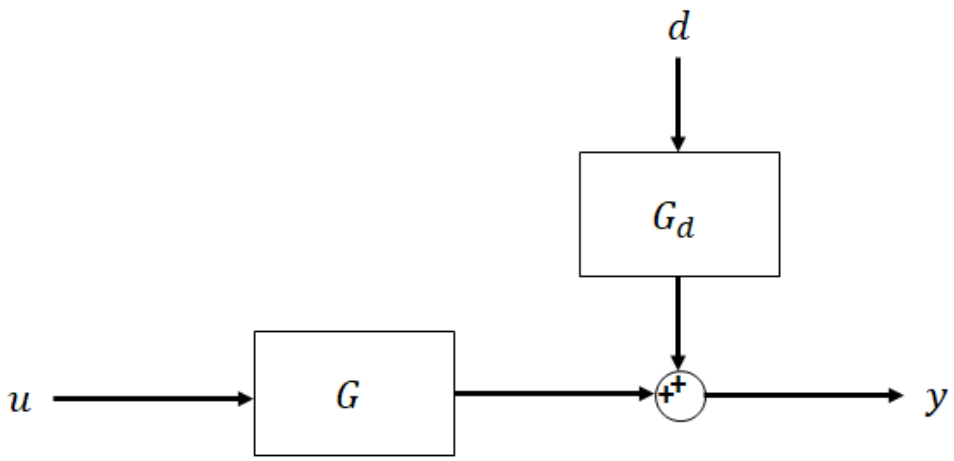

Figure 4.3: Block diagram of normalized system

As an example of MARGE in Section 3.5, the model is an LTI system that has a form in Equation 3.7, and the disturbance input is modeled as an control input in the B matrix. The scaling omits the $\hat{G}_d$ term in Equation 4.1 and the scaling matrices for 2019 model are

shown as following

$$D_u = \begin{bmatrix} \delta_{e,max} & 0 & 0 & 0 \\ 0 & \delta_{OB,max} & 0 & 0 \\ 0 & 0 & \delta_{IB,max} & 0 \\ 0 & 0 & 0 & \delta_{gust,max} \end{bmatrix},$$
$$D_e = \begin{bmatrix} a_{fore,max} & 0 & 0 & 0 \\ 0 & a_{aft,max} & 0 & 0 \\ 0 & 0 & \epsilon_{WR,max} & 0 \\ 0 & 0 & 0 & \theta_{max} \end{bmatrix} \tag{4.9}$$

4.2 Construction of Generalized Plant

By constructing the generalized plant, the problem can be solved in the standard H_2 and H_∞ control problem that is in Section 2.3.2. The general dynamical system has the form in Equations 2.16 and 2.17. The transfer matrix of the generalized plant in Equation 2.18 can be represented in the continuous state-space form in Equation 2.19 and discrete state-space form in Equation 4.10.

$$\begin{aligned} x_{k+1} &= Ax_k + B_1 d_k + B_2 u_k \\ z_k &= C_1 x_k + D_{11} d_k + D_{12} u_k \\ y_k &= C_2 x_k + D_{21} d_k + D_{22} u_k \end{aligned} \tag{4.10}$$

where the index k is the time step and the dimensions of each signals remain the same.

The H_2 and H_∞ control problem minimize energy, $||T_{zw}||_2$, and peak response, $||T_{zw}||_\infty$, respectively, from disturbance input to regulated outputs. By constructing the generalized plant, the norm of the transfer matrix from specified exogenous input to regulated outputs can be minimized. There are multiple approaches to constructing a generalized plant. This paper presents the LQR and signal-based method. The MARGE is used as an example detailing the construction process, and the state-space representations of MARGE are in Section 3.5.

4.2.1 LQR

The H_2 optimization of LQG is presented in Section 2.3.3. The MARGE Simulink setup has Kalman filter such that the estimation of states and filter of noise are excluded from the formulation. Furthermore, by the separation principle, the controller and observer can be designed separately. The A matrix in MARGE remains the same for the generalized plant. The analytical model of MARGE is modeled with the disturbance input in the B matrix. The goal of gust load alleviation is minimizing disturbance effect on the system such that the B_1 matrix is the last column vector of the B matrix in Equation 3.8 for the 2018 model and Equation 3.10 for the 2019 model. The elevator is used for trim flight and is not employed for gust load alleviation actuation. The disturbance input and control input matrices are

$$B_1 = \begin{bmatrix} \delta_{gust} \end{bmatrix}, \qquad B_2 = \begin{bmatrix} \delta_{OB} & \delta_{IB} \end{bmatrix} \tag{4.11}$$

Equation 2.42 relates LQR cost with H_2 regulated output, and Equation 2.43 shows the regulated output of H_2 with LQR weighting. The LQR weights in H_2 optimization are square root of Q and R and the size of regulated output, $z(t)$, is state variables plus control variables, $p = n + m$. With Kalman filter, the setup uses full-state feedback where the observation matrix is identity. The generalized plant is shown in Equation 4.12.

$$G(s) = \left[\begin{array}{c|cc} A & B_1 & B_2 \\ \hline \begin{bmatrix} Q^{\frac{1}{2}} \\ 0 \end{bmatrix} & 0 & \begin{bmatrix} 0 \\ R^{\frac{1}{2}} \end{bmatrix} \\ I & 0 & 0 \end{array}\right] \tag{4.12}$$

4.2.2 Signal-based

The signal-based method is like LQR in the previous subsection. The state dynamic, $\dot{x}(t)$, remains the same as in Section 4.2.1. The observed outputs, $y(t)$, could be full-state or output feedback depending on the system setup. The full-state feedback has an identity matrix, and the output feedback has an observation matrix in C_2. The control law designer

chooses the outputs to be regulated in $z(t)$. The results presented in Sections 5.3 and 5.4 have the regulated outputs of wing-root strain, as well as outboard, and inboard ailerons.

$$z(t) = \begin{bmatrix} \epsilon_{WR} & \delta_{OB} & \delta_{IB} \end{bmatrix}^{\intercal} \tag{4.13}$$

With output feedback, the generalized plant becomes

$$G(s) = \left[\begin{array}{c|cc} A & B_1 & B_2 \\ \hline \begin{bmatrix} \epsilon_{WR} \\ 0 \end{bmatrix} & 0 & \begin{bmatrix} 0 \\ I \end{bmatrix} \\ C_2 & 0 & 0 \end{array}\right] \tag{4.14}$$

where ϵ_{WR} is the strain measurement in the second last row of matrix C in Equation 3.10. The identity matrix in D_{12} assigns equal weights to outboard and inboard ailerons. C_2 matrix is the observation matrix C in Equation 3.10 for output feedback.

Note that it is important to minimize at least one performance channel and control channel. The performance channels refer to the Q in LQR setup and ϵ_{WR} in this section. The Q weights the state performance and the ϵ_{WR} directly specified interested output performance. If only performance channels are minimized, the controller synthesis assume unlimited control authority and the control signal would be out of bound. Vice versa that if only the control channels are minimized, then no control will be commanded.

4.3 Weighting Selection

After the construction of the generalized plant, the regulated outputs are selected for weight tune. The weightings of the regulated outputs penalize the output performance. The higher the weighting is, the less response of the output is performed. For LQR weights, the higher the weights in the Q matrix penalize the state performance suppressing the state response to gust excitation in this paper; contrarily, the higher the weights in the R matrix penalize the control inputs prohibiting ailerons actuation. Therefore, the combination of the Q and R matrix yields quadratic weighted state and control performance. Worth noting that the LQR

weight tune usually does not involve the normalization process such that the tuning process is arbitrary and performance-dependent. The LQR weights impose no frequency restriction; however, in the H_2 setup, frequency weight is achievable.

In the signal-based method, two results presented in Chapter 5 are static weighted and frequency weighted wing-root strain with frequency weighted ailerons. In this process, normalization is required for efficient controller design and meaningful closed-loop responses. The closed-loop responses are normalized such that the responses of the system are represented in terms of maximum expected or allowed values. Here the wing-root strain is normalized by the maximum open-loop response value so that the closed-loop responses directly yield a comparison between closed-loop and open-loop responses. The normalized control surface actuation is bounded by maximum allowed rotations. As a result, the weight selection with normalized regulated outputs makes the tuning process and closed-loop responses intuitive.

The static and frequency weighting are choices of the designer. The static weighting penalizes the same weight across all frequencies, while frequency weighting penalizes depending on filter types. The frequency weighting high-pass filters are usually applied on the control inputs to constrain the bandwidth and force the input response to roll off with actuators' limitation. The high-pass filters are applied to both ailerons penalizing the high-frequency dynamics. As mentioned above, the static weighted and frequency weighted signal-based methods are tested. The reason is that the updated 2019 model has the second wing bending response higher than the first wing bending response. The H_∞ controller is designed to suppress maximum response but is constrained by the frequency weight on the ailerons. The H_∞ norm measures the supremum norm of of the transfer matrices of the exogenous inputs to the regulated outputs. Although the H_∞ controller minimizes the first wing bending mode, the H_∞ norm is measured at the second wing bending mode. Therefore, the additional low-pass filter is applied to the wing-root strain channel to roll off the second wing bending mode, allowing the first wing bending performance to be measured.

The work presented in the paper is done in MATLAB and Simulink environments. This

paragraph denotes a brief tutorial on the weights implementation. The LQR weights in Equation 4.12 could be done by constructing the generalized plant and assigning the weights diagonally in the Q and R matrix. The general static weights are done in the same way multiplying the weights in the row of C_1, D_{11}, and D_{12} matrix. The mixed static and frequency weights require a different approach. The frequency weights can be specified with the *makeweight* function in MATLAB Robust Control Toolbox [42] and the static weight can be specified with the *ss(0,0,0,W,dt)* function with respective weight W and sample time dt. The weights are then connected in the generalized plant with respect to the corresponding regulated outputs via *append* and *connect* functions in MATLAB Control System Toolbox [47]. The resulted plant has the order of the original system plus the order of the weighting applied. The output filters could also be included in the generalized plant to increase the fidelity of the system with the same method. Note that the frequency weights and filters need to have the same sample time as the original system to form the generalized plant in MATLAB.

4.4 Preview Augmentation

This section incorporates the preview information in the feedback system. MARGE has no LIDAR on-board for generating the preview disturbance signal, which uses the GGS command signal loop prior to the actuation. The finite preview signal is modeled as a discrete dynamic system whose states include discrete preview information embedded in the generalized plant. The discrete preview augmentation formulates the preview problem for solution by standard H_2 and H_∞ feedback control synthesis. Takaba presents a tutorial on the preview control system with full-state feedback in [33]. The feedback and preview control configurations are shown in Figure 4.4.

Khalil and Fezan's work in [23–25] are inspired by [33, 38] solving the preview problem in full information structure as in Section 2.3. The differences between the two methods are subtle. In Takaba's setup, the reformulate disturbance is unknown such that D_{22} matrix is zeros violating Riccati solution assumption in Section 2.3. Khalil and Fezan's work redefines

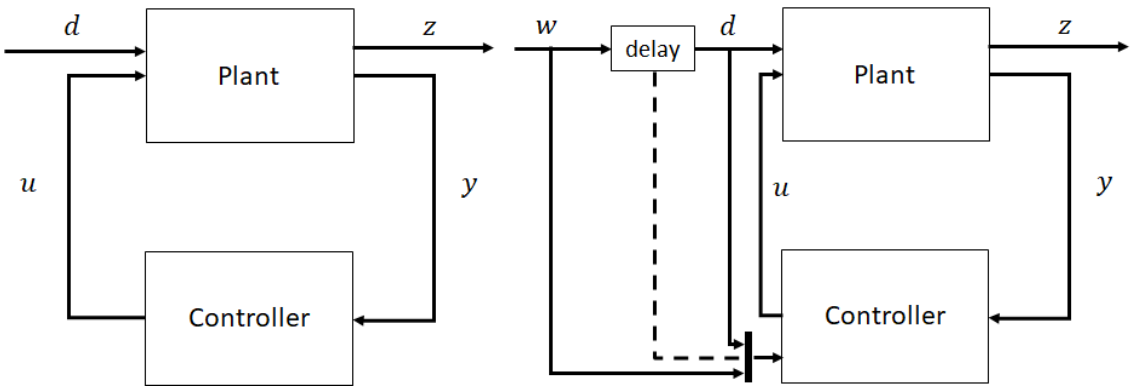

(a) Feedback Control (b) Preview Control

Figure 4.4: General Control Configuration

the disturbance to be the last known preview information which satisfies the assumptions for Riccati's solution. The disturbance dynamic matrix of Khalil and Fezan's is one order less than Takaba's setup. After the formulation, the full-order H_2 and H_∞ controller can be synthesized with *h2syn* and *hinfsyn* functions and the fixed-order H_∞ controller can be synthesized with *hinfstruct* function in MATLAB Robust Control Toolbox [42]. The subsections below summarize both setups.

4.4.1 Takaba's Approach

Assume the system has the form in Equation 4.10, and the following assumptions are made for the system.

1. (A, B) is stabilizable.
2. $\begin{bmatrix} A - e^{j\theta} I & B \\ C & D \end{bmatrix}$ has full column rank for any $\theta \in [0, 2\pi)$.
3. The preview information from d_k up to d_{k+h} are available for control. h is a nonnegative constant that is called the preview length.

The detailed preview control configuration is shown in Figure 4.5.

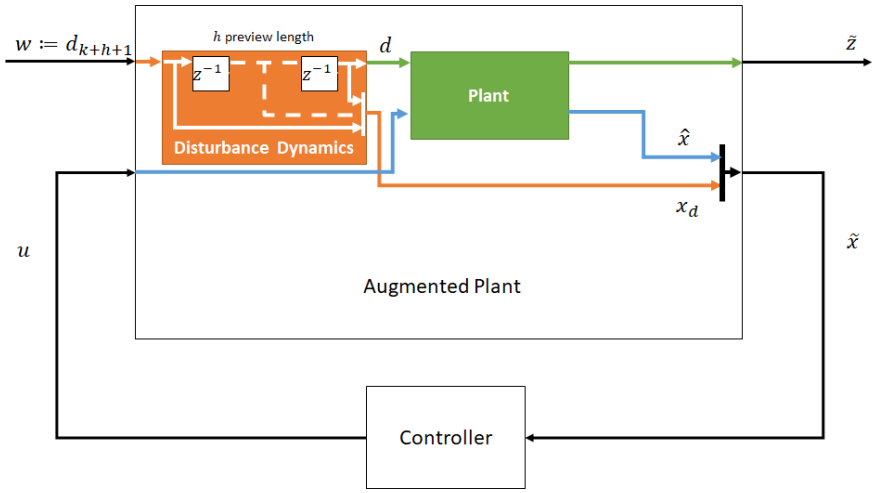

Figure 4.5: Takaba's preview control configuration

The disturbance is redefined as

$$d_{p,k} := d_{k+h+1}. \tag{4.15}$$

where the redefined disturbance is not observed and unknown.

Substitute Equation 4.22 in discrete state-space form, and obtain

$$\begin{aligned} x_{k+1} &= Ax_k + B_1 d_{p,k-h-1} + B_2 u_k \\ z_k &= C_1 x_k + D_{11} d_{p,k-h-1} + D_{12} u_k \\ y_k &= C_2 x_k + D_{21} d_{p,k-h-1} + D_{22} u_k \end{aligned} \tag{4.16}$$

The disturbance vector is redefined from Equation 4.22,

$$x_{d,k} = \begin{bmatrix} d_k \\ d_{k+1} \\ \vdots \\ d_{k+h} \end{bmatrix} = \begin{bmatrix} d_{p,k-h-1} \\ d_{p,k-h} \\ \vdots \\ d_{p,k-1} \end{bmatrix} \in \mathcal{R}^{l\times(h+1)} \tag{4.17}$$

where the disturbance dynamic are modeled as

$$x_{d,k+1} = A_d x_{d,k} + B_d d_{p,k} = \begin{bmatrix} 0 & I & & O \\ & 0 & \ddots & \\ & & \ddots & I \\ O & & & 0 \end{bmatrix} x_{d,k} + \begin{bmatrix} 0 \\ 0 \\ \vdots \\ I \end{bmatrix} d_{p,k} \tag{4.18}$$

The new state vector is the original state vector augmented with known previewed disturbance states, $\tilde{x}_k = \begin{bmatrix} x_k^\intercal & x_{d,k}^\intercal \end{bmatrix}^\intercal$, and the augmented dynamics with partitions are

$$\begin{aligned} \tilde{x}_{k+1} &= \begin{bmatrix} A & B_1 & 0 \\ 0 & & A_d \end{bmatrix} \begin{bmatrix} x_k \\ x_{d,k} \end{bmatrix} + \begin{bmatrix} 0 \\ B_d \end{bmatrix} d_{p,k} + \begin{bmatrix} B_2 \\ 0 \end{bmatrix} u_t \\ \tilde{z}_k &= \begin{bmatrix} C & 0 & 0 \end{bmatrix} \begin{bmatrix} x_k \\ x_{d,k} \end{bmatrix} + D_{11} d_{p,k} + D_{12} u_k \\ \tilde{y}_k &= \begin{bmatrix} I \end{bmatrix} \begin{bmatrix} x_k \\ x_{d,k} \end{bmatrix} + \begin{bmatrix} 0 \end{bmatrix} d_{p,k} + \begin{bmatrix} 0 \end{bmatrix} u_k \end{aligned} \tag{4.19}$$

The formulation allows the preview problem to be solved in as standard H_2 and H_∞ problem as in Equation 4.10

$$\begin{aligned} \tilde{x}_{k+1} &= \tilde{A}\tilde{x}_k + \tilde{B}_1 d_{p,k} + \tilde{B}_2 u_k \\ \tilde{z}_k &= \tilde{C}_1 \tilde{x}_k + \tilde{D_{11}} d_{p,k} + \tilde{D_{12}} u_k \\ \tilde{y}_k &= \tilde{C}_2 \tilde{x}_k + \tilde{D_{21}} d_{p,k} + \tilde{D_{22}} u_k \end{aligned} \tag{4.20}$$

The generalized plant of the preview problem is

$$\hat{\tilde{G}} = \left[\begin{array}{c|cc} \tilde{A} & \tilde{B}_1 & \tilde{B}_2 \\ \hline \tilde{C}_1 & \tilde{D}_{11} & \tilde{D}_{12} \\ \tilde{C}_2 & \tilde{D}_{21} & \tilde{D}_{22} \end{array}\right] \tag{4.21}$$

4.4.2 Khalil and Fezan's Approach

Assume the system has the form in Equation 4.10 and the same assumption as in Takaba's work. The detailed preview control configuration is shown in Figure 4.6.

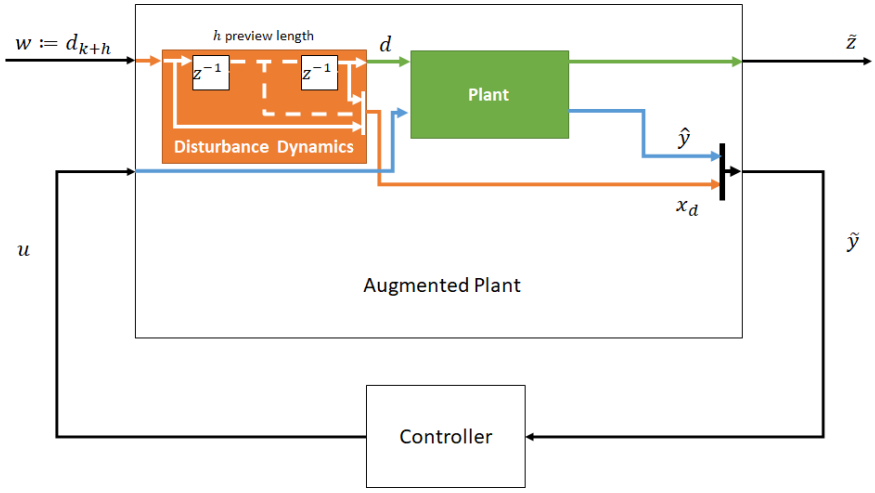

Figure 4.6: Khalil and Fezan's preview control configuration

The disturbance is redefined as

$$w_k := d_{k+h}. \tag{4.22}$$

where the redefined disturbance is observed and known.

Substitute Equation 4.22 in discrete state-space form, and obtain

$$\begin{aligned} x_{k+1} &= Ax_k + B_1 d_{p,k-h} + B_2 u_k \\ z_k &= C_1 x_k + D_{11} d_{p,k-h} + D_{12} u_k \\ y_k &= C_2 x_k + D_{21} d_{p,k-h} + D_{22} u_k \end{aligned} \tag{4.23}$$

The disturbance vector is redefined from Equation 4.22,

$$x_{d,k} = \begin{bmatrix} d_k \\ d_{k+1} \\ \vdots \\ d_{k+h} \end{bmatrix} = \begin{bmatrix} d_{p,k-h} \\ d_{p,k-h+1} \\ \vdots \\ d_{p,k-1} \end{bmatrix} \in \mathbb{R}^{l \times h} \tag{4.24}$$

which the disturbance vector is one less than Takaba's formulation. The disturbance dynamic

is the same as in Equation 4.18, but the outputs are further modeled.

$$\begin{aligned} x_{d,k+1} &= A_d x_{d,k} + B_d w_k \\ y_{d,k} &= C_d x_{d,k} + D_d w_k \end{aligned} \tag{4.25}$$

The disturbance dynamic matrices are partitioned with sizes of

$$A_d = \left[\begin{array}{c|c} 0_{h-1\times 1} & I_{h-1\times h-1} \\ \hline 0 & 0_{1\times h-1} \end{array}\right], B_d = \left[\begin{array}{c} 0_{h-1\times l} \\ \hline I \end{array}\right], C_d = \left[\begin{array}{c} I_{h\times h} \\ \hline 0_{1\times h} \end{array}\right], D_d = \left[\begin{array}{c} 0_{h\times l} \\ \hline I \end{array}\right] \tag{4.26}$$

The augmented state vector is the same, $\tilde{x}_k = \begin{bmatrix} x_k^\intercal & x_{d,k}^\intercal \end{bmatrix}^\intercal$, and the augmented dynamics with partitions are

$$\tilde{x}_{k+1} = \left[\begin{array}{c|cc} A & B_1 & 0_{n\times h-1} \\ \hline 0_{h\times n} & \multicolumn{2}{c}{A_d} \end{array}\right] \begin{bmatrix} x_k \\ x_{d,k} \end{bmatrix} + \left[\begin{array}{c} 0_{n\times l} \\ \hline B_d \end{array}\right] d_{p,k} + \left[\begin{array}{c} B_2 \\ \hline 0_{h\times m} \end{array}\right] u_k \tag{4.27}$$

$$\tilde{z}_k = \left[\begin{array}{c|cc} C & D_{11} & 0_{p\times h-1} \end{array}\right] \begin{bmatrix} x_k \\ x_{d,k} \end{bmatrix} + \begin{bmatrix} 0_{p\times l} \end{bmatrix} d_{p,k} + D_{12} u_k \tag{4.28}$$

$$\tilde{y}_k = \left[\begin{array}{c|cc} C_2 & D_{21} & 0_{q\times h-1} \\ \hline 0_{h+1\times n} & \multicolumn{2}{c}{C_d} \end{array}\right] \begin{bmatrix} x_k \\ x_{d,k} \end{bmatrix} + \left[\begin{array}{c} 0_{q\times l} \\ \hline D_d \end{array}\right] d_{p,k} + \left[\begin{array}{c} D_{22} \\ \hline 0_{h+1\times m} \end{array}\right] u_k \tag{4.29}$$

The resulted state-space model and generalized plant are the same as in Equation 4.20 and 4.21.

4.5 Closed-loop and Controller

After the MATLAB functions synthesize the controller, the controller and closed-loop system require post-processing. The synthesized controller is the normalized controller. The MATLAB functions output controller, closed-loop system, and norm values. The output closed-loop system is not the actual closed-loop system because the generalized plant input to the function is weighted. Therefore, the normalized closed-loop are linear fractional transformed with both normalized controller and unweighted normalized plant. To obtain the original closed-loop system, the normalized controller requires re-scaling similar to the

normalization process shown in Equation 4.31. The normalized closed-loop systems of feedback and preview configurations are shown in Figure 4.4 and the normalization process are introduced in Section 4.1. Figure 4.7 shows the scaling matrices of input and output signals of the normalized plant.

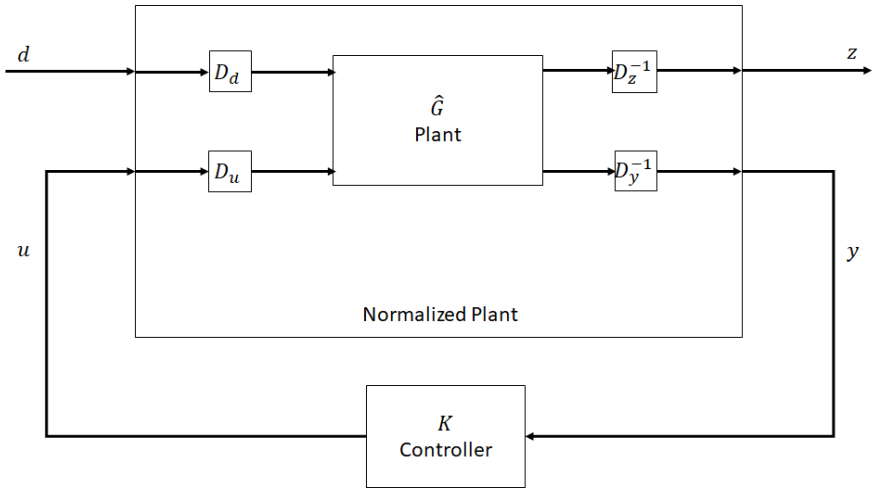

Figure 4.7: Normalized augmented plant

By scaling each normalized signals with their scaling matrices in Section 4.1, the original closed-loop system and controller are shown in Figure 4.8.

The scaled controller is

$$\hat{K} = D_u K \tilde{D}_y^{-1} \tag{4.30}$$

where D_u is the control input scaling matrix and $\tilde{D}_y$ is output scaling matrix of the system. For feedback configuration, the output scaling matrix is the observed output scaling matrix, D_y. For preview configuration, the discrete preview information is augmented in the state dynamics such that the output scaling matrix, $\tilde{D}_y$, increases in size with respect to preview length. The output scaling matrix is as following

$$\tilde{D}_y = \begin{bmatrix} D_y & 0 \\ 0 & D_d I \end{bmatrix} \tag{4.31}$$

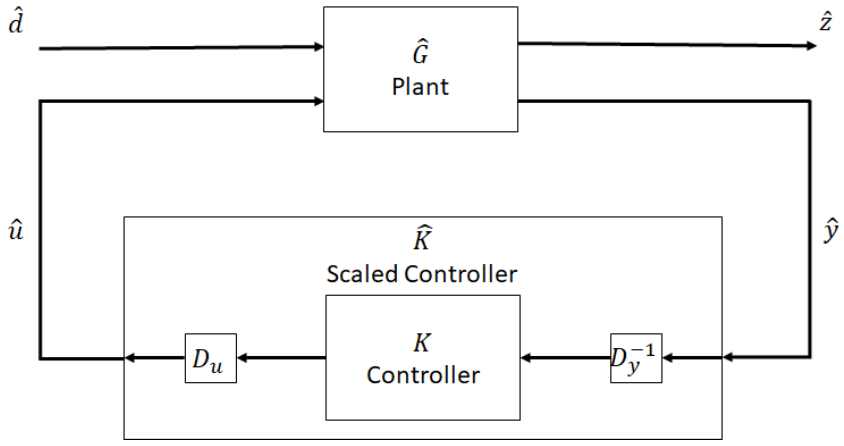

Figure 4.8: Original augmented plant

where D_d is the disturbance scalar value. The identity matrix has the size of $\mathbb{R}^{hxh}$ of given h preview information. After the re-scaling is done, the original closed-loop system can be obtained through linear fractional transformation as the normalized closed-loop with the original system and scaled controller.

4.6 Chapter Summary

This chapter details the systematic approach for preview H_2 and H_∞ controller formulation. The importance of normalization process, construction of generalized plant and weight selection are discussed. The preview formulation augmented the known discrete preview information in the plant such that the preview problem can be solved as standard H_2 and H_∞ problem as in Section 2.3. At the last, the synthesized controller is require rescale before implementation. The next chapter presents and compares both simulated and experimental results of feedback and preview controls.

Chapter 5

RESULTS

In the following chapter, the simulated and experimental results are presented. The simulations were conducted in the Simulink environments where the master files are stored on GitHub's repository. The wind tunnel tests were performed at the 3ft by 3ft low-speed wind tunnel at the University of Washington using the MARGE model described earlier. The goals of the tests were to demonstrate the feasibility of the preview benefiting H_2 and H_∞ controller and to study and compare performance. Three weighting setups are presented in the order of tested timeline, LQR weight, static weight in wing-root strain, and frequency weight in wing-root strain. In each subsection, frequency and time responses of the closed-loop system with summary plots are presented. In the figures, FB stands for feedback control and PC stands for preview control with following preview duration.

5.1 Open-Loop

The system dynamics were updated in Summer 2019. The 2018 and 2019 models are introduced in Section 3.5. The output filters are applied to roll off high-frequency contents. Band-pass filters are used for accelerometers eliminating low-frequency drift. The details of filters are tabulated in Table 5.1 and the bode plot of the filters is shown in Figure 5.1.

Figure 5.2 shows the bode plot of the transfer function of the gust disturbance to the wing-root strain, whose norm is desired to be minimized, of the 2018 model, 2019 model, and with filters.

Figure 5.3 shows the normalized response of the gust disturbance to the wing-root strain according to the normalization process is described in Section 4.1. The goal is to minimize the wing-root strain response less than the maximum allowed value which is used to normalize

Table 5.1: Output filters

Channel	Filter Type	Order	Frequency (Hz)
Forward Accelerometer	Band-pass Butterworth	3rd	0.5, 20
Afterward Accelerometer	Band-pass Butterworth	3rd	0.5, 20
Wing-root Strain	Low-pass Butterworth	2nd	15
Hall Effect Sensor	Low-pass Butterworth	2nd	10

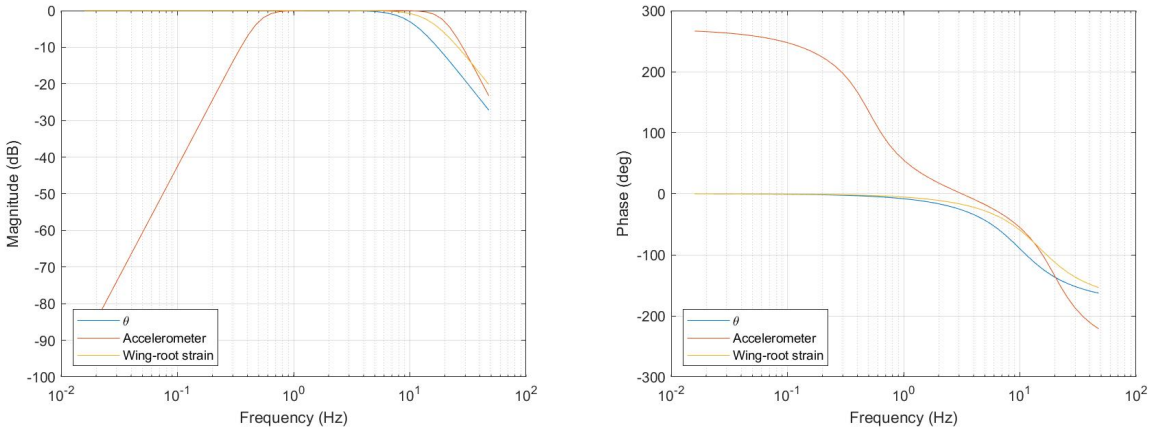

(a) Magnitude plot

(b) Phase plot

Figure 5.1: Bode plot of output filters

the signal.

Figure 5.4 shows both simulation and experimental results of wing-root strain response to gust excitation. The gust profile is a 1-cos gust of present amplitude and period. Figure 5.4b shows the effect of the wind tunnel's turbulence. The deterministic result from simulation does not account for this effect in the cases studied here, although this effect can be added to the simulations using conventional techniques of modeling the effects of random and discrete gusts on aeroservoelastic systems [48–50]. The OL and R in legends stand for open-loop and run number.

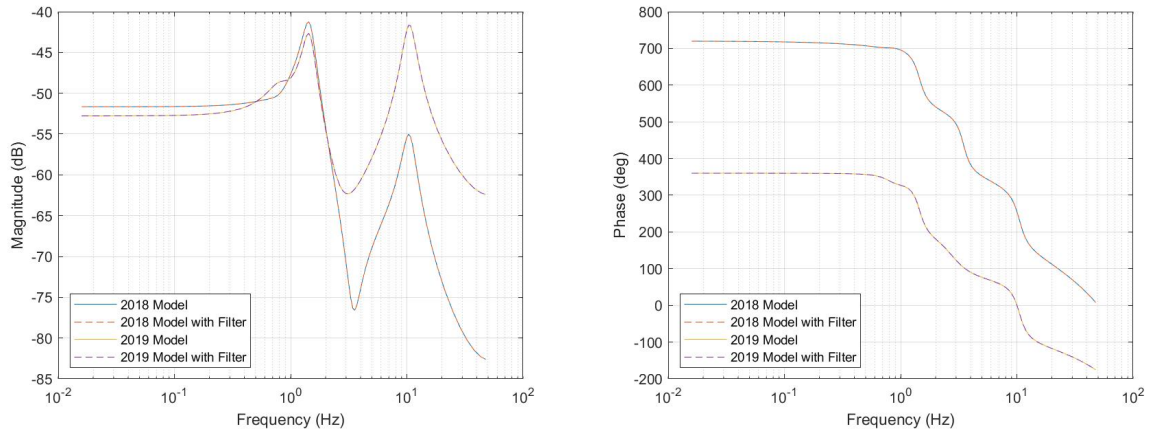

(a) Magnitude plot (b) Phase plot

Figure 5.2: Bode plot of wing-root strain response to gust excitation

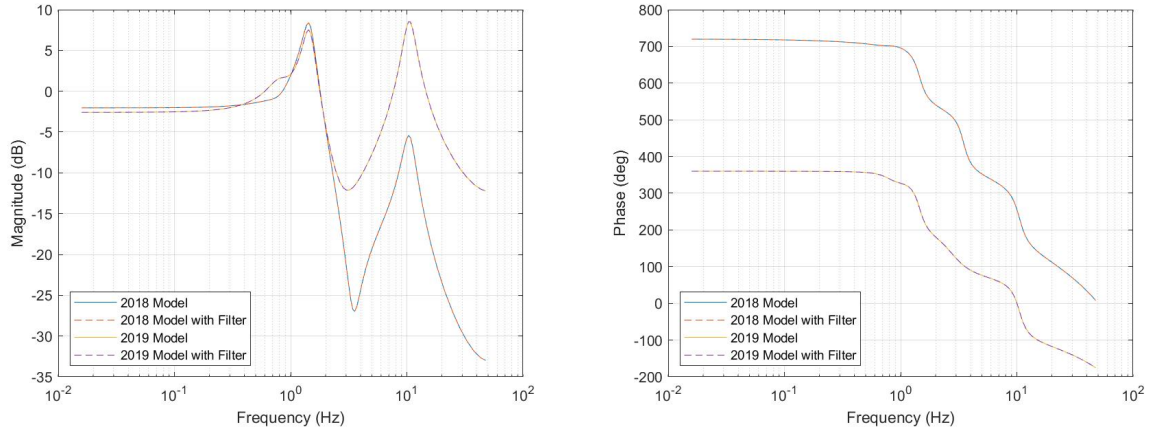

(a) Magnitude plot (b) Phase plot

Figure 5.3: ode plot of normalized wing-root strain response to normalized gust excitation

5.2 State Feedback: LQR Weighting

The LQR weights are designed with the 2018 model as part of the prior work in [2, 4]. The closed-loop system is full-state feedback consisting of output filers and Kalman filter where

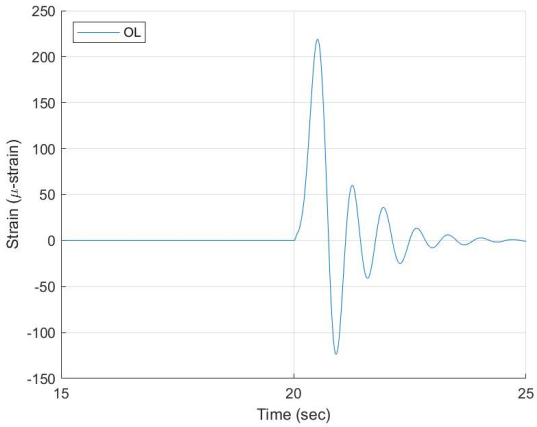

(a) Simulation

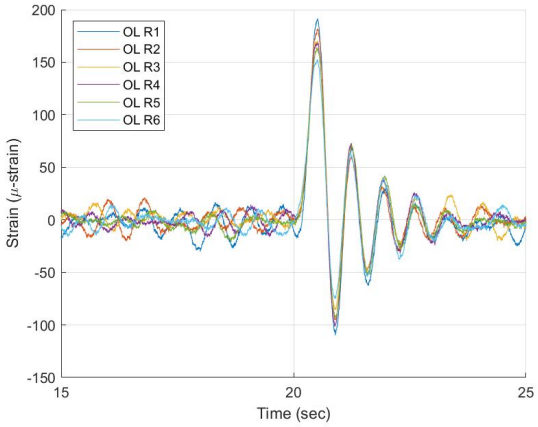

(b) Experiment

Figure 5.4: Time history of wing-root strain excited by 4° Gust at 1.4Hz excitation

the output filter, described in Section 5.1, is applied at the output of the system before Kalman filter. The output filters were not incorporated into the plant as part of controller synthesis, so that the order of the plant was 6 states. The LQR weights are static in both states and control inputs shown below.

$$Q = \begin{bmatrix} 1 & 0 & 0 & 0 & 0 & 0 \\ 0 & 1 & 0 & 0 & 0 & 0 \\ 0 & 0 & 1.04 & 0 & 0 & 0 \\ 0 & 0 & 0 & 2.45 & 1 & 0 \\ 0 & 0 & 0 & 0 & 0 & 0.999 \end{bmatrix}, \qquad R = \begin{bmatrix} 0 & 0 & 0 \\ 0 & 0.01 & 0 \\ 0 & 0 & 0.51 \end{bmatrix} \tag{5.1}$$

The H_2 results of LQR weightings are presented in Figures 5.5, 5.6, and 5.7, and the H_∞ results of LQR weightings are presented in Figures 5.8, 5.9, and 5.10.

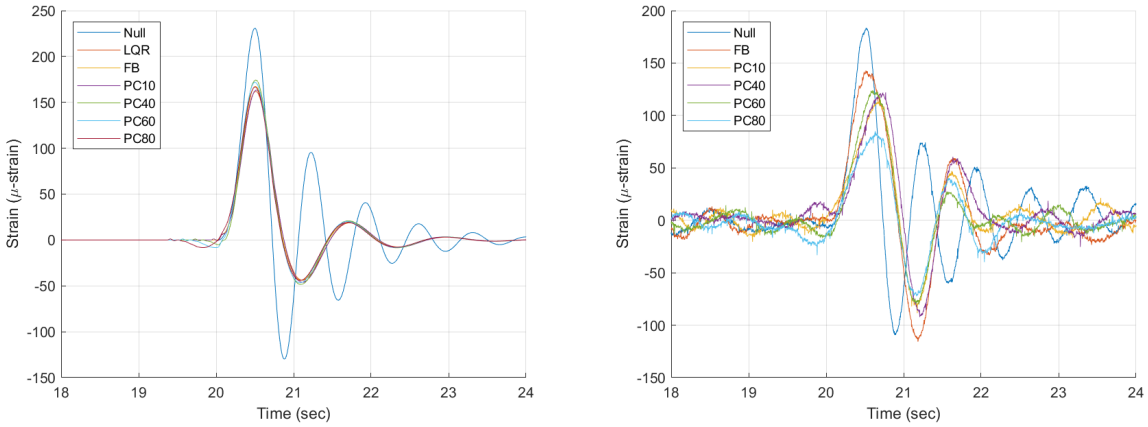

(a) Simulation (b) Experiment

Figure 5.5: Time history of H_2 closed-loop wing-root strain response to gust excitation

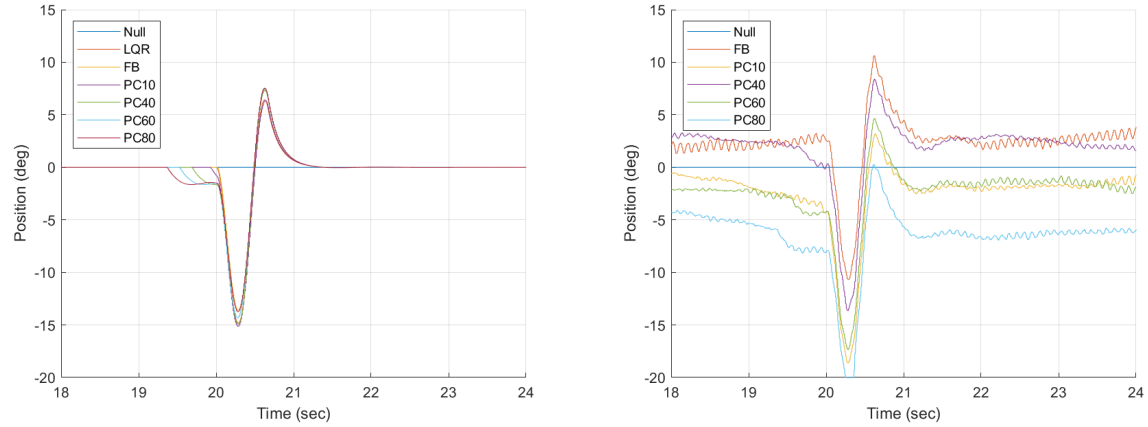

(a) Simulation (b) Experiment

Figure 5.6: Time history of H_2 closed-loop outboard aileron deflection to gust excitation

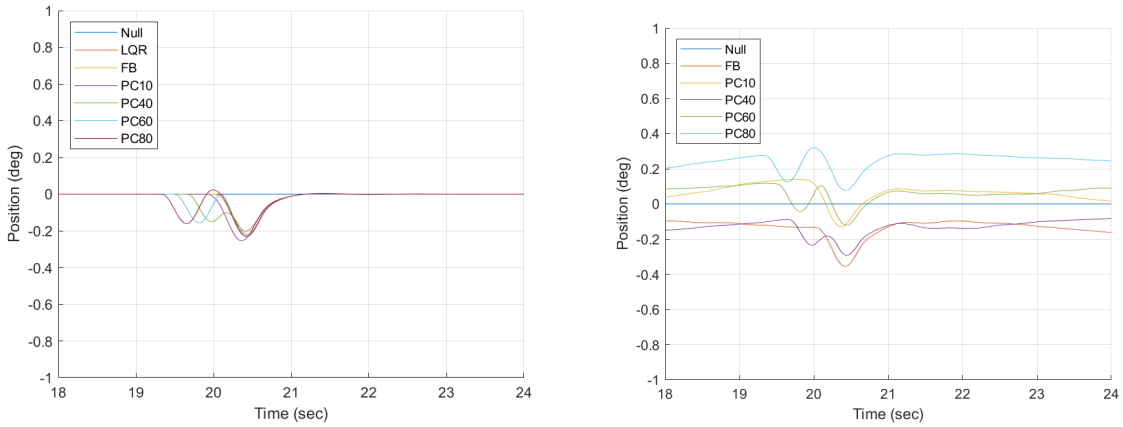

(a) Simulation (b) Experiment

Figure 5.7: Time history of H_2 closed-loop inboard aileron deflection to gust excitation

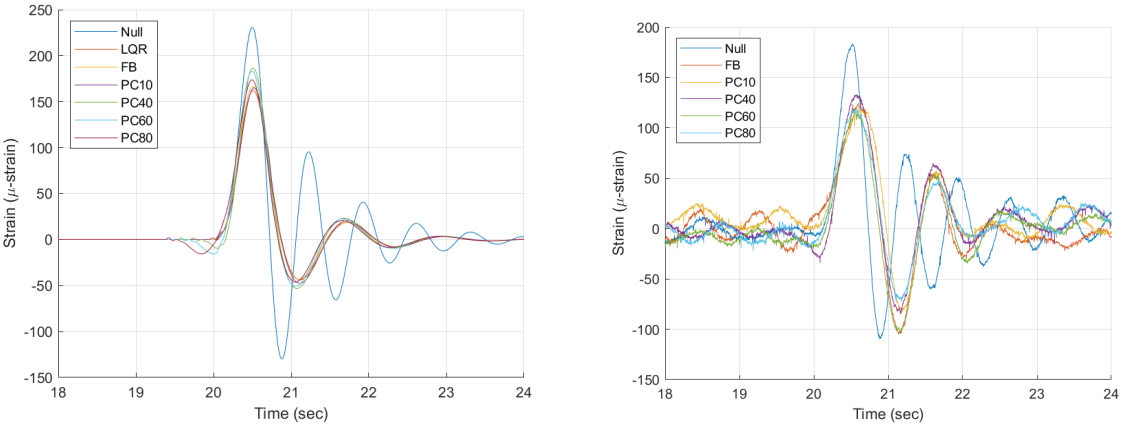

(a) Simulation (b) Experiment

Figure 5.8: Time history of H_∞ closed-loop wing-root strain response to gust excitation

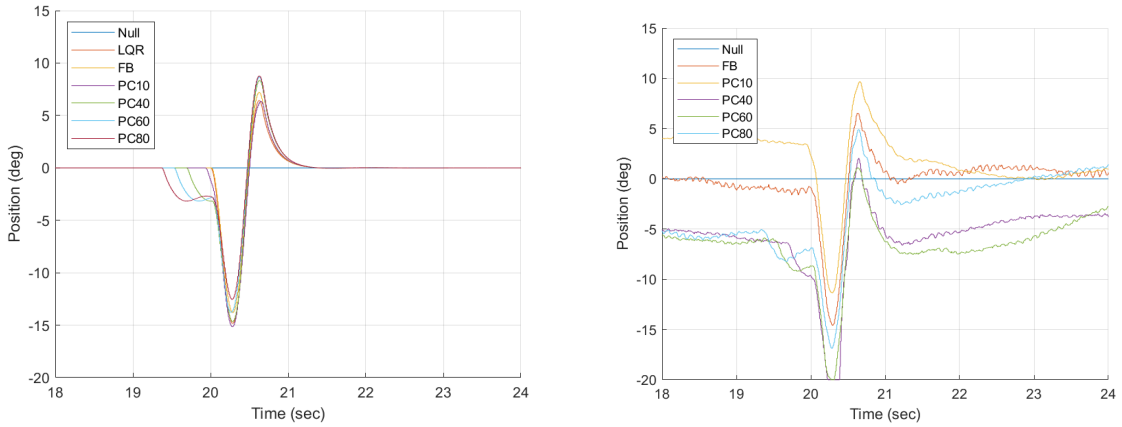

(a) Simulation (b) Experiment

Figure 5.9: Time history of H_∞ closed-loop outboard aileron deflection to gust excitation

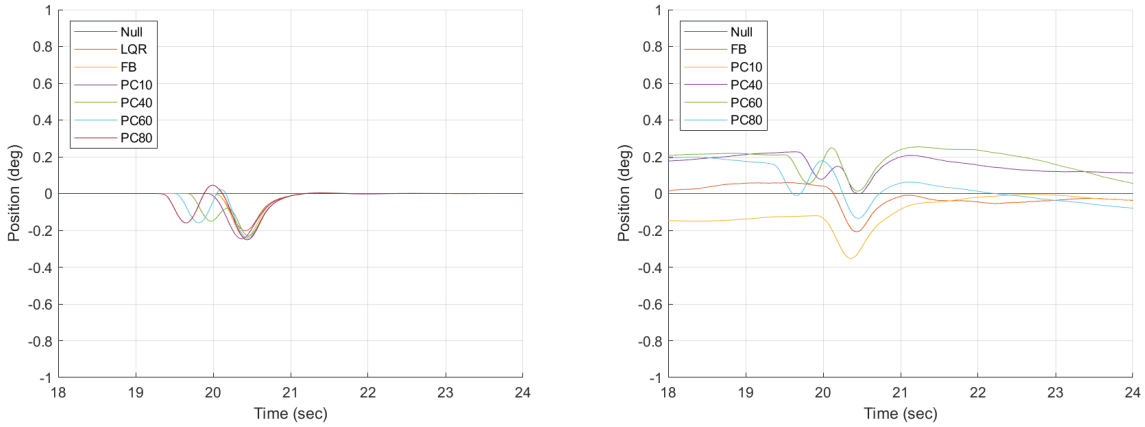

(a) Simulation (b) Experiment

Figure 5.10: Time history of H_∞ closed-loop inboard aileron deflection to gust excitation

5.3 Output Feedback: Static Weight for Wing-root Strain and Frequency Weight for Ailerons

The present results in this section followed the design steps in Chapter 4 using the 2019 model. The closed-loop system is output feedback with output filters excluding the Kalman filter. The selected regulated channels were the wing-root strain, inboard, and outboard ailerons motions for gust load alleviation while minimizing control inputs. The elevator was used for trim flight such that it was excluded. A static weight approach was selected as suggested in [23]. The static weight was tuned such that the norms decreased monotonically with respect to preview steps. Outboard and inboard ailerons used the same frequency weight to penalize high-frequency actuation due to bandwidth limitation of the actuators. The output filters were not incorporated into the plant, so that the order of the plant was 6 states. The frequency weights increased the number of states to 6+2, two 1st-order frequency weights, and the augmented preview plants were $6 + 2 + h$ states with respect to h preview steps. The full-order controllers were synthesized so that the controller had the same state order as the augmented preview plant's state order. The weights are tabulated in Table 5.2 and shown in Figure 5.11.

Table 5.2: Static weight for wing-root strain and frequency weight for ailerons

Regulated Channels	Weighting Type	Order	dcgain	Frequency (Hz), Gain (mag)
Wing-root Strain	Static	N/A	1.1765	N/A
Outboard Aileron	High-pass	1st	1	5, 2
Inboard Aileron	High-pass	1st	1	5, 2

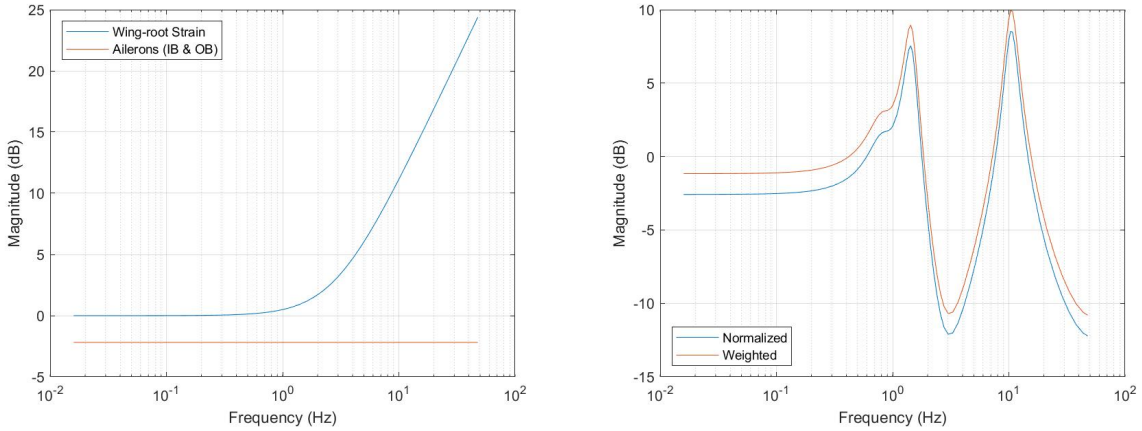

(a) Weighting (b) Weighted wing-root strain

Figure 5.11: Bode magnitude plot of weighting and weighted wing-root strain

5.3.1 Norms Plots

Figures 5.12 and 5.13 displays the norms versus preview steps and controller synthesis time. In the figures, the *Full* stands for full-order controller as described in Table 2.1.

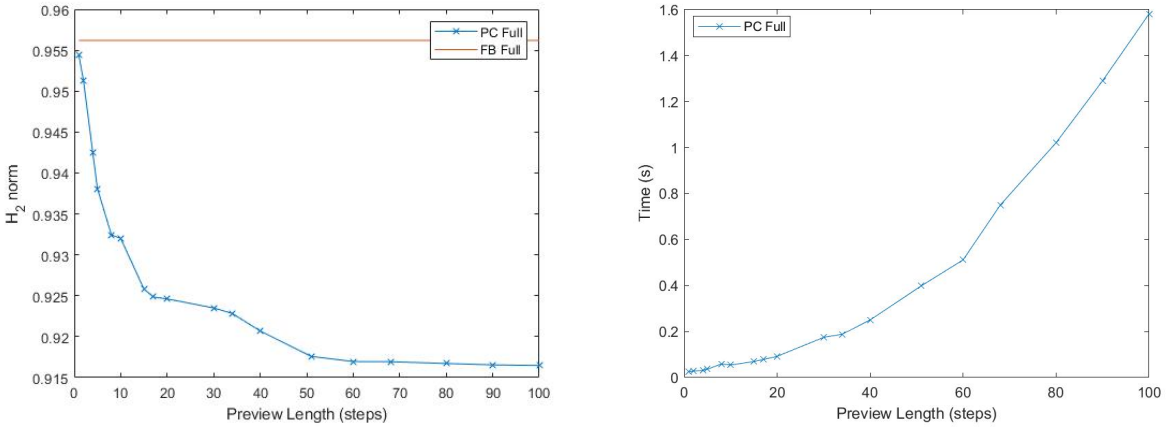

(a) Norms vs Preview Steps (b) Synthesis Time vs Preview Steps

Figure 5.12: H_2 synthesis with sample time of 0.01s

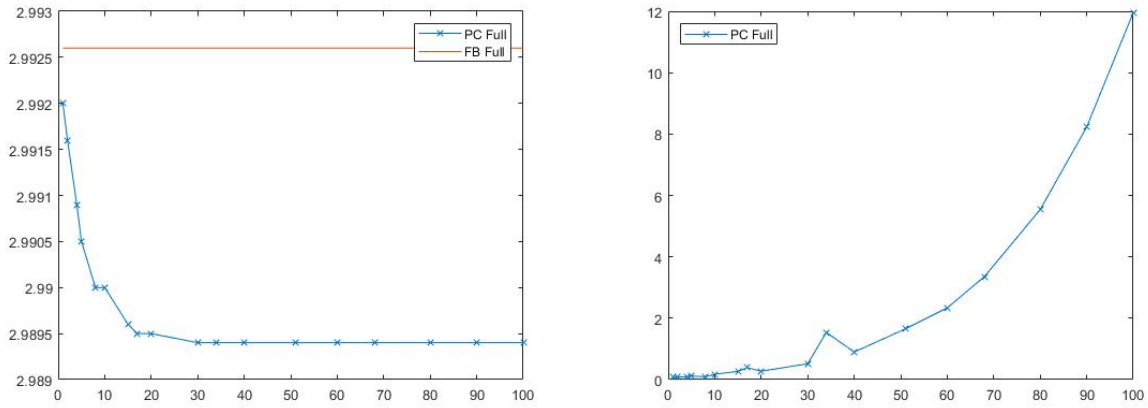

(a) Norms vs Preview Steps (b) Synthesis Time vs Preview Steps

Figure 5.13: H_∞ synthesis with sample time of 0.01s

5.3.2 Closed-loop

The H_2 and H_∞ closed-loop frequency response of wing-root strain, inboard, and outboard aileron, are shown in Figures 5.14, 5.15, and 5.16.

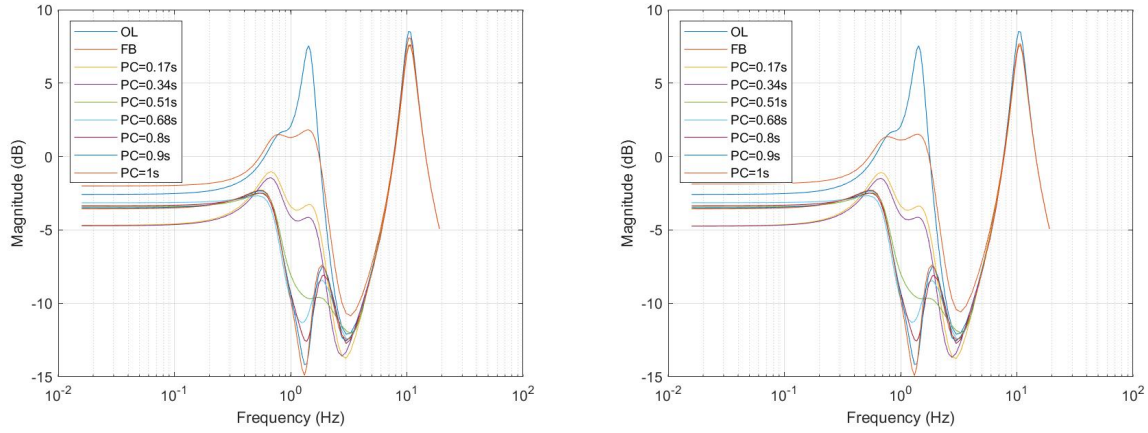

(a) H_2 (b) H_∞

Figure 5.14: Bode plot of normalized wing-root strain response to normalized gust excitation

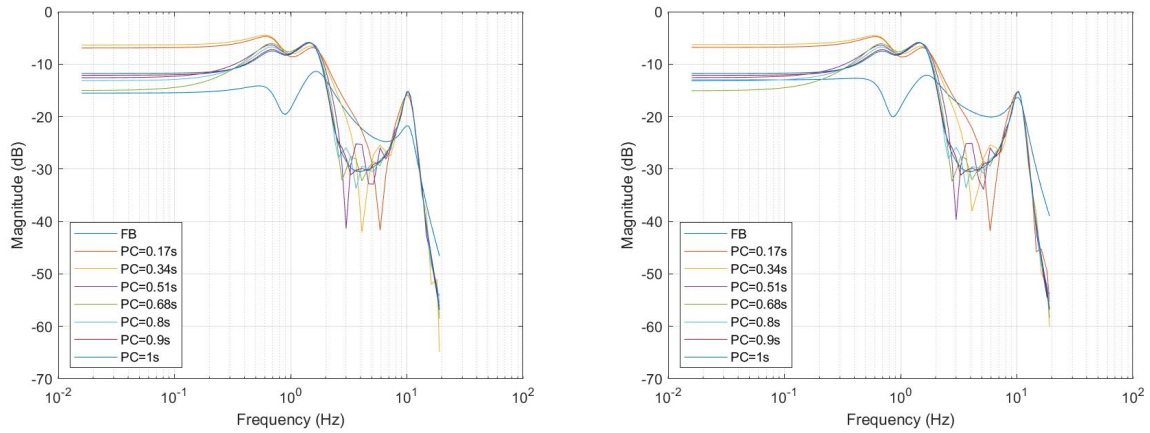

(a) H_2 (b) H_∞

Figure 5.15: Bode plot of normalized outboard aileron response to normalized gust excitation

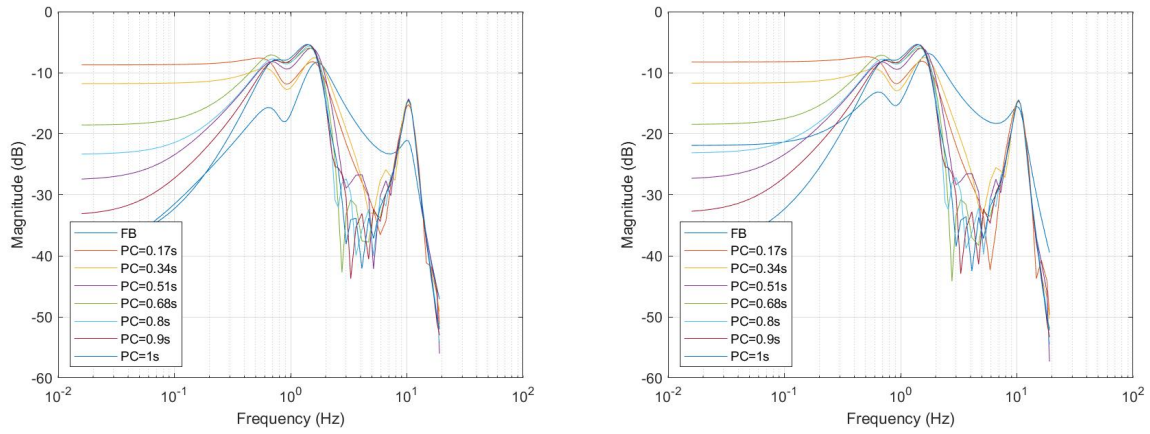

(a) H_2 (b) H_∞

Figure 5.16: Bode plot of normalized inboard aileron response to normalized gust excitation

5.3.3 Simulation and Experimental Results

The H_2 closed-loop time responses are shown in Figures 5.17, 5.18, and 5.19, and H_∞ closed-loop time responses are shown in Figures 5.20, 5.21, and 5.22. The maximum absolute

wing-root strain and aileron deflections are plotted in Figures 5.23, 5.24, and 5.25 with respect to preview time.

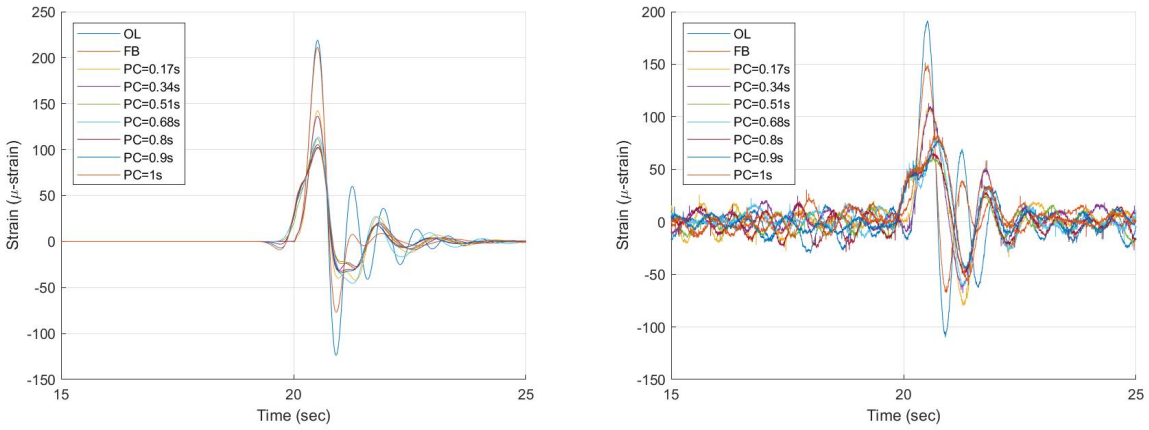

(a) Simulation (b) Experiment

Figure 5.17: Time history of H_2 closed-loop wing-root strain response to gust excitation

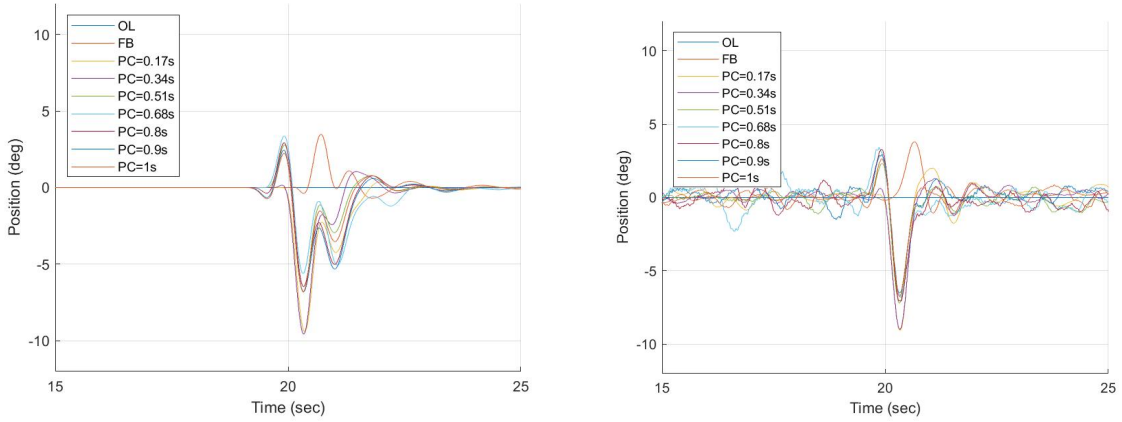

(a) Simulation (b) Experiment

Figure 5.18: Time history of H_2 closed-loop outboard aileron deflection to gust excitation

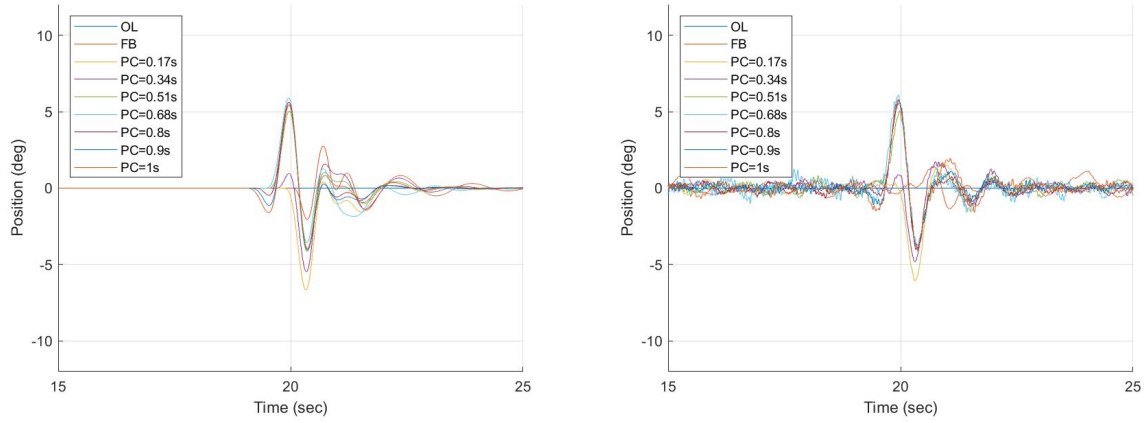

(a) Simulation (b) Experiment

Figure 5.19: Time history of H_2 closed-loop inboard aileron deflection to gust excitation

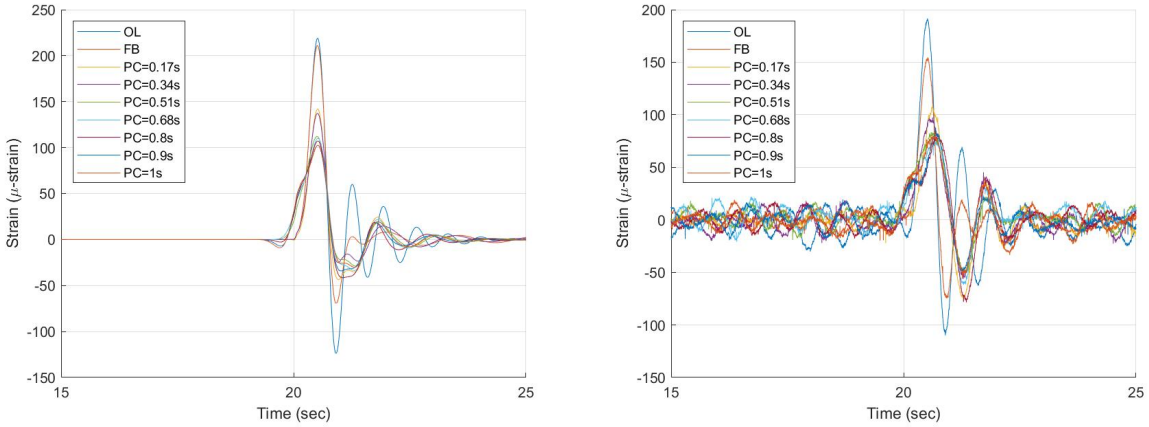

(a) Simulation (b) Experiment

Figure 5.20: Time history of H_∞ closed-loop wing-root strain response to gust excitation

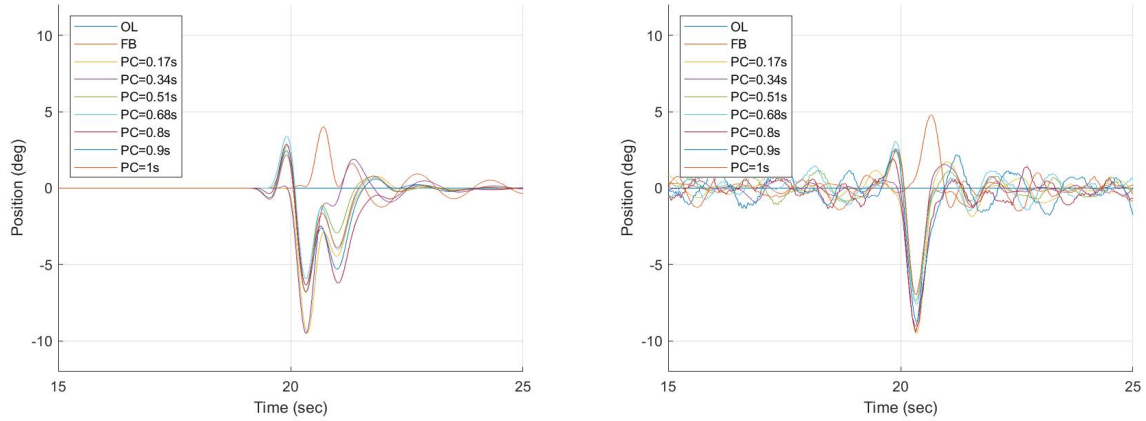

(a) Simulation (b) Experiment

Figure 5.21: Time history of H_∞ closed-loop outboard aileron deflection to gust excitation

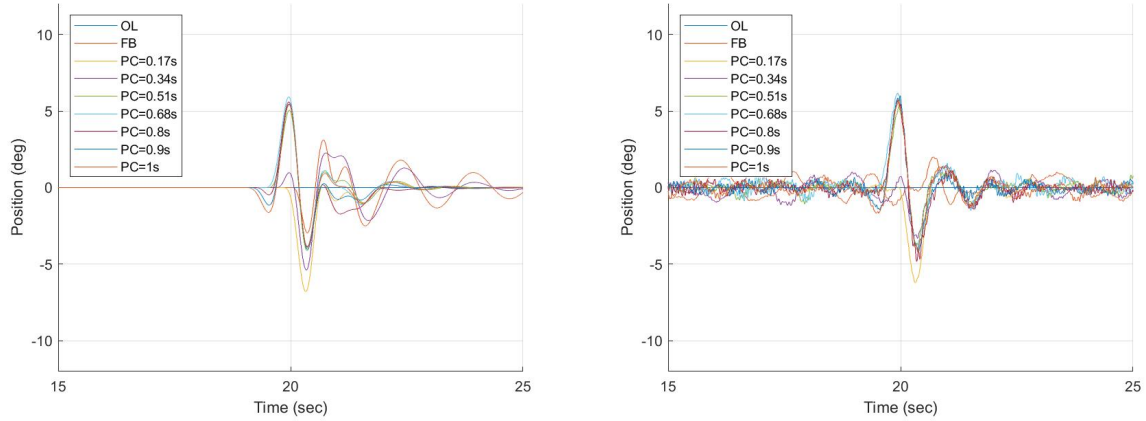

(a) Simulation (b) Experiment

Figure 5.22: Time history of H_∞ closed-loop inboard aileron deflection to gust excitation

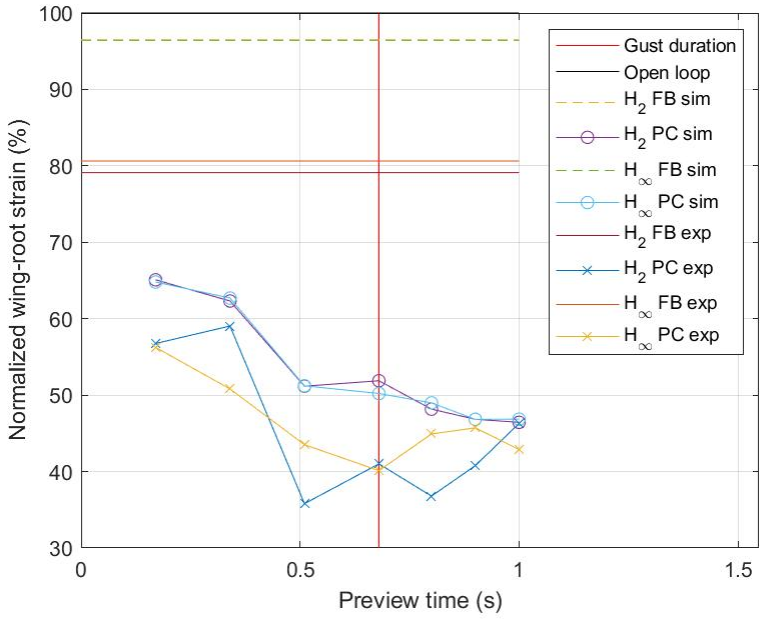

Figure 5.23: Maximum absolute normalized wing-root strain vs. preview time

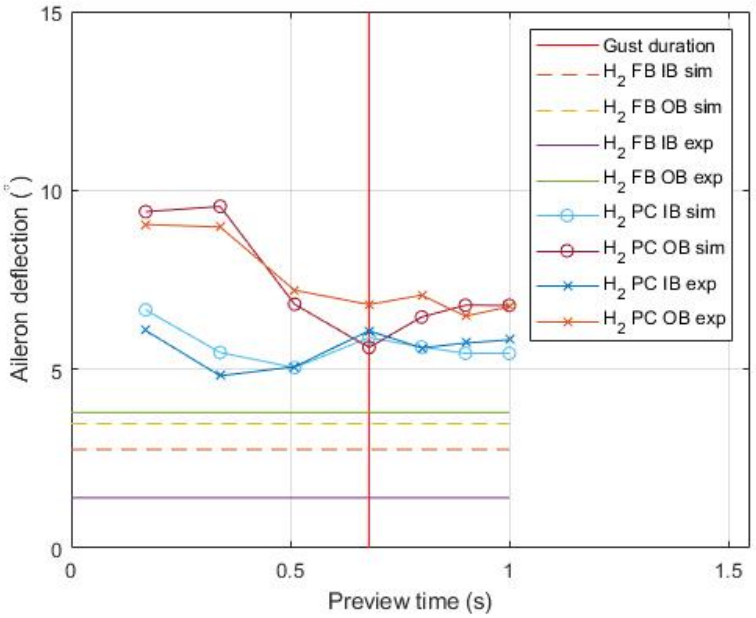

Figure 5.24: Maximum absolute inboard aileron deflection vs. preview time

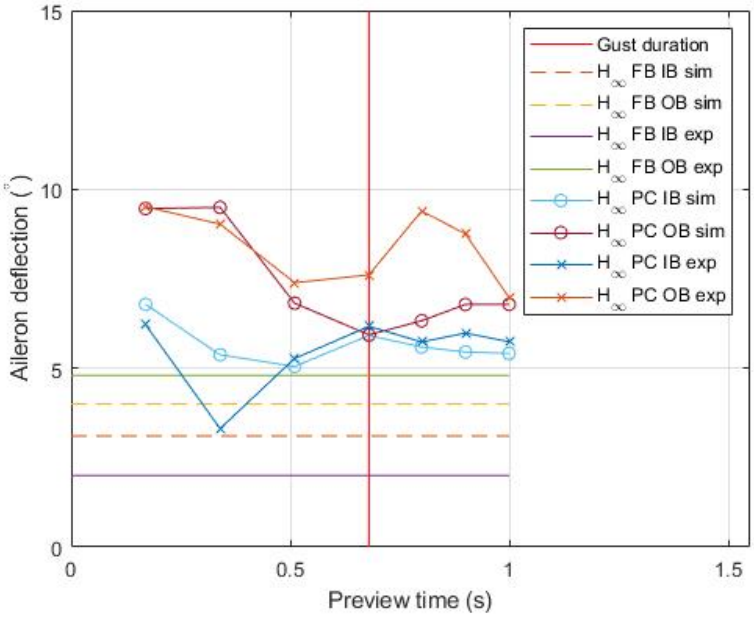

Figure 5.25: Maximum absolute outboard aileron deflection vs. preview time

5.4 Output Feedback: Frequency Weight for Wing-root Strain and Ailerons

The present results have same set up as Section 5.3 except a frequency weight for wing-root strain and incorporation of output filters in controller synthesis. The frequency weight was tuned such that the norms decreased monotonically with respect to preview steps. Outboard and inboard ailerons used the same frequency weight to penalize high-frequency actuation due to bandwidth limitation of the actuators. The output filters were incorporated into the plant, so that the order of the plant was increased from 6 to 22 states, two 3-order band-pass Butterworth filters, and two 2nd-order low-pass Butterworth filters. The frequency weights increased the number of states to $22 + 3$, three 1st-order frequency weights, and the augmented preview plants were $25 + h$ states with respect to h preview steps. The full-order controllers were synthesized so that the controller had the same state order as the augmented preview plant's state order. The reduced-order results are also presented in this section. In

the following figures, the numbers follow by FB and PC are order of the controllers described in Table 2.1. The frequency weights are tabulated in Table 5.2 and shown in Figure 5.11.

Table 5.3: Frequency weight for wing-root strain and ailerons

Regulated Channels	Weighting Type	Order	dcgain	Frequency (Hz), Gain (mag)
Wing-root Strain	Low-pass	1st	0.7770	2.5, 0.7079
Outboard Aileron	High-pass	1st	1	5, 1.4125
Inboard Aileron	High-pass	1st	1	5, 1.4125

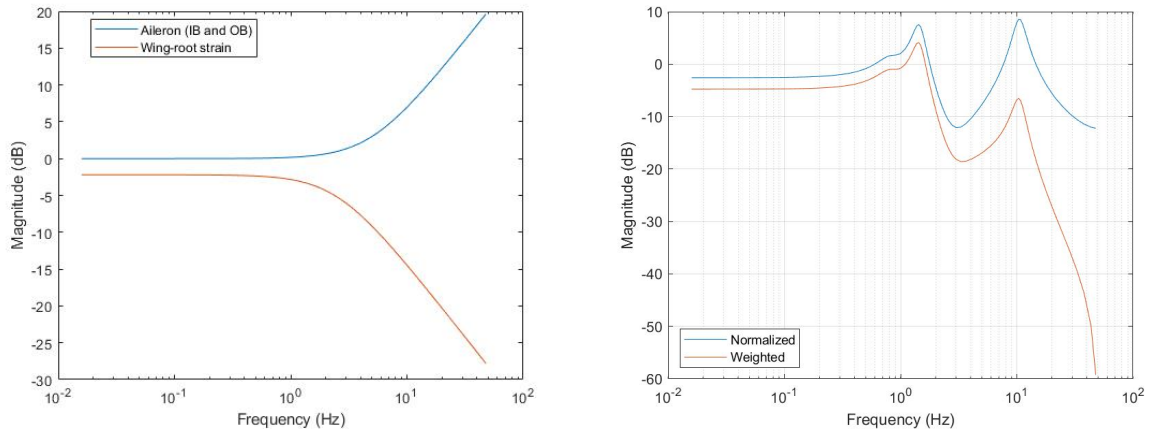

(a) Weighting

(b) Weighted wing-root strain

Figure 5.26: Bode magnitude plot of weighting and weighted wing-root strain

5.4.1 Norms Plots

Figures 5.27 and 5.28 displays the norms versus preview steps and controller synthesis time.

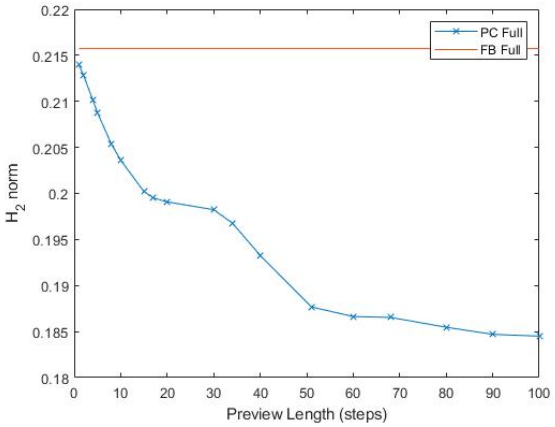

(a) Norms vs Preview Steps

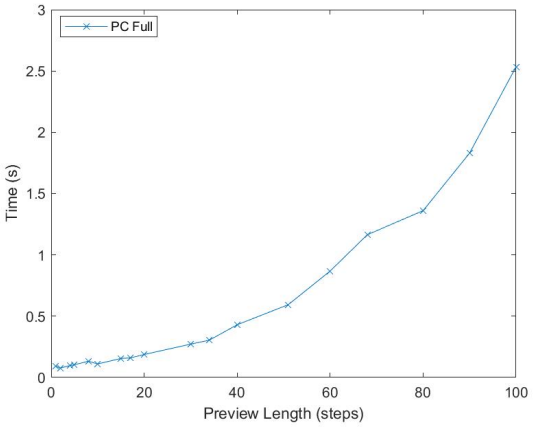

(b) Synthesis Time vs Preview Steps

Figure 5.27: H_2 synthesis with sample time of 0.01s

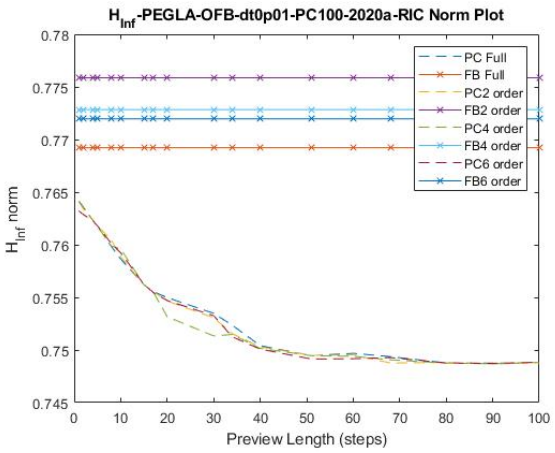

(a) Norms vs Preview Steps

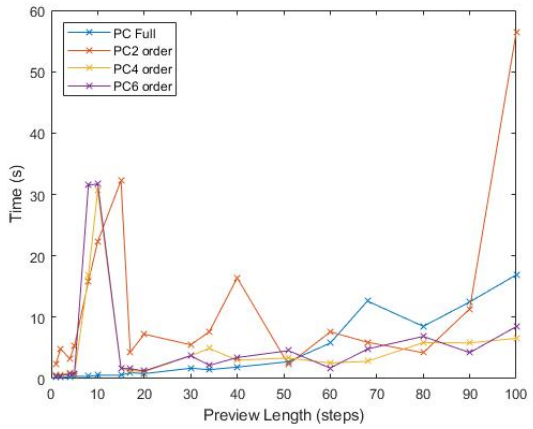

(b) Synthesis Time vs Preview Steps

Figure 5.28: H_∞ synthesis with sample time of 0.01s

5.4.2 Closed-loop

The H_2 and H_∞ closed-loop frequency response are in Figures 5.29, 5.30, and 5.31; furthermore, the fixed-order H_∞ controllers are in Figure 5.32.

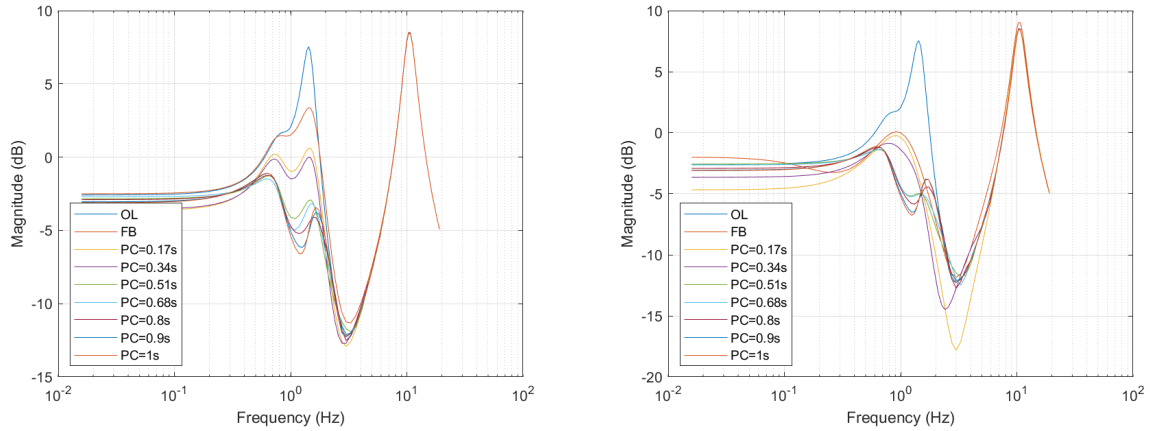

(a) H_2 (b) H_∞

Figure 5.29: Bode plot of normalized wing-root strain response to normalized gust excitation

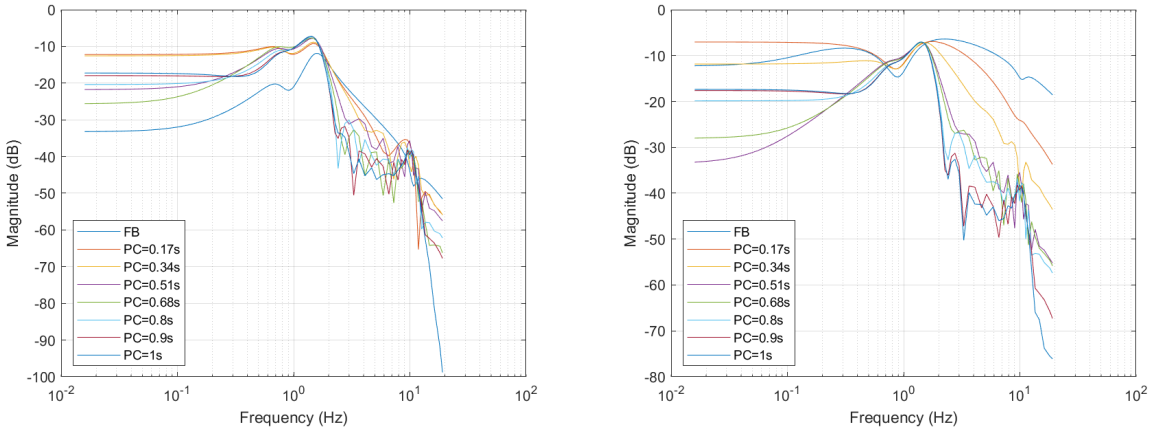

(a) H_2 (b) H_∞

Figure 5.30: Bode plot of normalized outboard aileron response to normalized gust excitation

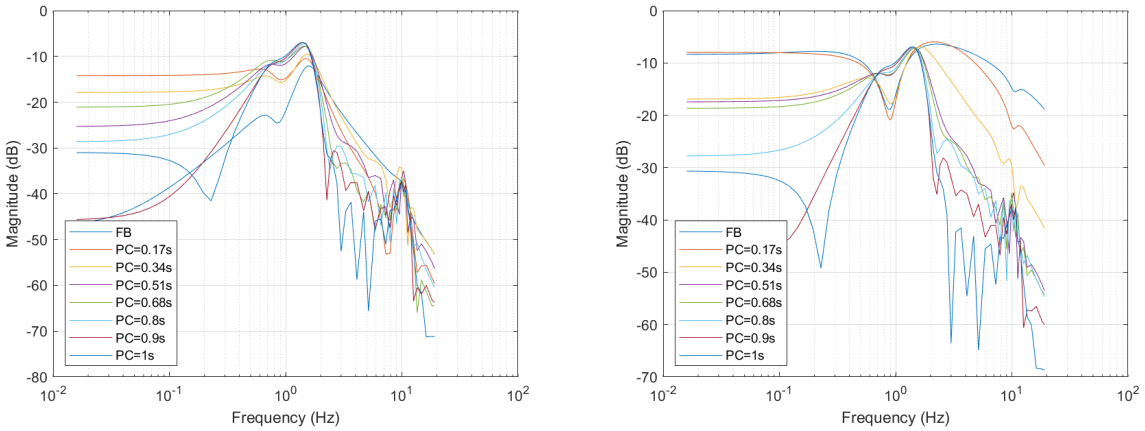

(a) H_2 (b) H_∞

Figure 5.31: Bode plot of normalized inboard aileron response to normalized gust excitation

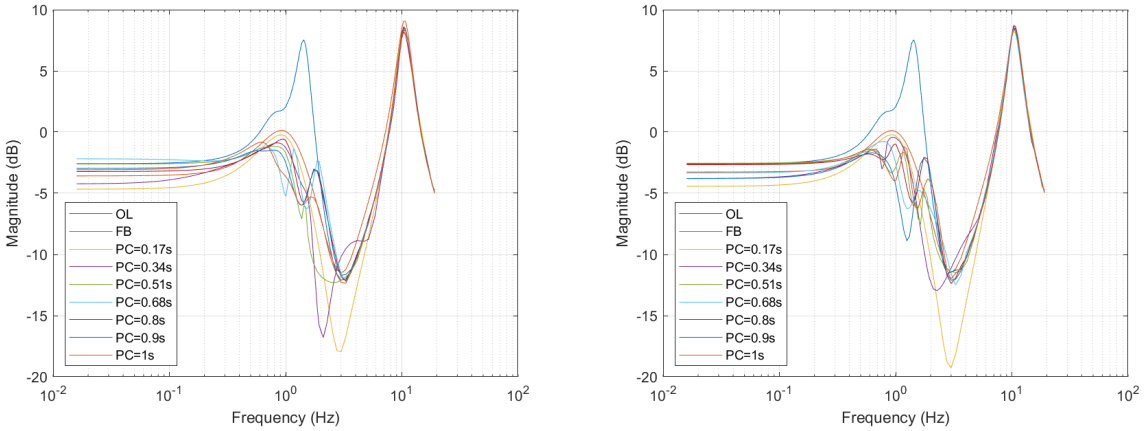

(a) H_∞ 6th-order (b) H_∞ 4th-order

Figure 5.32: Bode plot of normalized wing-root strain response to normalized gust excitation

5.4.3 Simulation and Experiments

The full-order H_2 closed-loop time responses are shown in Figures 5.33 to 5.35, the full-order H_∞ closed-loop time responses are shown in Figures 5.36 to 5.38, and the fixed-order, 6th-order and 4th-order, H_∞ closed-loop time responses are shown in Figures 5.39 to 5.44. The maximum absolute wing-root strain and aileron deflections are plotted in Figures 5.45 to 5.47 with respect to preview time. In Figures 5.45 to 5.47, summary of control performance in normalized load alleviation and maximum absolute aileron deflections are presented, on the y-axis, given preview information, on the x-axis, for variation of full-order H_2, full-order and fixed-order H_∞ in feedback and preview of simulation and experimental with results.

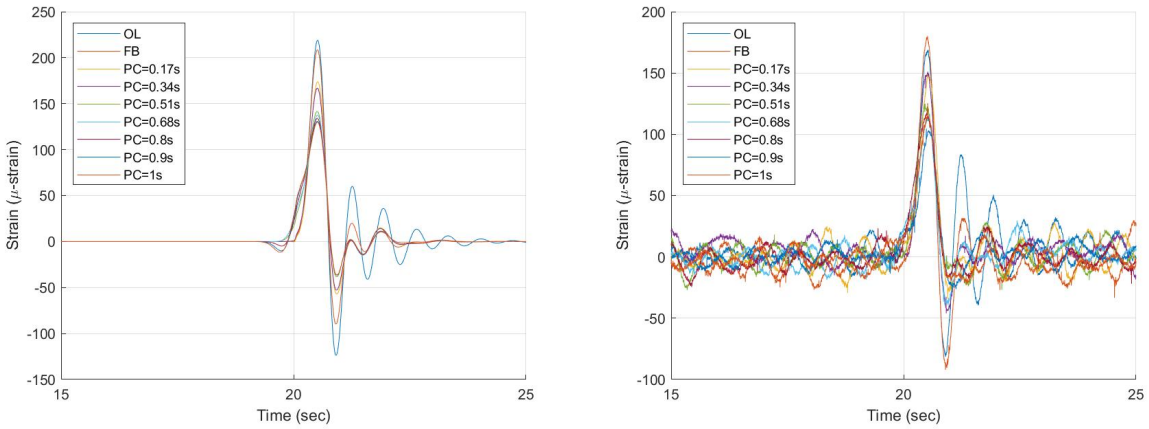

(a) Simulation

(b) Experiment

Figure 5.33: Time history of H_2 closed-loop wing-root strain response to gust excitation

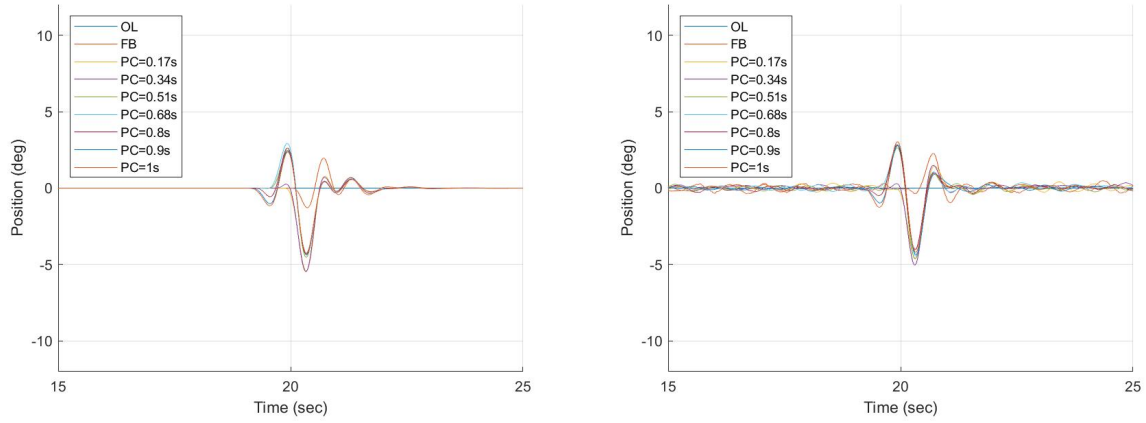

(a) Simulation (b) Experiment

Figure 5.34: Time history of H_2 closed-loop outboard aileron deflection to gust excitation

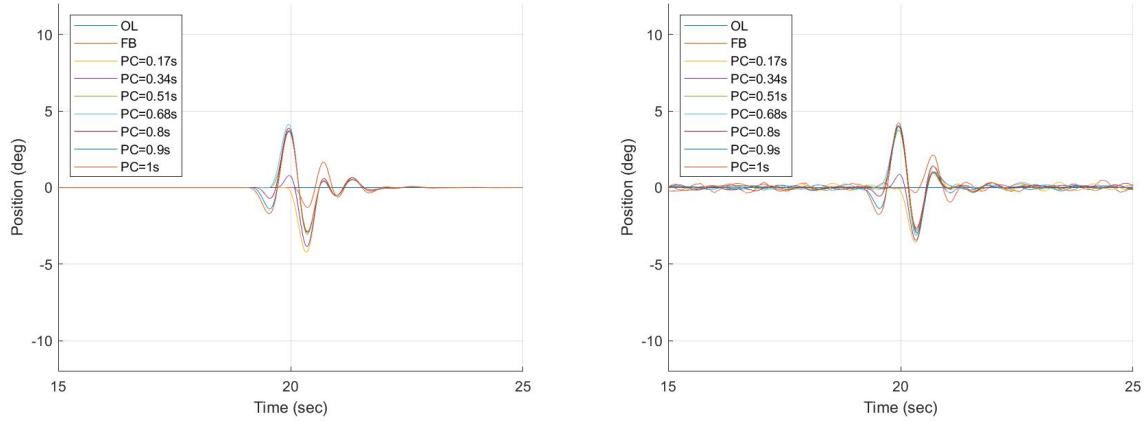

(a) Simulation (b) Experiment

Figure 5.35: Time history of H_2 closed-loop inboard aileron deflection to gust excitation

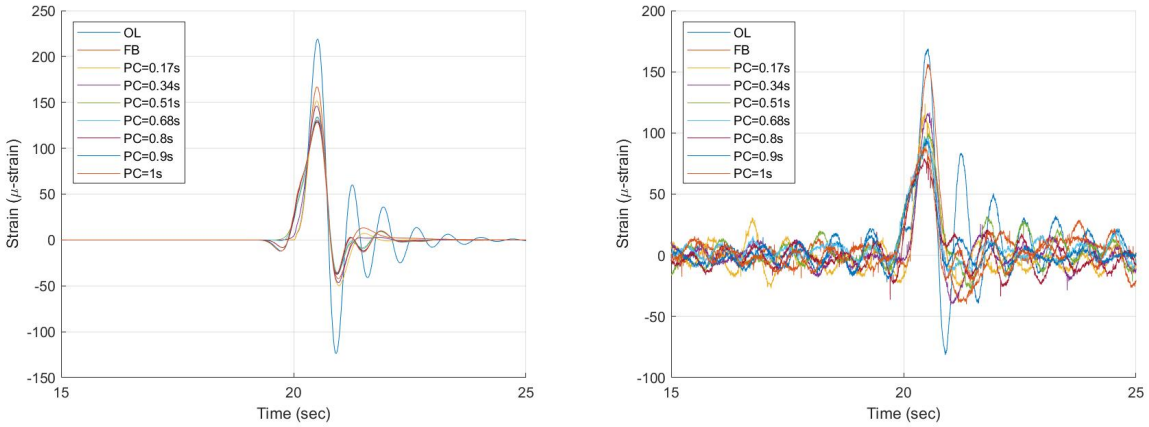

(a) Simulation (b) Experiment

Figure 5.36: Time history of H_∞ closed-loop wing-root strain response to gust excitation

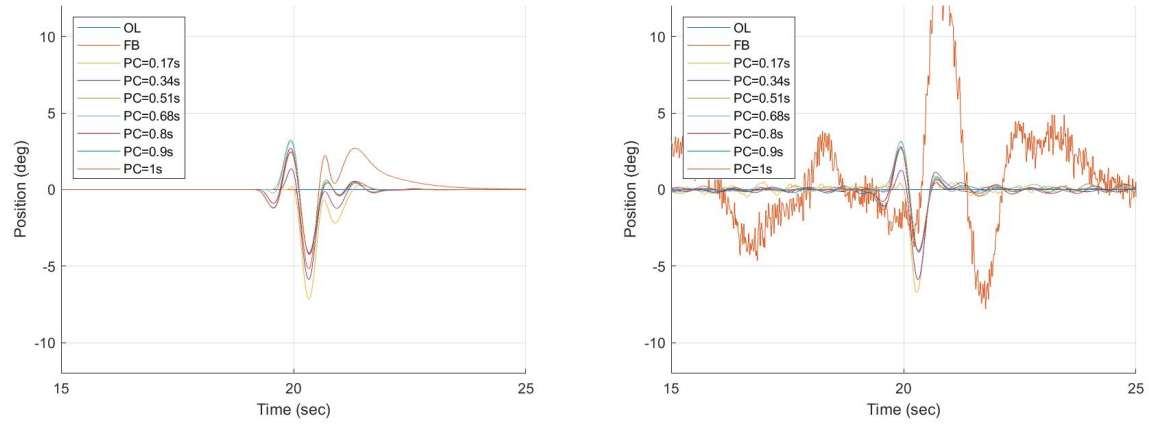

(a) Simulation (b) Experiment

Figure 5.37: Time history of H_∞ closed-loop outboard aileron deflection to gust excitation

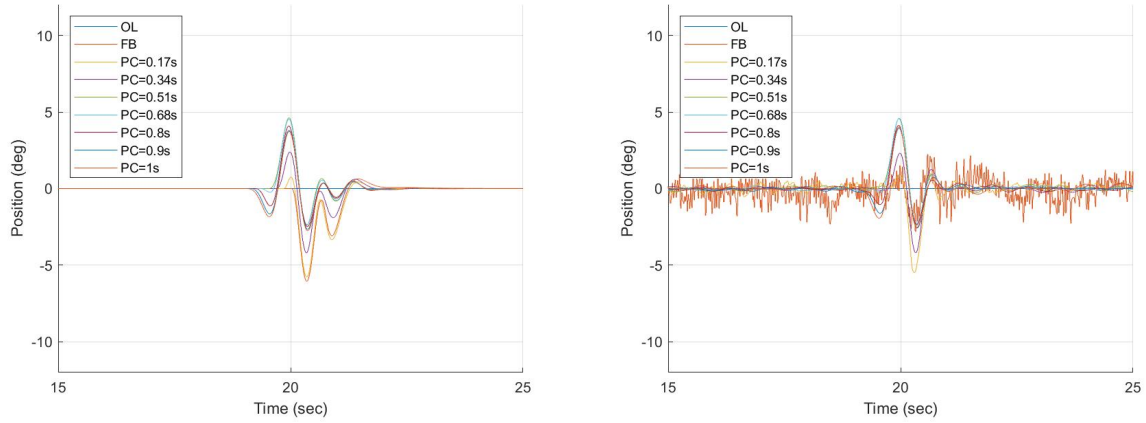

(a) Simulation (b) Experiment

Figure 5.38: Time history of H_∞ closed-loop inboard aileron deflection to gust excitation

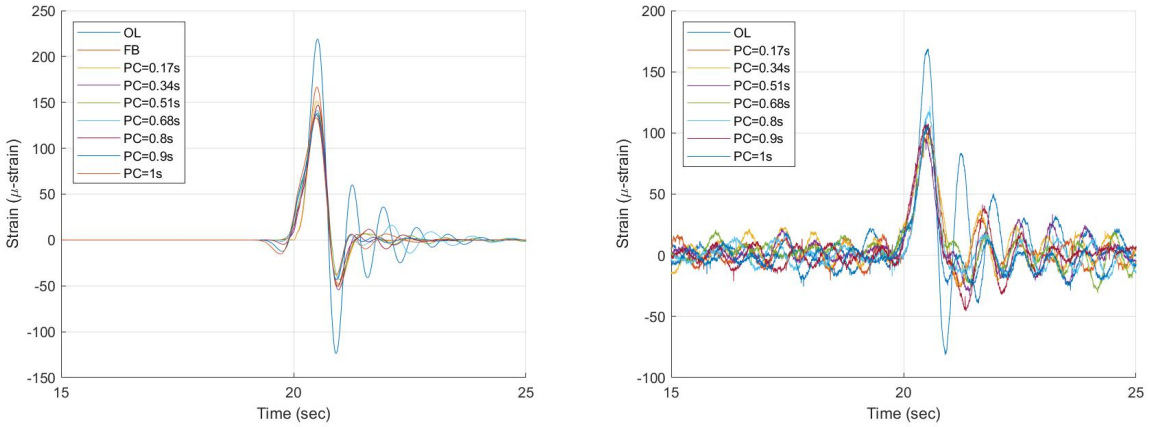

(a) Simulation (b) Experiment

Figure 5.39: Time history of H_∞ 6th-order closed-loop wing-root strain response to gust excitation

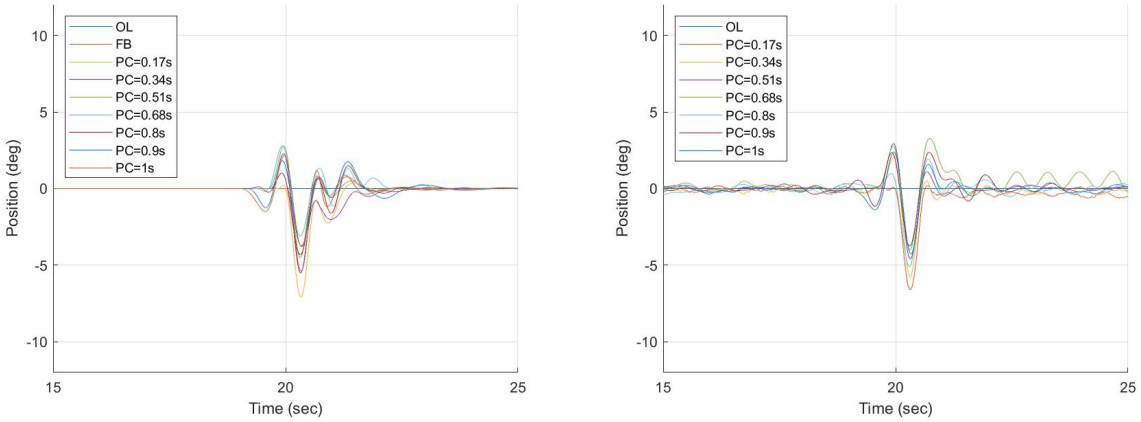

(a) Simulation (b) Experiment

Figure 5.40: Time history of H_∞ 6th-order closed-loop outboard aileron deflection response to gust excitation

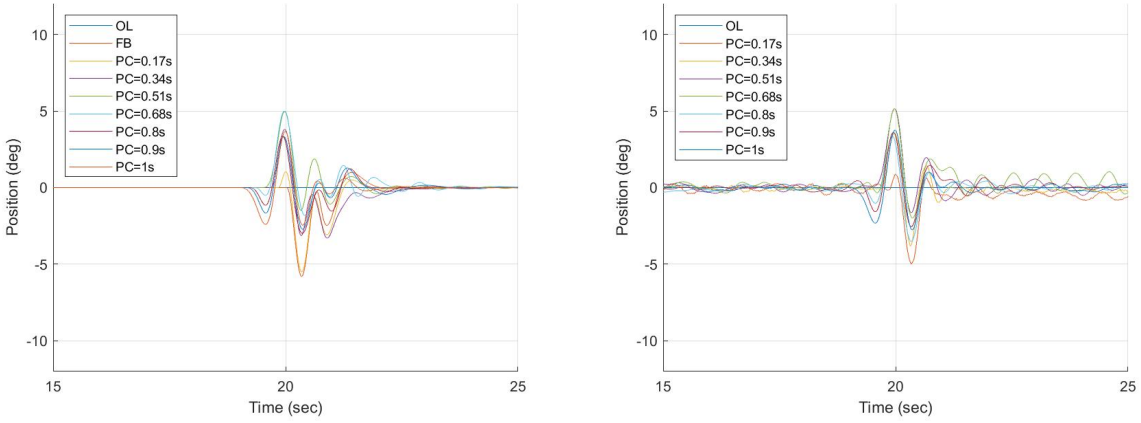

(a) Simulation (b) Experiment

Figure 5.41: Time history of H_∞ 6th-order closed-loop inboard aileron deflection response to gust excitation

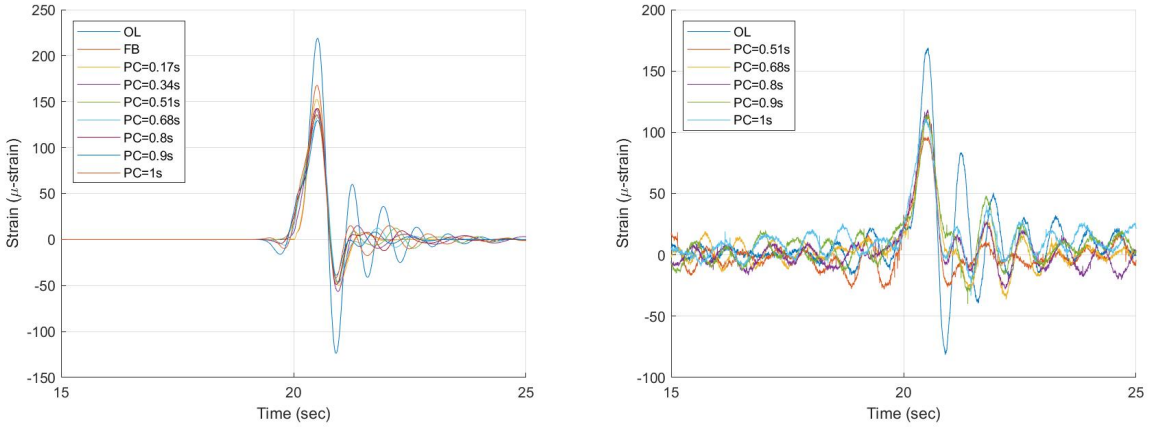

(a) Simulation (b) Experiment

Figure 5.42: Time history of H_∞ 4th-order closed-loop wing-root strain response to gust excitation

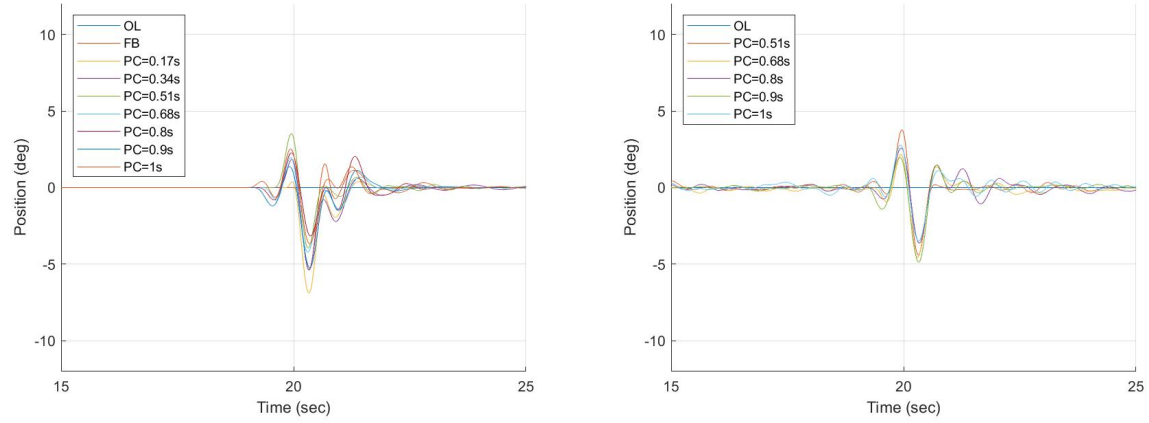

(a) Simulation (b) Experiment

Figure 5.43: Time history of H_∞ 4th-order closed-loop outboard aileron deflection response to gust excitation

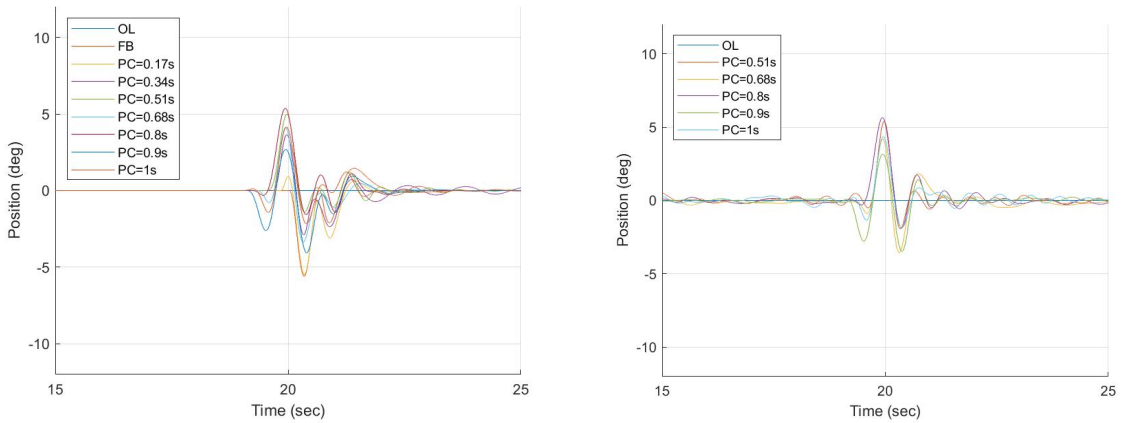

(a) Simulation (b) Experiment

Figure 5.44: Time history of H_∞ 4th-order closed-loop inboard aileron deflection response to gust excitation

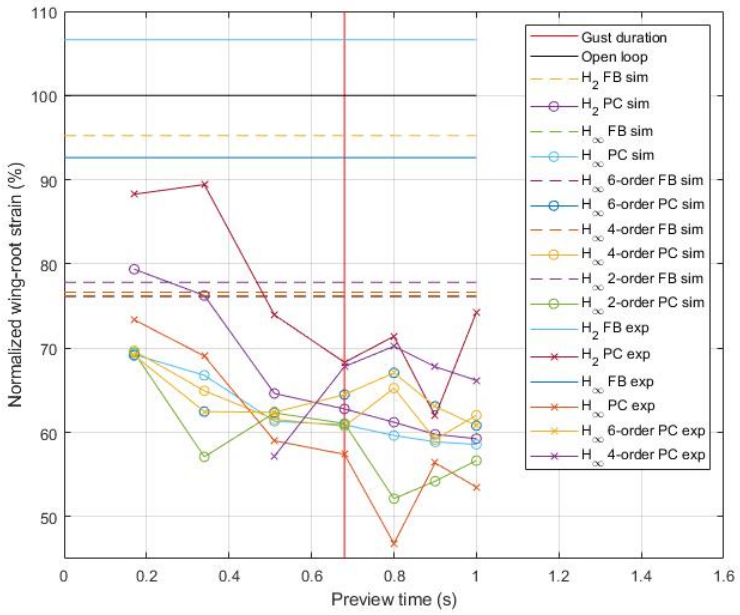

Figure 5.45: Maximum absolute normalized wing-root strain vs. preview time

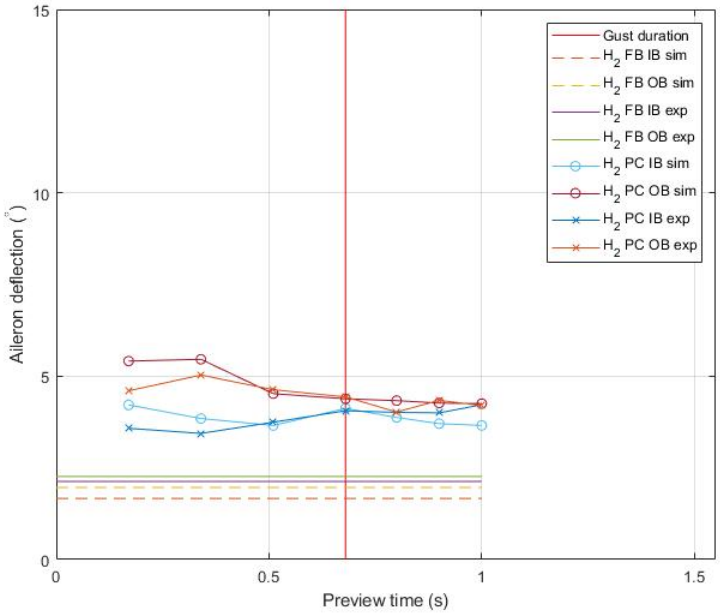

Figure 5.46: H_2 maximum absolute aileron deflection vs. preview time

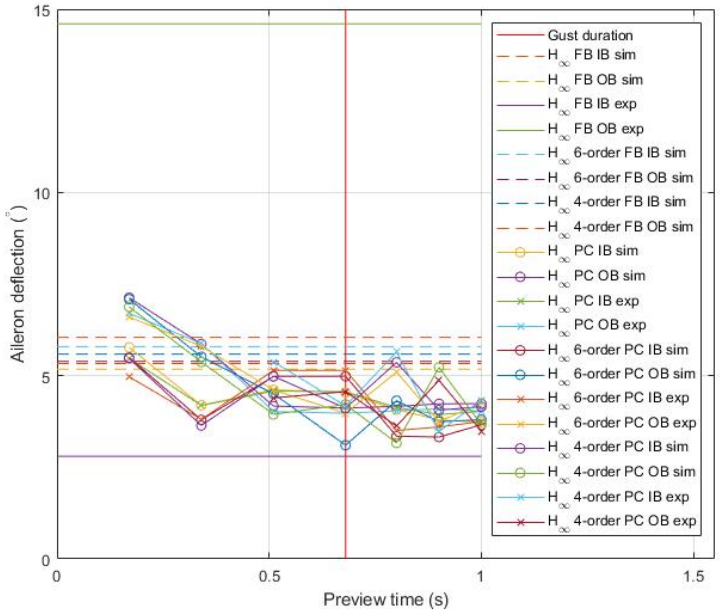

Figure 5.47: H_∞ maximum absolute aileron deflection vs. preview time

5.5 Chapter Summary

Both simulated and experimental results of H_2 and H_∞ control in feedback and preview are presented. LQR weights were tested first to verify the implementation of the H_2 controller. The systematic approach of preview controller design is adopted for efficient weight tune replacing LQR arbitrary weight tune approach. Static weight and frequency weight in wing-root strain were tested. The output filters were included in the plant to increase fidelity of the model. Chapter 6 discusses the results presented in this chapter.

Chapter 6
DISCUSSION

The results of simulation and experiments are presented in Chapter 5. This chapter discusses the detailed comparison between simulation and experiments, $\mathcal{H}_2$ and $\mathcal{H}_\infty$ controllers, feedback and preview, full-order and fixed order. Open-loop and three weighting setups are discussed with results from Chapter 5. The discussion format follows the last chapter from open-loop to each weighting cases.

6.1 Open-loop

The open-loop system has four inputs and four outputs. The inputs include elevator, outboard aileron, inboard aileron, and gust disturbance, while the outputs include forward, afterward accelerometer, wing-root strain, and pitch. The gust disturbance is not an input due to non-controllable but is modeled for gust response and preview control purposes. The elevator was deployed for trim flight such that it was not utilized for gust load alleviation control. The system matrices for the 2018 and 2019 models are in Section 3.5. The goal of gust load alleviation is minimizing the wing-roost strain bending which is equivalent to minimize the response of transfer function shown in Figures 5.2 and 5.3 of upon gust excitation The 2019 model has a low-frequency response lower than the 2018 model. The peak response of the first wing bending mode of the 2019 model is lower than the 2018 model, but the peak response of second wing bending mode of the 2019 model is higher than the 2018 model and higher than the first wing bending mode response. The systems with output filters are included to increase the fidelity of the modeled plant for controller synthesis and shown the filters do not alter or delay the system response .

The output filters are applied at each channel eliminating high-frequency content. The

forward and afterward accelerometers have a band-pass filter preventing low-frequency drift. Table 5.1 tabulated each channels filter type and cut-off frequencies, and Figure 5.1 shows the bode plots of the filters.

Figure 5.4 displays baseline wing root-strain response to gust excitation of 4° deflections of gust vane at 1.4 Hz. The gust profile is selected and targeted the first wing bending mode for the most significant response within the gust generation system bandwidth. All tests in Chapter 5 were tested in the same conditions with 4° deflection of gust vane at 1.4 Hz at $t = 20$s. The simulation has no random noise such that there exists no variation nor uncertainty; however, the experimental results illustrate uncertainty due to random excitation from wind tunnel turbulence.

6.2 LQR Weighting

As stated in Section 5.2, the LQR weights in Equation 5.1 were tuned in prior work [2–4]. The H_2 optimization with the LQG setup, described in Section 2.3.3, was to validate the implementation. The validation work was done in the early stage of research prior to the dynamical system update. The controller synthesis used the 2018 model with full-state feedback setup. The closed-loop system used both of the output filters and Kalman filter; however, the output filters were not included in the plant for controller synthesis. From Equation 5.1, the weights in each state are almost identical except 2.5 times penalty in the derivative of the first wing bending mode to minimize wing-root strain response. The elevator was used for trim flight such that it had no weights, and the inboard aileron was penalized more than the outboard aileron.

Figures 5.5, 5.6, and 5.7 show the time history of H_2 and Figures 5.8, 5.9, and 5.10 show the time history of H_∞. It is evident from Figure 5.5 that the implementation of LQR weights in H_2 control is successful. The time history of H_2 control matched LQR control performance in both simulation and experimental results. The preview has minimal benefits in the simulation, even with full gust length ($> 0.68s$) information. The experimental results confirm the minimal benefits of the preview with steps of 10, 40, and 60 (0.1s, 0.4s, and 0.6s).

The case of 80 preview steps (0.8s preview time) shows significant wing-root strain reduction contradicting simulation work. It is suspected that the turbulence in the wind tunnel induces random excitation causing reduction as mentioned in Section 5.2; however, the work is never repeated due to the interest in the benefits of the preview. Figure 5.8 shows that the preview worsened the wing-root strain compared to the feedback suggesting a new approach for weight selection and tuning. Figures 5.6 and 5.9 demonstrates the early actuation prior to gust excitation from preview information. The inboard aileron is highly penalized comparing to the outboard aileron such that there is minimal control actuation in Figures 5.7 and 5.10. Although the preview information does not benefit wing-root strain reduction with LQR weighting, the results show the ailerons can actuate ahead of gust excitation and potentially pre-load the wing to reduce gust load with well-tuned weight.

6.3 Static Weight for Wing-root Strain and Frequency Weight for Ailerons

The works done in Section 5.2 led to a systematic approach for preview weight tune. Section 5.3 work was done after the dynamical system update. The closed-loop system was output feedback setup using the 2019 model with output filters. Unlike the state feedback setup, the Kalman filter was excluded in output feedback. The controller design followed the approach detailed in Chapter 4. The regulated channels were chosen for gust load alleviation while minimizing control inputs. The weights and bode plot of the weights are shown in Table 5.2 and Figure 5.11. The frequency weights increased the states to $6+2$, two 1st-order frequency weights, and the augmented preview plants were $8+h$ states with respect to h preview steps. The resulted full-order controllers had the same state order as the augmented preview plant's state order using either RIC or LMI method.

Figures 5.12 and 5.13 show the norm plots and synthesis time plots. The norm plots suggest a monotonically decrease in norms with respect to preview steps as suggested in [23, 33]. On the other hand, the synthesis time increased exponentially with respect to preview steps. Both H_2 and H_∞ synthesis solved the Ricatti equations, convex, using the MATLAB Robust Toolbox [42]. H_2 required less computation time than H_∞. Although

fixed-order controllers were synthesized, the norms and closed-loop performance were not desired such that they were not tested experimentally.

Figures 5.14, 5.15, and 5.16 display the normalized closed-loop response of disturbance to wing-root strain, outboard, and inboard ailerons. Both figures show that the preview benefited from minimizing the first wing bending wing-root strain. The maximum absolute responses decrease with respect to preview steps given 4° gust at 1.4 Hz. The frequency weights of ailerons penalized the high-frequency actuation such that the second wing bending mode was hardly suppressed. Although it seems like H_2 and H_∞ have identical wing-root strain responses, the aileron frequency responses show the subtle differences in the normalized frequency response. The H_2 minimized the energy of the system, and the H_∞ minimized the peak response. In feedback setup, Figure 5.14 illustrates that the H_∞ immediately suppressed the second wing bending mode in feedback but penalized by the frequency weights while the H_2 gradually increased actuation to suppress second wing bending mode. The H_∞ norm is measured at the peak response of the system such that the H_∞ norm of the normalized closed-loop is measured at the second wing bending mode. Figure 5.13 presents the norm reduction at second wing bending mode penalized by high-frequency weights. Figures 5.15 and 5.16 confirm the actuations are constrained under 0dB, which is magnitude of 1 normalized by maximal deflection of 20°. Although the frequency weights penalized the high-frequency actuation of ailerons, the normalized frequency response indicates that the inboard and outboard ailerons are still responsive to second wing bending mode excitation at -18dB which is equivalent to 2° aileron deflection.

In the time history, the wing-root strain is minimized with respect to preview length. Both Figures 5.17 and 5.20 demonstrate that the experimental results confirmed the simulation works that the preview benefits wing-root strain reduction. The feedback of both H_2 and H_∞ reduced wing-root strain exceeding expectation. In both H_2 and H_∞ actuation time history, Figures 5.18, 5.19, 5.21, and 5.22 display minor differences between experimental and simulation results. The differences are most likely resulted from the turbulence within wind tunnel. Figures 5.23, 5.24, and 5.25 summarize the maximum absolute value of the

close-loop response in time history with respect to preview times and confirm the benefits of the preview information. Figure 5.23 suggests experimental results at most 10% decrease in reduction comparing to simulation. Figures 5.24 and 5.25 confirm that the actuations are bounded.

6.4 Frequency Weight for Wing-root Strain and Ailerons

The work in Section 5.4 was a continuation of Section 5.3. The goal was to improve and parametrize the closed-loop and actuation bandwidth. The work in Section 5.4 had the same output feedback setup using the 2019 model and output filters as Section 5.3. The additional works included are the frequency weight in wing-root strain, including output filters, and fixed-order controller synthesis. The low-pass frequency weighted wing-root strain rolled off the response before 2.5 Hz eliminating unnecessary second wing bending response outside actuation bandwidth. The roll-off frequency was selected to be half of the aileron bandwidth according to the rule of thumb in [41]. The dc gain of frequency weight was tuned such that the norms decreased monotonically with respect to preview steps. Outboard and inboard ailerons used the same frequency weight to penalize high-frequency actuation due to bandwidth limitation. The output filters were included in controller synthesis that the plant order increased from 6 states to 22 states, two 3rd-order band-pass Butterworth filters, and two 2nd-order low-pass Butterworth filters. The frequency weights increased the states to $22 + 3$, three 1st-order frequency weights, and the augmented preview plants became $25 + h$ states with respect to h preview steps.

Figures 5.27 and 5.28 show the norm plots and synthesis time plots. The norm plots suggest a monotonically decrease in norms with respect to preview steps as previous test results in Section 5.3. The norms of the fixed-order feedback controllers were slightly higher than the full-order controller. The preview norms of the fixed-order controllers shows good correlation with the full-order controllers. The computation time for the fixed-order controller generally requires more time due to non-convex controller synthesis for fixed-order, as shown in [40]. Both full-order and fixed-order synthesis were done with *hinfsyn* and *hinfstruct* command in

Robust Control Toolbox [42].

Figures 5.29, 5.30, and 5.31 display the normalized frequency response of wing-root strain, outboard, and inboard ailerons subject to disturbance. Unlike in Section 5.3, the H_∞ controllers immediately suppress the first wing bending mode due to additional frequency weight to roll off the second wing bending mode response. Figure 5.32 illustrates the same results but with fixed-order controllers. As expected, the H_2 controllers minimize the energy over the frequencies and gradually suppress the first wing bending mode response with respect to preview length. The H_2 actuations roll off beyond 2.5 Hz; however, the H_∞ actuations do not roll off in cases of feedback and 1.7s preview. The longer preview time of H_∞ controllers roll off as H_2 controllers. Both Figures 5.30 and 5.31 confirm the actuation were constrained under $0dB$, whose magnitude is one normalization by maximal deflection of 20°.

In the time history, the wing-root strain is minimized with respect to given preview information. Both Figures 5.17 and 5.20 confirm the preview benefiting wing-root strain reduction in both experiments and simulation. The feedback performances of both H_2 and H_∞ are not expected. Although the H_2 feedback simulation suggests a reduction in wing-root strain comparing to open-loop, the experimental result indicated the contrary. Similarly, the H_∞ feedback simulation promises a significant reduction, but the experiment yielded a minor reduction comparing to open-loop and almost unstable performance. The actuations time history in Figures 5.21 and 5.20 also suggests the feedback case is almost unstable and unbounded, unlike the simulation. This is most likely resulted from plant uncertainty or unmodeled dynamics. Besides feedback, preview performances are aligned between simulation and experiments. The time history of actuation has minor differences between experiments and simulation. Figures 5.45, 5.46, and 5.47 summarize the maximum absolute values in time history with respect to preview times. Figure 5.45 indicates the H_2 feedback suffering 10% increase in wing-root strain comparing to simulation despite the matching actuations in Figures 5.46. Figures 5.45 and 5.47 indicate the H_∞ closed-loop response performance matching closely between experiments and simulation besides the feedback case.

In addition, fixed-order controllers are tested and shown in Section 5.4. The 6th-order

feedback controller, 4th-order feedback, 4th-order preview with 1.7s and 3.4s were unstable in experiments such that the experimental results are excluded. The 6th-order preview experimental results confirm the simulation work in Figure 5.39; however, comparing to Figure 5.36 the 6th-order controllers have minor performance loss. Figure 5.45 suggests 5% difference in wing-root strain and Figure 5.47 indicates actuations aligning closely between simulation and experiments. The 4th-order preview results are limited due to unstable closed-loop response. Beside the case of preview with 5.1s have significant reduction which is more than expected from simulation, the wing-root strain of the preview closed-loop response deteriorate at most 10% comparing with the full-order preview response, still outperform feedback, in Figure 5.45.

6.5 Chapter Summary

This chapter discusses the results from Chapter 5. Most of the simulations and experiments show good correlations. The difference between H_2 and H_∞ control performances are discussed. The H_∞ norm is measured at the peak response and the H_∞ control suppresses the peak response in Section 2.3. Section 5.3 shows the norm is measured at second wing bending mode and suppressing first wing bending mode. Section 5.4 uses an additional low-pass filter to roll-off second wing bending mode such that the norm can be measured at first wing bending mode to be suppressed and utilized for weight tune for preview. The preview control demonstrate the feasibility of the preview information benefiting load reduction. The preview H_2 control suppresses the response gradually, while the H_∞ preview control alleviates peak response immediately. Chapter 7 concludes the present paper and addresses future work directions.

Chapter 7
CONCLUSION

Based on prior developments in wind tunnel architecture, including an aeroservoelastic test article and a gust generation system, initial closed-loop control experiments for gust load alleviation have been conducted.

A systematic approach for the H_2 and H_∞ control law synthesis for aeroservoelastic systems has been presented, with results that include simulation and results of experiments in the 3ft by 3ft wind tunnel of University of Washington. Experience and insights gained include better understanding of weight shaping the closed-loop response and performance for the system studied, demonstrated benefits of preview augmentation in the closed-loop feedback system, and various subtleties of H_2 and H_∞ control. The experimental repeatable test results can be used to validate other simulations and active control studies of GLA technology. The work adds insight regarding the parameters that the designer needs to consider and the difference between H_2 and H_∞ control. Future work will focus on the effect of various aeroservoelastic modeling techniques and mathematical methods for accounting for uncertainty and their effects on control law synthesis and closed loop behavior. Moreover, it is crucial to understand the uncertainty and robustness of the closed-loop system with respect to preview time. Control laws for optimizing other performance measures subject to alternate sets of constraints will be studied; furthermore, it is important to examine improvements in the corresponding estimation algorithms. The ultimate goal of this technology development is the integration of LIDAR in the flight control system in order to reduce dynamic loads and improve ride comfort.

BIBLIOGRAPHY

[1] Quenzer, J. D., Barzgaran, B., Mesbahi, M., and Morgansen, K., "The Generic Wide Body Aircraft Model," *2018 AIAA Guidance, Navigation, and Control Conference*, 2018, p. 0877.

[2] Barzgaran, B., Quenzer, J. D., Zongolowicz, A., Hinson, K. A., Mesbahi, M., Morgansen, K., and Livne, E., "Low-Cost Wind Tunnel Studies of Gust Alleviation Control Techniques," *International Forum on Aeroelasticity and Structural Dynamics*, 2019.

[3] Barzgaran, B., Quenzer, Mesbahi, M., Morgansen, K., and Livne, E., "Real-Time Model Predictive Control for Gust Load Alleviation on an Aeroelastic Wind Tunnel Test Article," *AIAA Scitech 2021 Forum*, 2021, p. 0500.

[4] Quenzer, J. D., Zongolowicz, A., Hinson, K. A., Barzgaran, B., Livne, E., Mesbahi M., and Morgansen K., "Model for Aeroelastic Response to Gust Excitation," *AIAA Scitech 2019 Forum*, 2019, p. 2031.

[5] Phillips, W.H., "Gust Alleviation," *Performance and Analysis of Flight Vehicles, NASA SP-258*, NASA, 1971, pp. 505–553.

[6] Hess, R.A., "Optimal Stochastic Control and Aircraft Gust Alleviation," *Journal of Aircraft*, Vol. 8, No. 4, 1971, pp. 284–286.

[7] Arnold, J. I. and Murphy, F. B., "B-52 Control Configured Vehicles: Flight Test Results," *Advanced Control Technology and Its Potential for Future Transport, NASA TMX-3409 (1976/8)*, 1976, pp. 75–89.

[8] McLean, D. and Prasad, R., "A Structure Load Alleviation Control System for a Large Aircraft," *Transactions of the Institute of Measurement and Control*, Vol. 2, No. 1, 1980, pp. 25–37.

[9] Bendixen, G., O'Connell, R., and Siegert, C., "Digital Active Control System for Load Alleviation for the Lockheed L-1011," *The Aeronautical Journal*, Vol. 85, No. 849, 1981, pp. 430–436.

[10] Regan, C.D., and Jutte, C.V., "Survey of Applications of Active Control Technology for Gust Alleviation and New Challenges for Lighter-weight Aircraft," *NASA TM-2012-216008*, 2012.

[11] Livne, E., "Aircraft Active Flutter Suppression: State of the Art and Technology Maturation Needs," *Journal of Aircraft*, Vol. 55, No. 1, 2018, pp. 410–452.

[12] Livne, E., "Integrated Aeroservoelastic Optimization: Status and Direction," *Journal of Aircraft*, Vol. 36, No. 1, 1999, pp. 122–145.

[13] Botez, R., Boustani, I., Vayani, N., Bigras, P., and Wong, T., "Optimal Control Laws for Gust Alleviation," *Canadian Aeronautics and Space Journal*, Vol. 47, No. 1, 2001, pp. 1–6.

[14] Aouf, N., Boulet, B., and Botez, R., "H_2 and H_∞-Optimal Gust Load Alleviation for a Flexible Aircraft," *Proceedings of 2000 American Control Conference, Chicago*, 2000.

[15] Giesseler, H-G., Kopf, M., Faulwasser, T., Varutti, P., and Findeisen, R., "Model Predictive Control for Gust Load Alleviation," *IFAC Proceedings Volumes*, Vol. 45, No. 17, 2012, pp. 27–32.

[16] Sato, M., "Gust Alleviation Flight Controller using Robust Model Predictive Control," *IFAC Proceedings Volumes*, Vol. 43, No. 15, 2010, pp. 7–12.

[17] Ricci, S., De Gaspari, A., Fonte, F., Riccobene, L., Toffol, F., Mantegazza, P., Karpel, M., Roizner, F., Wiberman, R., Weiss, M., Cooper, J.E., Howcroft, C., Calderon, D., and Adden, S., "Design and Wind Tunnel Test Validation of Gust Load Alleviation Systems," *58th AIAA/ASCE/AHS/ASC Structures, Structural Dynamics, and Materials Conference*, 2017, p. 1818.

[18] Schmitt, N., Rehm, W., Pistner, T., Zeller, P., Diehl, H. and Navé, P., "The AWIATOR Airborne LIDAR Turbulence Sensor," *Aerospace Science and Technology*, Vol. 11, No. 7-8, 2007, pp. 546–552.

[19] Bonin, T., Choukulkar, A., Brewer, W., Sandberg, S., Weickmann, A., Pichugina, Y., Banta, R., Oncley, S., and Wolfe, D., "Evaluation of Turbulence Measurement Techniques from a Single Doppler LIDAR," *Atmospheric Measurement Techniques*, Vol. 10, No. 8, 2017, pp. 3021–3039.

[20] Fezans, N., Schwithal, J., and Fischenberg, D., "In-Flight Remote Sensing and Identification of Gusts, Turbulence, and Wake Vortices using a Doppler LIDAR," *CEAS Aeronautical Journal*, Vol. 8, No. 2, 2017, pp. 313–333.

[21] Fezans, N. and Joos, H., "Combined Feedback and LIDAR-Based Feedforward Active Load Alleviation," *AIAA Atmospheric Flight Mechanics Conference*, 2017, p. 3548.

[22] Hamada, Y., "Aircraft Gust Alleviation using Discrete-Time Preview Controller with Prior Gust Information," *The SICE Annual Conference 2013*, IEEE, 2013, pp. 1907–1912.

[23] Khalil, A. and Fezans, N., "Performance Enhancement of Gust Load Alleviation Systems for Flexible Aircraft using H_∞ Optimal Control with Preview," *AIAA Scitech 2019 Forum*, 2019, p. 0822.

[24] Khalil, A., and Fezans, N., "A Multi-Channel H_∞ Preview Control Approach to Load Alleviation Function Design," *CEAS Aeronautical Journal*, Vol. 12, No. 2, 2021, pp. 401–412.

[25] Khalil, A., and Fezans, N., "Gust Load Alleviation for Flexible Aircraft using Discrete-Time Preview Control," *The Aeronautical Journal*, Vol. 125, No. 1284, 2021, pp. 341–364.

[26] Takase, R., Fujita, K., Hamada, Y., Tsuchiya, T., Shimomura, T., and Suzuki, S., "Robust C* Control Law Design Augmented with LIDAR-Based Gust Information," *IFAC-PapersOnLine*, Vol. 52, No. 12, 2019, pp. 122–127.

[27] Hamada, Y., Saitoh, K., and Kobiki, N., "Gust Alleviation Control using Prior Gust Information: Wind Tunnel Test Results," *IFAC-PapersOnLine*, Vol. 52, No. 12, 2019, pp. 128–133.

[28] Rabadan, G. J., Schmitt, N. P., Pistner, T., and Rehm, W., "Airborne LIDAR for Automatic Feedforward Control of Turbulent In-Flight Phenomena," *Journal of Aircraft*, Vol. 47, No. 2, 2010.

[29] Hamada, Y., "Flight Test Results of Disturbance Attenuation using Preview Feedforward Compensation," *IFAC-PapersOnLine*, Vol. 50, No. 1, 2017, pp. 14188–14193.

[30] Ricci, S. and Scotti, A., "Wind Tunnel Testing of an Active Controlled Wing Under Gust Excitation," *Proceedings of the 49th AIAA/ASME/ASCE/AHS/ASC Structures, Structural Dynamics, and Materials Conference*, 2008, pp. 7–10.

[31] Lancelot, P., Sodja, J., Werter, N., and De Breuker, R., "Design and Testing of a Low Subsonic Wind Tunnel Gust Generator," *Advances in Aircraft and Spacecraft Science*, Vol. 4, No. 2, 2017, p. 125.

[32] Fonte, F., Riccobene, L., Ricci, S., Adden, S., and Martegani, M., "Design, Manufacturing and Validation of a Gust Generator for Wind Tunnel Test of a Large Scale Aeroelastic Model," *30th Congress of the International Council of the Aeronautical Science*, 2016, pp. 25–30.

[33] Takaba, K., "A Tutorial on Preview Control Systems," *IEEE SICE 2003 Annual Conference*, Vol. 2, 2003, pp. 1388–1393.

[34] Crassidis, J. L. and Junkins, J. L., *Optimal Estimation of Dynamic Systems*, 2nd ed., Chapman & Hall/CRC, Boca Raton, 2004.

[35] Doyle, J., "Guaranteed Margins for LQG Regulators," *IEEE Transactions on Automatic Control*, Vol. 23, No. 4, 1978, pp. 756–757.

[36] Safonovz, M. G., "Origins of Robust Control: Early History and Future Speculations," *Annual Reviews in Control*, Vol. 36, No. 2, 2012, pp. 173–181.

[37] Zames, G., "Feedback and Optimal Sensitivity: Model Reference Transformations, Multiplicative Seminorms, and Approximate Inverses," *IEEE Transactions on Automatic Control*, Vol. 26, No. 2, 1981, pp. 301–320.

[38] Doyle, J., Glover, K., Khargonekar, P., and Francis, B., "State-Space Solutions to Standard H_2 and H_∞ Control Problems," *IEEE Transactions on Automatic Control*, Vol. 34, No. 8, 1989, p. 831–847.

[39] Gahinet, P. and Apkarian, P., "A Linear Matrix Inequality Approach to H_∞ Control," *International Journal of Robust and Nonlinear Control*, Vol. 4, No. 4, 1994, pp. 421–448.

[40] Apkarian, P. and Noll, D., "Nonsmooth H_∞ Synthesis," *IEEE Transactions on Automatic Control*, Vol. 51, No. 1, 2006, pp. 382–382.

[41] Skogestad, S. and Postlethewaite, I., *Multivariable Feedback Control: Analysis and Design*, 2nd ed., Wiley, New York, 2007.

[42] Balas, G., Chiang, R., Packard, A., and Safonov, M., *Robust Control Toolbox User's Guide R2020a*, The MathWorks, Natick, 2020.

[43] McLean, D., *Automatic Flight Control Systems*, Prentice Hall, Englewood Cliffs, 1990.

[44] Schmidt, D., *Modern Flight Dynamics*, McGraw-Hill Higher Education, New York, 2011.

[45] Baldelli, D., Chen, P., and Panza, J., "Unified Aeroelastic and Flight Dynamic Formulation via Rational Function Approximations," *Journal of Aircraft*, Vol. 43, No. 3, 2006, pp. 763–772.

[46] Lind, R., and Brenner, M., *Robust Aeroservoelastic Stability Analysis*, Springer-Verlag, London, 1999.

[47] *Control System Toolbox User's Guide R2020a*, The MathWorks, Natick, 2020.

[48] Gangsaas, D., Ly, U., and Norman, D.,, "Practical Gust Load Alleviation and Flutter Suppression Control Laws Based on a LQG Methodology," *19th Aerospace Sciences Meeting*, 1981, p. 21.

[49] Karpel, M., Moulin, B., and Chen, P., "Dynamic Response of Aeroservoelastic Systems to Gust Excitation," *Journal of Aircraft*, Vol. 42, No. 5, 2005, pp. 1264–1272.

[50] Etkin, B., Hughes, P., and Zhu, S., "Equivalent Deterministic Inputs for Random Processes," *Journal of Guidance, Control, and Dynamics*, Vol. 7, No. 4, 1984, pp. 477–482.